Stellingen

behorende bij het proefschrift

Novel Scanning Probes Applied to the Study of Nanostructures

van Luca Canali

1. The Scanning Gates probes described in this thesis can form the starting point of a new design of ultra-sensitive electrometers with exceptional spatial resolution. These can be realised by connecting the two electrodes of the Scanning Gates with a single colloid in between two tunnel barriers. (From the preface to this thesis).

2. The development of giant magnetoresistance (GMR) read-heads for the latest generation of hard drives represents one of the most successful examples of research in applied physics, because in a few years scientists and engineers at IBM went directly from the discovery of the fundamental physical phenomenon of GMR to the realisation of an innovative commercial product.

3. Hexanedithiols do not form an ordered self-assembled monolayer on gold substrates (from chapter 7 of this thesis)

4. In the XIX century chemistry had a leading role amongst the different branches of science, the XX century was the century of physics. The XXI century will be the century of biology.

5. In the age of internet and quickly-available electronic publishing, the traditional method for publishing scientific documents, including Ph.D. theses, yields a product that is old the same day that it comes out of the press. An electronic document, on the other hand, can 'live' much longer by means of frequent and low-cost updates to its contents.

6. *In rebus quibuscumque difficilioribus non expectandum, ut qui simul, et serat, et metat, sed praeparatione opus est, ut per gradus maturescant*. BACON, *Serm. Fidel.* n. XLV. [In all the most difficult subjects, one should not expect that someone could sow and harvest at the same time, but a delay is necessary to let the new ideas mature slowly.] This thought applies very well to many research projects in science.

7. In the elegance of the style and simplicity of execution lie the foundations for excellent art and exquisite food preparation.

8. Most critics consider comic writing as 'minor' and not meritorious of mention in the books of history or literature. This attitude is utterly diminutive of the merits of true literary geniuses like P.G. Wodehouse.

9. A considerable amount of all the money freely circulating in the world markets is kept out of trade and accumulated in private households in form of piles of small coins because they are too inconvenient to carry in the wallet.

1.De Scanning Gates sondes zoals beschreven in dit proefschrift kunnen het begin vormen van een nieuw ontwerp van ultra gevoelige electrometers met een uitzonderlijke ruimtelijke resolutie. Dit kan worden gerealiseerd door twee electrodes van de Scanning Gates te verbinden met een colloid tussen twee tunnel barriers. (Zie de inleiding van dit proefschrift).

2. De ontwikkelen van giant magnetoresistance (GMR) read-heads voor de nieuwste generatie hard drives is een van de meest succesvolle voorbeelden van onderzoek in toegepaste natuurkunde, omdat in een paar jaar tijd wetenschappers en technici bij IBM meteen vanaf het moment van ontdekking van het principe van het natuurkundige phenomeen GMR, naar de realisatie van een vernieuwend commercieel product overgingen.

3.Hexanedithiols vormen niet een geordend self-assembled monolayer op gouden substraten (zie hoofdstuk 7 van dit proefschrift)

4. In de negentiende eeuw had scheikunde een vooraanstaande rol in de verschillende takken van wetenschap, de twintigste eeuw was de eeuw van de natuurkunde. De eenentwintigste eeuw zal de eeuw van de biologie worden.

5.In het tijdperk van internet en snel beschikbare publicatie door middel van electronica, levert de traditionele methode om wetenschappelijke documenten te publiceren, zoals proefschriften, een product af dat al oud is op de dag dat uit de pers komt rollen. Een electonisch document, aan de andere kant, is veel langer houdbaar doordat men het frequent en voor weinig geld kan updaten.

6. *In rebus quibuscumque difficilioribus non expectandum, ut qui simul, et serat, et metat, sed praeparatione opus est, ut per gradus maturescant.*
BACON, Serm. Fidel. n. XLV
Als het de meest lastige onderwerpen betreft, kan men niet verwachten dat men kan zaaien en oogten tegerlijk, maar er is een vertraging nodig om nieuwe ideeen langzaam te laten rijpen.
Deze gedacht is erg goed toepasbaar op vele projecten van wetenschappelijk onderzoek.

7.In de sierlijke manier van vormgeven en de eenvoudige uitvoering liggen de grondslagen voor geweldige kunst en de voortreffelijke bereiding van gerechten.

8. De meeste critici beschouwen comische literatuur als minderwaardig en vinden dat zulke geschriften het niet verdienen in boeken en de literatuurgeschiedenis te worden vermeld. Deze houding is volkomen neerbuigend jegens de verdiensten van ware literatuurgenieen zoals P.G. Wodehouse.

9.Een aanzienlijke hoeveelheid van al het geld dat vrij circuleert in de wereldmarkt wordt uitgesloten van de handel doordat het is opgestapeld in huishoudens in de vorm van stapels kleingeld omdat ze te onhandig zijn om in een portemonnne te mee te slepen.
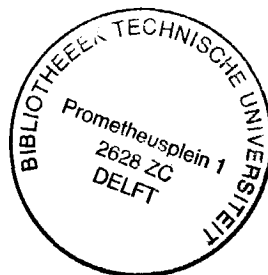
Novel Scanning Probes Applied to the Study of

Nanostructures

Novel Scanning Probes Applied to the Study of Nanostructures

Proefschrift

ter verkrijging van de graad van doctor
aan de Technische Universiteit Delft,
op gezag van de Rector Magnificus Prof.ir. K.F. Wakker,
voorzitter van het College voor Promoties,
in het openbaar te verdedigen op dinsdag 14 november 2000 om 16:00 uur

door **Luca CANALI**
dottore in fisica

Geboren te Parma (Italië)

Dit proefschrift is goedgekeurd door de promotoren:

        Prof.dr.ir L.P. Kouwenhoven
        Prof.dr.ir J.E. Mooij

Samenstelling van de promotiecommissie:

Rector Magnificus	T.U. Delft, voorzitter
Prof.dr.ir J.E. Mooij	T.U. Delft, promotor
Prof.dr.ir L.P. Kouwenhoven	T.U. Delft, promotor
Prof.dr.ir T.M.Klapwijk	T.U. Delft
Prof.dr.ir H.W.M. Salemink	T.U. Delft
Prof.dr.J.M. van Ruitenbeek	U. Leiden
Prof.dr.H. van Kempen	K.U. Nijmegen
Dr. P.M. Koenraad	U.D-T.U. Eindhoven

Questa tesi è dedicata alla memoria

di mio padre Franco Canali.

Preface

This thesis concludes my graduate research at the Technical University of Delft in the group Quantum Transport in the period between March 1996 and June 2000. It contains several experiments on low-temperature scanning probes applied to the study of mesoscopic and nanoscopic physics. The experiments discussed in this thesis concern the investigation of the electronic structure and/or transport properties of man-made systems that show prominent quantum mechanical effects.

The most innovative part of this work is constituted by the development of a novel scanning probe that we called the Scanning Gate (S-gate, patent number NL1013671). An extensive discussion of the fabrication and use of the S-gate probes is presented in chapters 4 to 7. The experiments presented in this thesis show that the S-gate has a great potential for future applications as a tool to improve STM spectroscopy with three-terminal measurements. The technique developed to fabricate the S-gate is also very interesting in itself and will probably lead to the development of new probes: for example it may be possible to extend the fabrication process of the S-gates by connecting the two electrodes with a colloid, in between two tunnel barriers. The resulting device would be a scanning SET with exceptional spatial resolution for the study of the quantum Hall effect or hydrodynamics effects in electronic transport (see also chapter 3).

A Ph.D. thesis, by definition, can only contain those parts of the research that have produced 'results'. This means that the Reader will find here only the results of those few happy days, when the gods of STM have blessed us with the kiss of good luck. Those who are interested in knowing the details of the day-to-day work of an experimentalist (in this area of research) will alas, have to search elsewhere.

In the following I would like to distribute my thanks amongst the people I have had the pleasure to work with in the last four years. First of all I would like to thank my supervisors Leo Kouwenhoven and Hans Mooij. I have very much appreciated in Leo the ability to push me towards obtaining good results in the various projects that make this thesis, and, at the same time, to keep a laid-back approach towards people management and life in general. I share with many QT-ers the belief that Hans Mooij has done a great job over the years to build and maintain an excellent research group. Many of the experiments discussed in this thesis have been performed together with

Table of Contents

Chapter 1

Introduction to Scanning Tunnelling Microscopy

Abstract:

In this chapter we introduce the reader to the basic ideas behind the operation and interpretation of STM experiments. Starting from the original ideas of Binnig and Röhrer we discuss the structure and design of an STM set-up and then we review the formulae commonly employed to interpret STM topographies and spectroscopies. We also describe our custom STM set-ups and their optimisation for low-temperature operations.

The basics of STM

The scanning tunnelling microscope (STM) appeared in 1981 when Gerd Binnig and Heinrich Röhrer [1] of the IBM Zürich set out to build a tool for studying the local conductivity of surfaces. Its principle of operation is based on the quantum mechanical phenomenon known as tunnelling, in which the wavelike properties of electrons permit them to 'tunnel' beyond the surface of a solid into regions of space that are forbidden to them under the rules of classical physics. The probability of finding such tunnelling electrons decreases exponentially as the distance from the surface increases. The STM makes use of this extreme sensitivity to distance. The sharp tip of a metallic needle (typically tungsten or platinum) is positioned a few angstroms from the sample surface. A voltage bias is applied between the probe tip and the surface, causing electrons to tunnel across the gap. As the probe is scanned over the surface, it registers variations in the tunnelling current, and this information can be processed to provide a topographical image of the surface. Binnig and Röhrer chose the surface of gold for their first image. When the image was displayed on the screen of a television monitor, they saw rows of precisely spaced atoms and observed broad terraces separated by steps one atom in height. Binnig and Röhrer had discovered in the STM a simple method for creating a direct image of the atomic
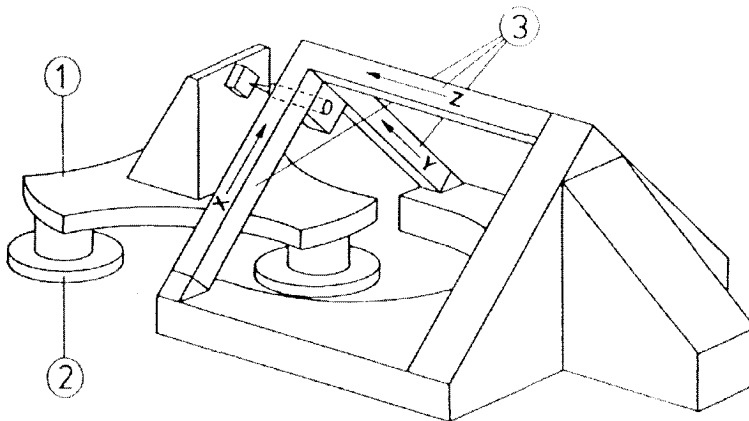
Figure 1: Scheme of the first working STM developed by Binning, Rohrer, Gerber and Weibel at IBM Zürich in 1981. (1) Coarse approach: the 'louse' with piezoelectric base plate and three feet (2) allowing the sample to be approached towards the tip. (3) The tip is mounted on a piezoelectric tripod scanner.

structure of surfaces. Their discovery opened a new era for surface science, and their impressive achievement was recognized with the award of the Nobel Prize for Physics in 1986. The advance of this new form for surface microscopy had been previously impeded by four instrumental problems: (1) the isolation of the experiment from the natural vibrations that are present in every laboratory, (2) the approach of the probe tip to the sample surface, (3) the scanning of the probe across the sample surface, and (4) the sharpening of the tip. The techniques that Binnig and Röhrer employed to solve these problems are elegant and straightforward and are briefly described here. The sample and the scanning probe are protected from vibrations by being placed on a stage that is suspended from springs within another section or stage. This outer stage is in turn suspended from springs within a stainless steel frame. The structure is equipped with magnets and copper plates that will, if necessary, induce eddy currents that damp any motion of the stages. The placement and scanning movement of the probe are controlled by a tripod made of piezoelectric materials (which expand or contract when voltage is applied) and by a piezoelectric plate with three metal feet that can be fastened to a metal plate carrying the sample. Applying a voltage to one leg of the tripod (or to the piezoelectric plate) causes the other tripod legs (or one or more of the metal feet) to move slightly. Both the direction and the magnitude of this movement can be precisely controlled. The tip is sharpened by applying a strong electric field; this dislodges the surface atoms of the tip until only a few (ideally, one) remain. The sharp tip in the STM is similar to that in the scanning electron microscope (SEM), but the differences in the two instruments are profound. In the SEM, electrons are extracted from the tip with a series of positively charged plates placed a few centimetres downstream from the tip. The electrons at the apex of the tip are confined to the region within the metal by a potential barrier. The attractive force from the positive charge on the plates is sufficient to permit the electrons to overcome the barrier and enter the vacuum as free particles. The apertures in the downstream plates form an electron lens that converts the diverging beam from the tip into a beam converging to a focus on the surface of the sample. In the STM, the set-up is much simpler. The plates that form the lens in the SEM are removed, and the tip is positioned close to the sample. The electrons move through the barrier because of the quantum mechanical effect of tunnelling: when the tip is moved close to the sample, the spacing between the tip and the surface is reduced to a value comparable to the

spacing between neighbouring atoms in the lattice. In this circumstance, the tunnelling electron can move either to the adjacent atoms in the lattice or to the atom on the tip of the probe. The tunnelling current measures the local density of states (LDOS) of the electrons at the surface of the sample. A sufficiently stable STM can measure the small LDOS modulation generated by single surface atoms or impurities. Images of the atomic lattice at the surface have been measured for many semiconductors (for example Si, GaAs, InAs, etc [2]) and metals (gold, platinum, silver, nickel, copper, etc [3]).

Quantitative interpretation of STM experiments

The calculation of the tunnel current (I_t) in an STM experiment is a complicated quantum mechanical problem involving the solution of Schrödinger equation in three dimensions. Even such an accurate approach, tough, would have to rely on some degrees of modelling, mainly concerning the shape of the STM tip which, in most cases, is composed of an irregular and uncontrollable arrangement of atoms at its apex. It is nevertheless possible to simplify the problem with a series of 'reasonable' approximations and reach a simple formula for the tunnel current. The first approximation is to treat the problem in first-order time-dependent perturbation theory neglecting inelastic tunnelling events:

$$I(V) = \frac{2\pi e}{\hbar} \sum_{\mu,\nu} \left\{ f(E_\mu)[1 - f(E_\nu - eV)] - f(E_\nu)[1 - f(E_\mu - eV)] \right\} \cdot |M_{\mu\nu}|^2 \delta(E_\nu - E_\mu)$$

Where $f(E)$ in the Fermi distribution, V is the applied voltage and $M_{\mu\nu}$ is the tunnelling matrix element between quantum states ψ_μ and ψ_ν, respectively, of the tip and of the sample. An analytical expression for $M_{\mu\nu}$ was derived by Bardeen [4]

$$M_{\mu\nu} = -\frac{\hbar^2}{2m} \int dS \cdot \left(\psi_\mu^* \nabla \psi_\nu - \psi_\nu^* \nabla \psi_\mu \right).$$

A simpler formula for the tunnel current requires the introduction of a few extra approximations, which apply to most of samples and tips used for STM experiments:

(a) $M_{\mu\nu}$ is only a function of the energy U and tip-sample distance z, (b) $T = 0$ so that the Fermi distribution has a simple step-like shape, (c) we assume that the tip is very sharp so that the tunnelling events are localised in space, (d) we ignore the effect of spin (not applicable for STM on magnetic materials). Given those approximations, the current can be written as a simple convolution of the (local) density of states of the tip and of the sample multiplied by a factor $M(U,z)$.

$$I(\mathrm{V},z) = \frac{4\pi e}{\hbar} \int_0^{eV} \mathrm{d}U\, \rho_\mathrm{T}(E_{F,1} - eV + U)\rho_\mathrm{S}(E_{F,2} + U)M(U,z),$$

where $E_{F,1}$ and $E_{F,2}$ are the Fermi energies of the tip and sample. The local density of states (LDOS) can be written as

$$\rho(\mathrm{r},E) = \sum_k |\psi_k(\mathrm{r})|^2 \cdot \delta(E_k - E),$$

this is a generalisation of the usual expression for the density of states that takes into account the spatial modulation of the wavefunction. In the case of small voltage bias, the matrix element can be written (using the WKB approximation) as $M(k,z) = M_0 \exp(-2kz)$. A simple expression for k can be derived in the case of a rectangular barrier of height ΔW: $k^2 = 4\pi m(\Delta W + U) / h^2$. Furthermore, the density of states of the tip can be approximated as a constant for metal tips. With these additional approximations we obtain the following simplified expression for the tunnel current:

$$I_T(\mathrm{V},z) \propto e^{-kz} \int_0^{eV} \mathrm{d}U\rho_\mathrm{S}(E_F + U).$$

The physical interpretation of this formula is that (a) the STM current I_T 'measures' the local density of states of the sample and (b) that I_T varies exponentially with the tip-sample distance. An intuitive picture of the STM tunnelling processes is to consider the current as being entirely emitted from the last atom of the tip and going directly into the sample beneath it at a distance z determined directly by the magnitude of the tunnel current.

The STM can be used to image the surface of conducting samples with the highest resolution of any other microscope. The most common mode of operation for an STM

is called the 'constant current' topographic mode; that is when the tip hovers over the sample while an electronic feedback loop maintains the tunnel current constant (see Fig. 2). The map of the tip position $z(x,y)$ is a topographic representation of the sample, i.e. by means of the feedback loop the tip follows the profile of the sample maintaining a constant distance to it (see Fig. 2). The displacement of the tip in the three spatial dimensions is taken care of by computer-controlled electronics: the tip is normally mounted on a piezoelectric tube which can be driven with high accuracy (better than a picometer in some set-ups) by a set of DACs and high voltage amplifiers.

A few more details have often to be taken into account to interpret the STM topographies, the most common ones are: tip convolution, double tip, and drift. The first two effects stem from the fact that a real tip is most likely not point-like in shape, as assumed in our simplified equations for the tunnel current. The image will thus be the result of a convolution of the tip-shape and the actual image of the sample. This phenomenon can be best understood with a *Gedankenexperiment* of 'reversed STM', where the sample presents a very sharp (atomic) feature, while the tip is very blunt (e.g. has a diameter of a few tens of nanometers). In this case the role of the sample and the tip in the STM experiment are reversed and scanning one over the other produces an image of the tip taken by the protrusion on the sample. Any other topography taken with that particular tip will be convoluted with such an image which
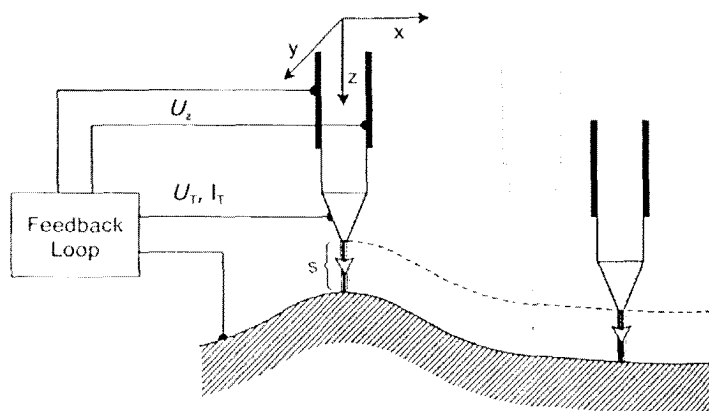
Figure 2: Pictorial illustration of the functioning of the STM in the so-called constant current mode: a feedback loop maintains constant the tunnel current flowing between the tip and the surface, while the STM is scanned over the sample. Typically a computer records the map of the voltages applied to the piezos $U_z(U_x,U_y)$ and displays it in graphical form as a topographic map of the sample.

can therefore be considered as the 'signature' of the tip. Note that, knowing the STM imaging of the tip, it is possible to calculate back the real topography of the sample.

A 'double tip' is a particular case of tip convolution, where the tip has two sharp protuberances at the apex and thus all the sample features appear with a shadow-like replica. Drift is another common cause of distortion of STM images: it appears as a continuous shift of the images towards one particular direction of the scan field. There are two main types of drift: thermal and electronic. The former is seen when the STM is not uniformly thermalised and, consequently, thermal expansion/contraction can cause the relative position of the tip and sample to change in time. This is normally seen in the topography as a constant drift of the image toward a fixed direction in space. Electronic drift has the same effect of thermal drift and can be caused by a variable offset in the high-voltage amplifiers that drive the piezotube. This effect is normally not observed in our STM control electronics. Another effect that gives distortions similar to electronic drift is 'piezoelectric creep': after a fast voltage change the piezotube will have a slow creep in time according to the formula [5] $\Delta l/l = a + b \cdot \ln(t)$, where a and b are constants and t is the time.

Low-temperature STM

The STM has already become a standard tool in experimental solid-state physics and material science. In particular, we are interested on its applications to the area of mesoscopic physics, i.e. the investigation of the electronic properties of 'systems' with sizes between molecular ($\sim 10^{-9}$ m) and macroscopic objects ($> 10^{-6}$ m). For the study of mesoscopic phenomena, the STM is often used as a controllable electrical contact to be positioned (with subnanometer resolution) on the device under study to acquire spatially resolved spectroscopy. Another class of mesoscopic experiments involves some sort of extension of the basic STM capabilities, which allows, for example, the investigation of surface electric and/or magnetic fields (see also chapter 3). Most of the interesting phenomena in mesoscopic physics have typical energy scales of a few meV and are thus observable only at low temperatures, e.g. the thermal broadening at liquid helium temperature (4.2 K) is of the order of 1 meV. For this reason, we have developed and used STM set-ups capable of working from room temperature down to ~100 mK. A low-temperature STM is not fundamentally
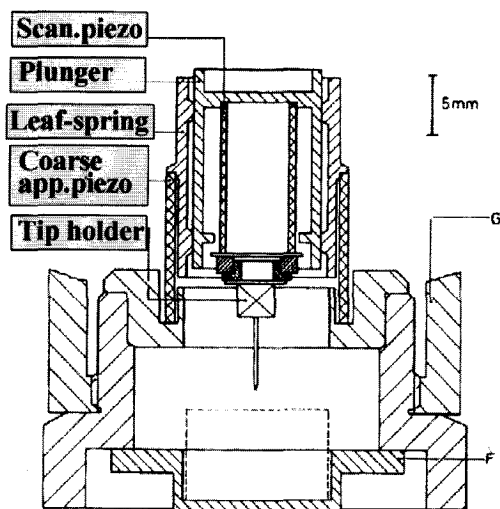
Figure 3: Drawing of one of our low-temperature STMs, from Ref. 6. The scan piezo (housed inside the plunger) allows the control electronics to move the Pt-Ir tip in three dimensions. A coarse-approach piezotube is used to make plunger slide in the vertical direction inside its stainless steal holder. (F) Sample holder. (G) External body of the STM.

different from any other STM, apart from a few extra technical problems in its design and operation: (a) developing movable parts (mainly the STM plunger) that are able to work at room- and low-temperature, (b) installing the STM in a cryostat, (c) providing a good vibration insulation system.

Figure 3 shows the scheme of one of our homemade STM scan-heads, developed following the design of Wildöer et al. [6,7] with some custom modifications. The STM tip is mounted on the tip-holder, which can be screwed on a copper nut glued onto the scan-piezotube. The piezotube is externally divided into four quadrant-electrodes, which provide the lateral displacement; the inner part of the tube is the fifth electrode and provides the vertical movement. The five electrodes are connected to high-voltage low-noise amplifiers to drive the motion of the tip in three dimensions. The piezotube is glued inside a stainless steel plunger coated with a thin layer of hard ceramic [8]. The ceramic coating prevents the (mechanical) wearing of the plunger. Stainless steel is used because of its low thermal expansion coefficient (a large contraction of the plunger at low temperatures could break the ceramic piezotube). Besides, special non-magnetic steel is used, so that the STM can be used

in combination with high magnetic fields, without experiencing considerable contraction/expansion. Molybdenum sulphide (diluted in 2-propanol) is used as a lubricant to ensure that the plunger will be able to slide inside the holder even at low-temperatures. For the same reason it is crucial that all contaminants that can freeze at low temperatures (such as fingerprints) are carefully removed from the sliding surfaces (plunger and leaf springs). The holder makes contact to the plunger by means of two leaf springs which are also made of stainless steel, again to avoid problems with thermal contraction/expansion of the STM. The leaf springs are adjusted so that the static friction of the plunger on the inner tube is ~1 N at room temperature: a higher friction coefficient would require too high excitation voltages for the slip-stick motion, while a softer spring constant would degrade the stiffness and stability of the STM.

A second piezotube is glued to the external part of the holder to be used for the slip-stick coarse-approach motion: the holder is slowly stretched by applying a (high-voltage) waveform to the piezotube (roughly with a parabolic shape), then the piezo is quickly contracted back to its original length: this forces the plunger to slide down by effect of its inertial force. This is true only if the inertial force is bigger than the static friction between the plunger and the holder. The STM is designed to fit into commercially available cryostats and inserts such as Oxford instruments' Heliox^{TM} and Kelvinox^{TM} (see also Fig. 6). To provide better thermal contact at low temperatures, the external body of the STM and the sample holder are made of
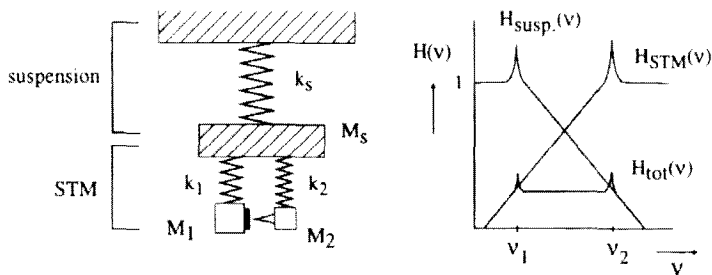
Figure 4: (a) Schematic representation of the model describing the STM response to external vibrations. The spring constants k_s, k_1, k_2 and the masses M_s, M_1, M_2, define the mechanical problem. (b) The total response function of the system is the product of the response of the STM and the suspension system, as shown in figure. The best noise attenuation is obtained when the resonance frequency of the suspension, v_1, and STM, v_2, are, respectively, very small and very large (Ref. 6).

copper.

Mechanical stability is a crucial issue for STM. We have discussed in the previous paragraph that the tunnel current is roughly exponentially dependent on the tip-sample distance. Typically the tunnel current changes an order of magnitude for every change of the tip-sample distance of 0.1 nm.

This means, for instance, that to achieve a stable tunnel barrier with 1% noise in the current, the STM must have a mechanical stability of 1 pm or better. On the other hand, building vibrations have amplitudes of the order of 10 to 100 nm, which is several orders of magnitude more than the required stability. For this reason it essential to equip STM set-ups with vibration damping systems. Particular care on that subject has to be taken in developing low-temperature STMs, which suffer the contact with 'extra' noise sources like the boil of cryogenic fluids and/or vibrations from the pumps. Figure 4a shows a simplified model system to study the effect of vibrations coupling into the STM and how to damp them. Only the masses and the spring constants of the parts of the STM have to be taken into account to calculate the vibrational response function $H(v)$. $H(v)$ is the ratio of the amplitude of the oscillation of the forced oscillator (the STM) over the excitation amplitude with frequency v (Fourier component of the vibration noise). The total response function of the STM is the product of the response function of the vibration damping system and the one of the STM (tip-sample distance oscillations). Figure 4b shows the two response
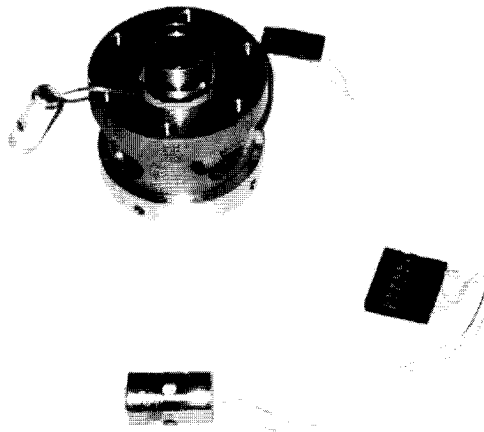
Figure 5: Photograph of the low-temperature STM set-up used for the experiments of chapter 9 (STM on passivated InAs). The piezotube is housed in a stainless steel plunger and connected to the high-voltage signal via the black connector. The body of the STM that provides the coarse approach motion is visible on the top of the picture.
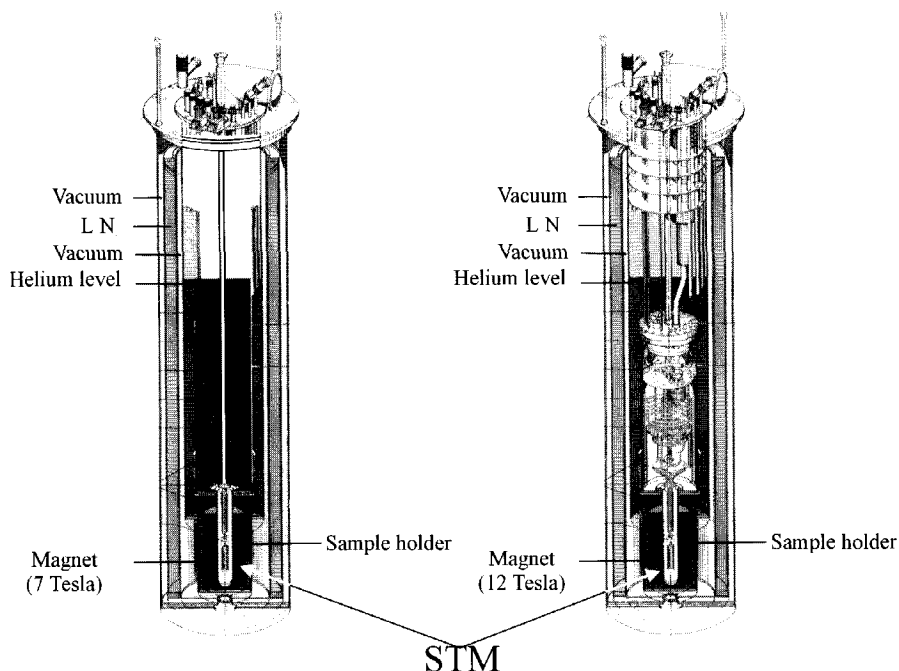
Figure 6: Our STM design can fit various cryostats with minor modification. Left: our STM scan head is mounted on a home-made insert that can be cooled down to 4.2 K in a cryostat equipped with a 7 T magnet (see also Fig. 5). Right: the same design for the STM scan head has been customised to fit into a commercial dilution refrigerator to reach temperatures below 100 mK.

functions and their product: the damping system behaves like a low-pass filter, while the STM behaves like a high-pass one. The overall result is the reduction of the external oscillations by several orders of magnitude. The most effective reduction is obtained for low v_1 and high v_2, which means that the damping system should be very 'soft' and the STM construction very stiff. A simple but effective damping system has been realized in our set-up by suspending the STM (together with the entire cryostat) with elastic ropes. The resonance frequency of such damping system depends on the length and quality of the elastic ropes, and is of the order of a few Hertz for our set-up. We have taken care to have a high resonance frequency v_2, by making our STMs small and compact. Moreover most of the critical parts of the STMs are made of stainless steel to improve their stiffness. In our set-up, v_2 is of the order of a few

kHz [6]. Figure 5 shows a photograph of the low-temperature set-up used for the experiments reported in chapter 9. There the STM is mounted on a homemade low-temperature insert capable of reaching liquid helium temperatures in just a few hours. The insert is used in combination with an Oxford instruments cryostat equipped with a superconducting magnet (see also Fig. 6 for a drawing of the set-up).

For the control electronics, there is no particular difference between room temperature and/or 4K operations. For this reason we have decided to use commercial electronics and software to drive our STM set-ups. Namely we have used control units by Omicron, RHK and Oxford instruments.

References

[1] G. Binnig, H. Röhrer, C. Gerber, E. Weibel, Phys. Rev. Lett. **49**, 57 (1982).

[2] see for example J. A. Stroscio *Scanning Tunneling Microscopy,* Boston Academic Press (1993).

[3] see for example C. J. Chen *Introduction to Scanning Tunneling Microscopy,* Oxford University Press (1993).

[4] J. Bardeen, Phys. Rev. Lett. **6**, 57 (1961).

[5] R. Wiesendanger *Scanning probe microscopy and spectroscopy,* p. 96, Cambridge University Press (1994).

[6] J.W.G. Wildöer, *Low temperature STM on mesoscopic systems,* PhD thesis, Nijmegen (1996).

[7] J.W.G. Wildöer, A.J.A. van Roy, H. van Kempen and C.J.P.M. Harmans Rev. Sci. Instrum. **65**, 2849 (1994).

[8] The plunger is coated with ~100 μm of titanium carbonitride, by Gimex technische keramiek b.v., The Netherlands.

Chapter 2

Introduction to the Physics of Metallic Clusters

Abstract:

Metallic clusters have attracted considerable interest in recent years because of their peculiar physical and chemical properties and also because of their industrial applications. From the physical point of view, clusters form the link between the well-established fields of solid-state and atomic physics. From the chemical point of view, clusters are interesting for important applications, such as catalytic converters and solar cells. In this chapter we review some of the most significant properties of clusters and colloids, mainly focusing on electronic transport measurements.

Metallic clusters

How many atoms of gold does it take to make a crystal showing metallic properties? Questions like that make the physics of small metallic particles an interesting topic for fundamental research. The most evident difference between clusters and solids is the ratio surface/volume. In the case of macroscopic systems, that ratio is negligible: we talk then of bulk properties of the solid. In the case of small clusters, the properties of the surface can completely alter their physical properties. More precisely, the electronic spectrum (and density of states) of a cluster is intrinsically different to that of a solid. Indeed, an important approximation in solid-state physics [1] is to assume the quantum number **k** (a vector in $\Re^3$ that is proportional to the pseudo-momentum of the electron $\hbar \mathbf{k}$) as a continuous variable. Moreover, the dispersion relation E(**k**), which contains most of the information about the physics of the solid, is also a function with values in $\Re$. Conversely, for small particles, the electronic spectrum is indexed by a integer quantum number n and the dispersion relation E(n) is composed of a sequence of electronic levels, similarly to the spectrum of atoms and molecules.

Throughout this chapter we will refer to small metallic particles as (metallic) clusters and colloids. Although the two terms have similar meanings and are often used as synonyms in literature, here we would like to make a distinction which can also help to understand better the structure of these objects. Strictly speaking, colloids are particles substantially bigger than atoms or simple molecules but much too small to be
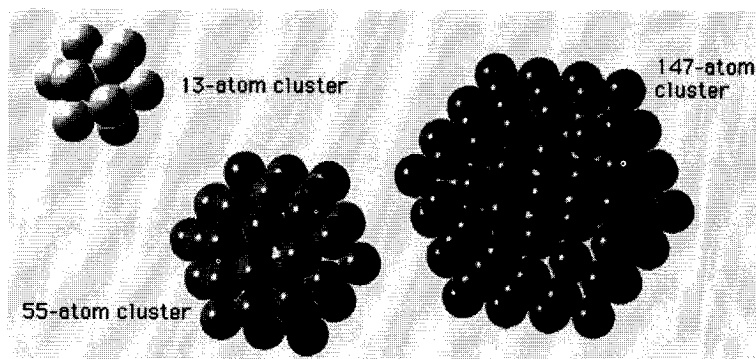
Figure 1: Clusters of noble metals form particularly stable structures when they have exactly the number of atoms needed to arrange into a regular structure. The first 3 regular structures can be shown to have respectively 13, 55 and 147 atoms.

visible to the unaided eye. Such particles range in size from about 10^{-9} to 10^{-5} m and can be linked or bonded together in various ways.

Colloidal systems may exist as dispersions of one substance in another as, for example, smoke particles in air, or as single substances, such as rubber. The term cluster indicates a subclass of colloids that have a regular (crystalline) structure. Clusters can be formed, for example, by atoms of noble metals bound by short-range forces that depend only on the distance between each pair of atoms. This class of clusters shows very high stability when it can form highly symmetric structures, called Mackay icosahedra [2]. The first three clusters of this kind (also called magic-number clusters) can be seen in Fig. 1 for an increasing number of atoms from left to right: 13, 55, and 147. In the 13-atom cluster, all but one of the atoms occupy equivalent surface sites. The 55-atom cluster in this series consists of a core, which is just the 13-atom icosahedron, plus 12 more atoms on top of the 12 vertices of the icosahedron and 30 more atoms, one in the centre of each of the 30 edges of the icosahedron. The 147-atom cluster consists of a 55-atom icosahedral core, 12 more atoms at the vertices of the outermost shell, one atom in the centre of each of the 20 faces, and two atoms along each of the 30 edges between the vertices. The shell structure that provides special stability to this class of clusters is determined by the regularity and symmetry of their geometric structure. A different kind of extraordinary stability manifests itself in clusters of simple metal atoms. The shell structure for this class of clusters is determined by the electrons and the filling of those shells that have energy states available to the electrons [3]. The numbers of electrons corresponding to closed electron shells in metal clusters are 8, 20, 40, 58, ... The electronic structure can be modelled by supposing that the positively charged cores consisting of the protons and inner-shell electrons of all the cluster's atoms are smeared out into a continuous, attractive background, while the valence, or outer-shell, electrons are delocalised (i.e. shared among all atoms in the cluster). The electrostatic potential is much like a well or pit with a flat bottom and a moderately steep wall. The determination of the energy states available for electrons in such a simplified model system is relatively easy and gives a good description of clusters of more than about eight or nine alkali atoms, i.e. lithium, sodium, potassium, rubidium, or caesium. The single valence, or outer-shell, electron of each alkali atom is treated explicitly, while all the others are considered part of the smeared-out core. Since each

alkali atom has only one valence electron, the unusually stable clusters of alkalis consist of 8, 20, 40, . . . atoms, corresponding to major shell closings. This model is not as successful in treating metals such as aluminium, which have more than one valence electron.

Electrical properties of metallic clusters

The electrical characteristic of small metallic particles present interesting deviations from Ohm's law. When the size of the particle is small enough a new phenomenon characterises its spectroscopy: Coulomb blockade (CB). A basic explanation of CB can be illustrated by considering that the energy necessary to put a charge q on a conductor of capacitance C, is $q^2/2C$. The capacitance scales as the size of the conductor (this follows directly from the linearity of Poisson equation) and, thus, the charging energy diverges as $1/r$ when the size of the conductor goes to zero. Moreover, the total charge of an isolated metallic cluster has to be an integer multiple of the electron charge e, so that there is a minimum energy that the electrons must have in order to be able to jump onto the cluster from the contact leads. This is the single electron charging energy $E_c = e^2/2C$. For example, the energy to put one electron into a cluster with diameter ~1 nm is of the order of 1 eV. When $E_c > k_B T$ this effect can manifest itself in the I-V characteristic as a blockade of the current.

In the following we want to give a more quantative explanation of the CB, following the so-called orthodox theory of single electron tunnelling following the notation of Averin et al. [4] and Hanna et al. [5]. We consider the circuit of Fig. 2, as a model of the simplest single-charge tunnelling system: R_1 and C_1 are the resistance and capacitance of the left junction, R_2 and C_2 of the right junction, $C_\Sigma = C_1 + C_2$, is the
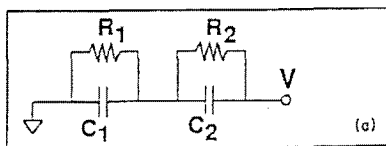
Figure 2: The physical problem of single-electron charging can be described with a simple model circuit of two tunnel junctions with capacitances C_i and resistances R_i. $C_\Sigma = C_1 + C_2$, is the total capacitance (the capacitance between the cluster and the surrounding conductors).

total capacitance (the capacitance of the cluster). The charge Q on the cluster can be written as $Q = ne - Q_0$, where n is the integer closest to Q/e. Q_0 is called the residual charge.

The electron tunnelling rate from the jth junction to the cluster, with the process $n \rightarrow n \pm 1$ is represented by $\Gamma_j^{+/-}(n)$. Such quantity can be obtained from a basic golden-rule calculation:

$$\Gamma_j^{\pm}(n) = \frac{1}{R_j e^2} \left(\frac{-\Delta E_j^{\pm}}{1 - \exp(\Delta E_j^{\pm}/K_B T)} \right).$$

Where ΔE is the energy change of the system when the electron tunnels across the barrier. From electrostatic energy considerations:

$$\Delta E_1^{\pm} = \frac{e}{C_{\Sigma}} \left(\frac{e}{2} \pm (ne - Q_0) \pm C_2 V \right),$$

$$\Delta E_2^{\pm} = \frac{e}{C_{\Sigma}} \left(\frac{e}{2} \pm (ne - Q_0) \mp C_1 V \right).$$

The current is given by

$$I(V) = e \sum_{n=-\infty}^{\infty} \sigma(n) \left[\Gamma_2^+(n) - \Gamma_2^-(n) \right] = e \sum_{n=-\infty}^{\infty} \sigma(n) \left[\Gamma_1^-(n) - \Gamma_1^+(n) \right],$$

where $\sigma(n)$ is the normalised ensemble distribution of the number of electrons on the cluster. The distribution is obtained by noting that the net probability for making a transition between two adjacent states in the steady state is zero, thus:

$$\sigma(n)[\Gamma_1^+(n) + \Gamma_2^+(n)] = \sigma(n+1)[\Gamma_1^-(n+1) + \Gamma_2^-(n+1)].$$

The last two equation can be solved self-consistently by numerical methods to calculate the $I(V)$ characteristic. We have used such a program (available from Ref. 6) to model our experimental data obtained with a gated STM on a gold cluster (see also chapter 4). Good agreement was found between the model and the measured data, which allowed us to fit the capacitances and resistances of the junctions from the measurements.

Non-equilibrium effects in the tunnelling density of states

The orthodox theory described in the previous paragraph takes into account only the charging properties of the clusters. A much richer class of physical phenomena can be investigated studying very small clusters at low temperatures, i.e. such that the mean level spacing of the particle $\Delta < 3.5 \cdot k_B T$ (the thermal broadening). When that condition is satisfied, the dI/dV characteristic will show resonances associated with the presence of quantised levels. More precisely, a peak in the dI/dV will be measured [7] each time a transport channel opens up because a new electronic level enters the energetically allowed bias window.

More recent experiments on ultrasmall metallic particles [8] have shown that there are complicated many-body phenomena in the clusters, which may generate extra features in the tunnelling spectroscopy. Agam et al. [9] have investigated that problem by studying non-equilibrium tunnelling spectroscopy, focusing their attention on the (experimental) voltage regime with at most one extra electron in the dot. At small voltage bias V, within the Coulomb-blockade regime (see Fig. 3a), current does not
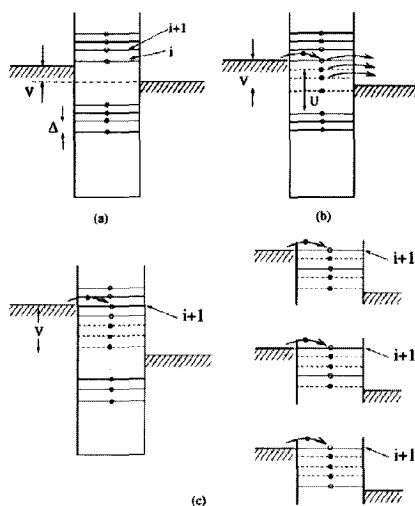
Figure 3: An illustration of transport through the metal particle at various values of the source-drain voltage V. Filled single-particle levels are indicated by full circles and empty ones by open circles. U is the charging energy, and Δ is the single-particle mean level spacing. (a) The system at small bias voltage within the Coulomb blockade regime. (b) V corresponding to the first cluster of resonances. The thin dashed lines indicate the energy of a level after an electron has tunneled into the dot. (c) V near the first cluster of resonances. The splitting within the first cluster originates from the sensitivity of level|i+1 to the different possible occupation configurations as shown. From Agam et al. [9].

flow through the system. Current first starts to flow when one state i inside the grain becomes available for tunnelling through the left barrier, as illustrated in Fig. 3(b). As the system becomes charged with an additional electron, the potential energy of the other electrons in the dot increases by $U = e^2/C$ and some of the lower-energy occupied electronic states are raised above the right-lead chemical potential (in Fig. 3b these 'ghost' states are shown as dashed lines). Electrons can tunnel out from these states into the right lead leaving the particle in an excited state. There is, however, only one configuration of the electrons that allows an electron to tunnel into level i from the left lead: that is when all the levels are occupied but i. This implies that only a single resonance peak appears in the differential conductance at the onset of the current flow through the system (broken spin degeneracy would cause the splitting of this peak). The situation changes when V increases such that electrons can tunnel from the left lead into the next higher available state $i+1$, as shown in Fig. 3(c). In that case, there are many possible occupancy configurations, on which the exact energy of level $i+1$ depends: when M states are available below the highest accessible energy level and they are occupied by M' electrons, there are $\begin{pmatrix} M' \\ M \end{pmatrix}$ different occupancy configurations. The several possible energies of level $i+1$ lead to a cluster of resonances in the differential conductance of the grain. The scenario described above holds provided that inelastic processes are too slow to maintain equilibrium in the particle.

The increase of the density of tunnelling resonances with energy has also been investigated by Altshuler et al. [10] by studying the relaxation processes in a many-body problem. They find that the interaction of the quasiparticle-decay processes with the many-body eigenstates may lead to the splitting of the resonance associated with a quasiparticle energy level into many peaks in the dI/dV characteristic. Moreover the authors conclude that the width of the resonant peaks changes with energy. This means that the application of a gate voltage (which can shift the energy levels in the particle) may cause the sharpening or broadening of the resonances in the dI/dV characteristic. In accordance with Sivan et al. [11], they also find that the highest energy at which the quasiparticles can be resolved is the Thouless energy E_T (defined by the relation $h/E_T =$ diffusion time through the system).

Zeeman splitting in metallic clusters

Recent experiments have addressed the measurement of the Zeeman splitting of the electronic levels in a cluster under the application of a magnetic field B. The Zeeman splitting of a level ε_μ is described by the formula, $\delta\varepsilon_\mu = \pm \frac{1}{2}\,\mu_B \cdot g \cdot B$, where μ_B is the Bohr magneton. In a free electron gas $g = 2$, but in small metallic grains the effective g-factor may be reduced as a result of spin-orbit scattering [7]. In order to study this reduction Salinas et al. [12] have doped Al grains (which do not have significant spin-orbit scattering) with Au (which has). For small concentration of Au, the effective g-factor was seen to drop from 2 to around 0.7. Lower values $g \sim 0.3$ were reported in a different experiment on Au grains [8]. For disordered particles with spin-orbit scattering, the splitting of a level ε_μ does not only depend on the magnitude of the magnetic field, but also on its direction. Therefore the formula for the Zeeman splitting can be generalised to:

$$\delta\varepsilon_\mu^2 = \left(\frac{\mu_B}{2}\right)^2 \vec{B} \cdot G_\mu \cdot \vec{B},$$

where G_μ is a 3×3 tensor that takes into account the anisotropy of the problem. G_μ is a fluctuating quantity that varies for the different electronic levels ε_μ. The calculation of
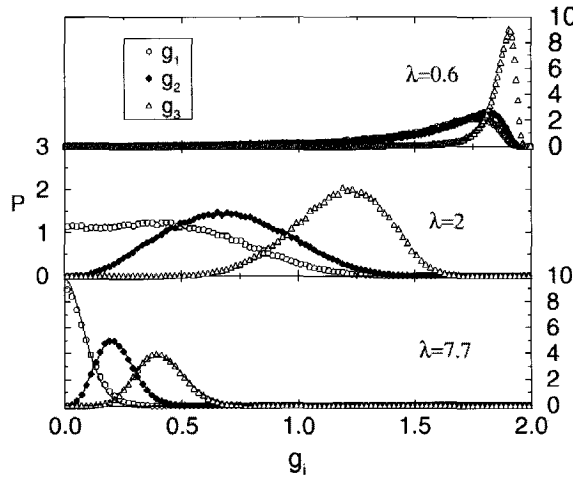
Figure 4: Distributions of the principal g-factors g_i for different strenghts of the spin-orbit coupling. λ is an adimensional parameter proportional to the spin-orbit scattering rate. The data points are obtained by numerical simulation by Brouwer et al. [14].

the statistical distribution of G_μ was performed by Matveev et al. [13] and by Brouwer et al. [14]. The two papers agree on similar conclusions even though the authors of Ref. 13 simply used a scalar approximation for the Zeeman splitting. Brouwer et al. used a random matrix approach to calculate the distribution of the 3 eigenvalues of the G_μ matrix as a function of the spin orbit coupling strength. In Fig. 4 we report their calculated distribution for three different couplings. Lambda is an adimensional parameter indicating the strength of the spin-orbit scattering, defined as $\lambda \sim (\tau_{SO} \cdot \Delta)^{-1/2}$, where τ_{SO} is the spin-orbit scattering time and Δ is mean level spacing. The distributions reported in Fig. 4 are in good agreement with the experiments that demonstrate the suppression of the g-factor [8,12].

Electronic states of small aluminium nanoparticles

A very interesting series of experiments aimed at the study of the electronic properties of colloids have been developed in the recent years by Tinkham et al. We have already mentioned their experimental results on Zeeman splitting [8]. Here, we review their experimental techniques and the results in the seminal papers by Ralph et al. [15,16]. These results are particularly interesting in view of our own measurements on 20-nm gold clusters, which will be the subject of chapter 4.

Figure 5 shows a schematic cross section of the sample of Ref. 16. The authors use e-beam lithography and reactive-ion etching to fabricate a bowl-shaped hole in a
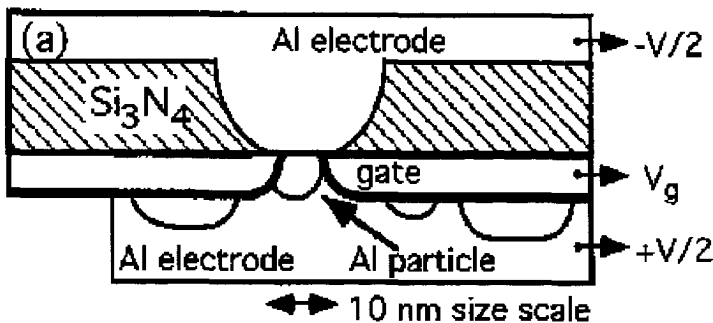
Figure 5: Nanoparticle transistor fabricated by Ralph et al. [16] to measure the three-terminal characteristic of single (evaporated) Al nanoparticles.

suspended silicon nitride membrane, with an opening on the lower edge between 5 and 10 nm in diameter. The gate electrode is formed by evaporating 12 nm of Al onto the flat side of the membrane. Plasma anodisation and deposition of insulating SiO are then used to provide electrical insulation for the gate. Next they form the electrode that fills the bowl-shaped side of the membrane by evaporation of 100 nm of Al, followed by oxidation to form a tunnel barrier near the lower opening of the bowl-shaped hole. A layer of nanoparticles is created onto the lower side of the device by evaporation of 2.5 nm of Al. Due to surface tension the metal beads up into separate grains less than 10 nm in diameter. The last step is the oxidation of the exposed surface of the particle (to form a tunnel junction) and the evaporation of 100 nm of Al to cover it. The authors report on a 25% yield of samples having a single Al grain right on the opening of the bowl-shaped hole. The devices are mounted in a dilution refrigerator, cooled down to 50 mK and then electrically characterised by acquiring *I-V* or *dI/dV* characteristics for different gate voltages. The authors are able to clearly resolve Coulomb blockade in transport and also fit the parameters of the tunnel junctions from the measurements. The most important feature reported in Ref. 16 is the use of the gate, which means: (a) measurements of the electronic spectra for different number of electrons in the particle, (b) improved resolution (see also Ref.
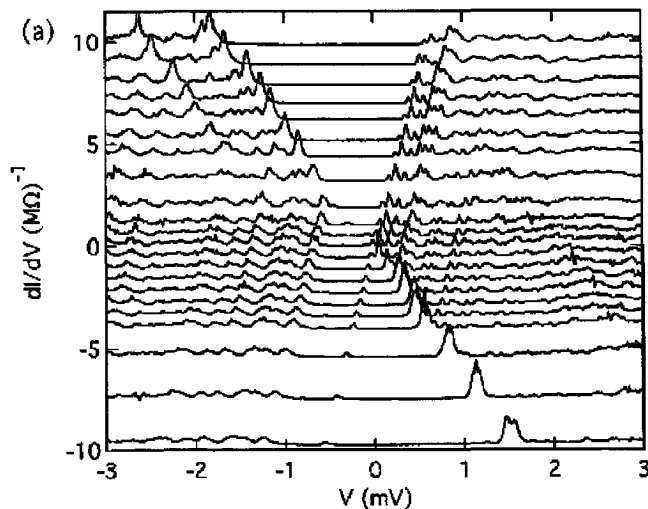
Figure 6: dI/dV vs. source drain voltage plotted for gate voltage ranging from 75 mV (bottom) to 205 mV (top), for the device of Fig. 5 (from Ralph et al. [16]). All data are take for T = 50 mK, H = 50 mT, to drive the Al leads normal. Curves are offset on the dI/dV axis.

10), (c) detailed study of the gate-voltage dependence of the resonance level widths. Figure 6 shows a group of *dI/dV* characteristics taken for different gate voltages. As the gate voltage is increased the extent of the Coulomb blockade region varies between E_c (the charging energy of the grain) to 0. The zero crossing indicates that an electron is added to the particle.

More recently other authors have succeeded to fabricate devices to measure the three-terminal conductance of small particles (or molecules). Notably, Ref. 17 about the transport of Au colloids, Ref. 18 of CdSe nanocrystals and Ref. 19 of a single C_{60} molecule.

References

[1] C. Kittel, *Introduction to solid state physics,* pp 29-50, J. Wiley (1986).

[2] A. L. Mackay, Acta Cryst. **15**, 916 (1962).

[3] W. D. Knight, K. Clemenger, W. A. de Heer, W. A. Saunders, M. Y. Chou and M. L. Cohen, Phys. Rev. Lett. **52**, 2141 (1984).

[4] D.V. Averin et al. Mesoscopic phenomena in Solids, edited by B.L. Altshuler et al. (Elsevier, Amsterdam, 1991), p 169.

[5] A.E. Hanna and M. Tinkham, Phys. Rev. B **44**, 5919 (1991).

[6] P. Hadley, http://vortex.tn.tudelft.nl/research/set and links therein.

[7] W.P. Halperin, Rev. Mod. Phys. **58**, 533 (1986).

[8] D. Davidovich and M. Thinkham, Phys. Rev. Lett. **83**, 1644 (1999).

[9] O. Agam, N.S. Wingreen, B.L. Altshuler, D.C. Ralph and M. Tinkham, Phys. Rev. Lett **78**, 1956 (1997).

[10] B.L. Altshuler, Y. Gefen, A. Kamenev and L.S. Levitov, Phys. Rev. Lett **78**, 2803 (1997).

[11] U. Sivan, F.P. Milliken, K. Milkove, S. Rishton, Y. Lee, J.M. Hong, V. Boegli, D.Kern and M. DeFranza, Europhys. Lett. **25**, 605 (1994).

[12] D.G. Salinas, S. Gueron, D.C. Ralph, C.T. Black and M. Tinkham, Phys. Rev. B **60**, 6137 (1999).

[13] K.A. Matveev et al. cond-mat/0001431 (2000).

[14] P.W. Brouwer et al. cond-mat/0002139 (2000).

[15] D.C. Ralph, C.T. Black and M. Tinkham, Phys. Rev. Lett **74**, 3241 (1995).

[16] D.C. Ralph, C.T. Black and M. Tinkham,. Phys. Rev. Lett **78**, 4087 (1997).

[17] S.H.M. Persson, L. Olofsson and L. Gunnarsson, Appl. Phys. Lett. **74**, 2546 (1999).

[18] D.L. Klein, R. Roth, A.K.L. Lim, A.P. Alivisatos and P.L. McEuen, Nature **389**, 699 (1997).

[19] Hongkun Park, Jiwoong Park, Andrew K.L. Lim, Erik H. Anderson, A. Paul Alivisatos, and Paul L. McEuen *preprint* (2000).

Chapter 3

Scanning probes in mesoscopic physics

Abstract:

Since the invention of the STM in the early 1980s extensive work has been done to apply scanning probe methods to various areas of physics and science in general. Some of these efforts were addressed to combining STM with (mesoscopic) device technology and, consequently, develop a new class of scanning probes. In that perspective the STM can be considered as a scanned probe with only one terminal (the sharp STM tip), while other and more advanced probes present increasingly complex multiterminal configurations. In this chapter we want to review and discuss the most significant developments in the area of scanned probes applied to the study of mesoscopic physics.

Scanning Hall microscopy

The study of the local structure of magnetic fields at the surface of mesoscopic samples is a rich and promising field, with many (potential) applications, such as: the imaging of magnetic domains in magnetic materials, vortices in (high-T_c) superconductors, magnetic clusters, etc. A scanning probe able to measure the magnetic field (flux) is the natural tool for such investigations because it can combine high B-field sensitivity with high spatial resolution. Such an instrument has recently been developed: the scanning Hall microscope (SHM). The SHM consists of an STM-like scanning probe that can measure the magnetic field profile at the surface of a conducting sample by reading out the output of a Hall bar. The SHM is a very sensitive microscope and, to a large extent, it is non-invasive. It has good spatial and magnetic field resolution and it can work in a large range of temperatures and magnetic fields. The first work on a high resolution SHM was published by Chang et al. [1] and applied to the imaging of magnetic bubble domains and of individual vortices in high-T_c $La_{1.85}Sr_{0.15}CuO_4$ films and superconducting networks.

The SHM of Chang et al. (see also Fig. 1) consists of a Hall probe, which is brought into close proximity with the sample surface using STM positioning techniques. The Hall probe is fabricated on a $GaAs/AlGa_xAs_{1-x}$ heterostructure chip just a few
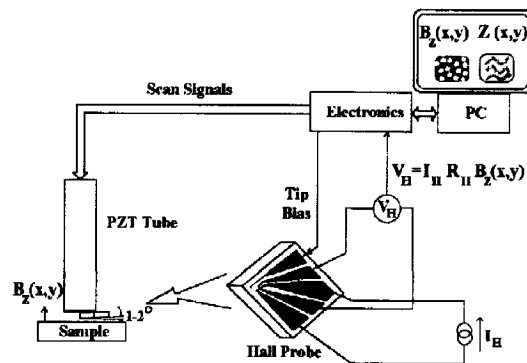
Figure 1: Scheme of the scanning Hall probe (SHM) by Chang et al. [1]. A Hall bar is fabricated on a corner of a chip and mounted as the tip in a STM set-up. The STM electronics and software are used to record the map of the local magnetic field as the Hall bar is scanned over the sample.

micrometers away from the chip corner. First the probe is approached to the sample until a tunnel current is detected and then the Hall probe (retracted a few nanometers away from the sample) is scanned across the surface to measure the magnetic field and the surface topography simultaneously. Gold is deposited on the corner of the chip which is electrically connected to the tip of the STM, allowing a tunnel current to flow between the tip and the sample. The magnetic field is measured using a Hall-bar in a standard four-point measurement configuration (as shown in Fig. 1). More precisely, the SHM measures the Hall resistance of the Hall-bar, which is directly proportional to the magnetic flux through the bar itself. For this reason the most important features for the SHM sensor design are: how close the Hall-bar is to the sample (to maximise the signal) and how small the bar is (to increase the lateral resolution, but at the cost of a decreasing the signal). To have a quantitative idea of the resolution attainable with a SHM we report the specifications for one of the most recent and advanced probes documented in the scientific literature [2].

The magnetic field resolution of the Hall probe measured by Oral et al. is $3.8 \cdot 10^{-6}$ T/Hz$^{1/2}$ at 300 K and $2.9 \cdot 10^{-8}$ T/Hz$^{1/2}$ at 77 K (including the amplifier noise). The flux resolution of the microscope, $\sim 1 \cdot 10^{-5} \Phi_0$/Hz$^{1/2}$ at 77 K (where Φ_0 is the flux quantum) is comparable with the best scanning SQUID systems operating at 4.2 K (see also next paragraph). There is a small $1/f$ noise component with $f_c \sim 10$ Hz. The field resolution at 4.2 K is limited by the voltage noise in the design of Ref. 2: 4 nV/Hz$^{1/2}$ (or $2.2 \cdot 10^{-8}$ T/Hz$^{1/2}$). The frequency response of the Hall probe is flat up to ~ 10 kHz at 77 K and then rolls off with 10 dB/decade. The bandwidth is reduced to 1 kHz if high magnetic field resolution is required. The spatial resolution of the probe is ~ 1 μm. The typical acquisition time per image is of the order of a few minutes in the SHM mode.

Scanning SQUID

Another scanned probe designed to image the surface magnetic field distribution is the Scanning SQUID Microscope (SSM). The SSM, first developed by Vu et al. [3], consists of a superconducting quantum interference device (SQUID) mounted on an STM-like scan-head. Similarly to the SHM, the SSM measures the magnetic flux through its sensor head and it is able to map out complex magnetic field profiles at the surface of flat samples (see Fig. 2 for a scheme of the set-up). The SQUID is the most

sensitive detector of magnetic flux available, which gives the SSM the advantage the highest possible B-field resolution. The drawbacks of this design, comparing for example with the SHM, are that the SQUID is made of superconducting materials which limits the operation of the sensor to low temperatures and also that the area of a SQUID loop is relatively big, which means lower spatial resolution. Typical values for the field and spatial resolution are reported in Ref. 4. The authors find a noise level for their SSM of $2 \cdot 10^{-6} \Phi_0/Hz^{1/2}$ (where Φ_0 is the flux quantum) while the spatial resolution is of the order of 10 μm. Because of such high field and spatial resolutions the SSM has been successfully applied to variety of problems concerning the mapping of the local magnetic field, such as: the imaging of single vortices in High-T_c superconductors [4], the determination of the symmetry of the order parameter in YBCO [5], the imaging of the current distribution in integrated circuits [6] and the measuring of (local) radio-frequency fields [7].
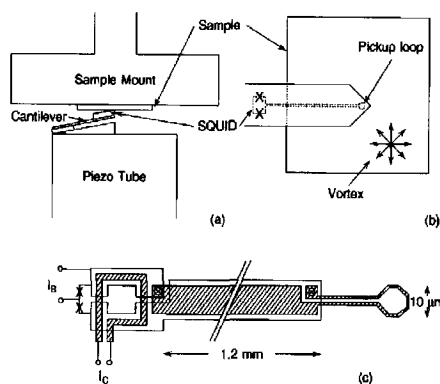
Figure 2: Scheme of the scanning squid microscope (SSM) by Kirtley et al. [4]. (a) The squid, fabricated on a cantilever, is mounted on a piezotube to scan it over the surface of the sample. (b) An expanded view of the squid-sample configuration. (c) A schematic layout of the single-chip magnetometer.

Scanning quantum point contact

In the previous paragraphs we have discussed the design of two microscopes, which can measure magnetic fields a spatial resolution of the order of 1 μm and, at the same time, are relatively non-invasive toward the measured sample. It is natural to pose the
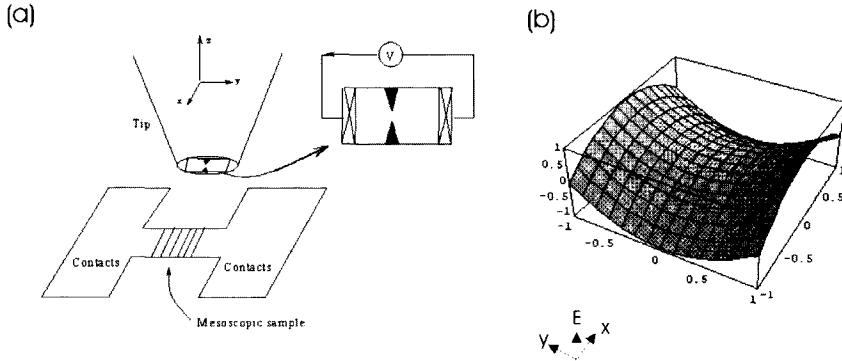
Figure 3: (a) Scheme of the scanning quantum point contact microscope (S-QPC). A QPC is fabricated on a chip and scanned over the mesoscopic sample. (b) Plot of the model potential for a QPC: electrons tunnel from left to right (on the x-axis) mainly from the saddle point of the potential (at the origin of the axis).

question of how to realise scanning probes that can measure electric fields with similar performances. A large range of phenomena of great interest would then be observable, just to mention a few: investigation of the quantum Hall condensate spatially resolved, visualisation of the Friedel oscillations in semiconductors, measurement of the vortex charge in superconductors, imaging of hydrodynamic effects in the electronic transport, etc.

In this paragraph we report on our design and implementation of a scanning probe for measuring local electric fields based on the properties of microfabricated quantum point contacts (QPC). The design of the scanning QPC (S-QPC) microscope is in many ways similar to the SHM and SSM discussed in the previous paragraphs: a sensor element (in this case a QPC) is mounted on top of a piezotube and scanned over the surface of the sample. A scheme of the S-QPC is shown in Fig. 3a.

The QPC is a quantum device consisting of a narrow slit fabricated on top of a two-dimensional electron gas. The conduction of the device can be tuned by varying the width of the slit. In fact, the conductance as a function of the slit width has a staircase-like behaviour, where the step height is an integer multiple of the conductance quantum $2e^2/h \sim 13$ KΩ^{-1} [8]. The explanation of this phenomenon is that when the slit aperture is of the same order of magnitude as the wavelength of the electrons that have to pass through it, there are only a few (integer) number of allowed transmission

modes and each of them can be demonstrated to contribute to the conductance with a conductance quantum. When the slit is so narrow that the number of allowed modes is zero, the device still has non-zero conductance because of another quantum effect: tunnelling through the slit. In this regime the QPC can be used as an electrometer. A simple explanation of that can be obtained considering the graph of the potential-barrier profile in the QPC as a function of the in-plane spatial coordinates (x,y). In first approximation the potential can be represented by a saddle-like function $V = V_0$ $((x/a)^2 - (y/b)^2)$ [8], as shown in Fig. 3b. A distinctive property of quantum tunnelling (see also chapter 1) is that the tunnelling rate through a potential barrier is roughly exponentially dependent on the barrier height and width. This means that tunnelling through the QPC occurs almost entirely in the proximity of the saddle point of the $V(x,y)$ function where the potential barrier is smaller (the $(0,0)$ point in the graph of Fig. 3b). The application of a small external field $V_{ext}(x,y)$ can change the potential profile, but the current will still flow from the saddle point of the potential (which can be slightly moved though). Nevertheless, the conductance of the QPC can vary significantly with the application of an external field, because the tunnelling rate is (roughly) exponentially dependent on the value of the potential barrier at the saddle point. The use of a QPC as an electrometer has been first reported in literature [9] using a on-chip geometry. The authors have fabricated a QPC on a 2DEG and have used it to measure the charge fluctuations (of the order of 1 e) on an electrode located 1 μm away from the QPC opening.
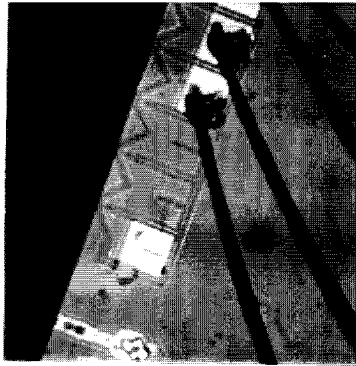
Figure 4: Picture of the S-QPC device. A row of point contacts, with different aperture widths, have been fabricated by e-beam lithography at the edge III-V heterostructure with a shallow 2DEG. The point contacts are used as electrometers in a scanning probe experiment.

The main experimental challenges to make a working S-QPC concern the alignment of the QPC device to the sample to be measured. An STM-like geometry, for example, would require the fabrication of a QPC at the apex of the tip. This is very hard to implement, mainly because it would be difficult to grow a two-dimensional electron gas on a curved substrate. A planar geometry is a much more viable alternative, with the drawback, though, that it requires a very accurate alignment procedure in order to scan two flat surfaces over each other. Figure 4 shows a picture of the device we have made to test the principle of S-QPC. A series of point contacts have been fabricated on a high mobility shallow 2DEG at about 20 μm from the edge of the $GaAs/Al_xGa_{1-x}As$ substrate. To fabricate a device so close to the sample we had to take the extra care of spinning the resist before cleaving of the substrate, so that a uniform layer was available near the edge were we want to fabricate the QPCs by e-beam lithography. Different QPCs were fabricated in one device, with different apertures and, thus, conductances. The S-QPC was tested by approaching a metal film on top of it using a standard STM set-up. Special care was taken to align the QPC and metal film surfaces using a laser alignment system able to reach alignment better than 1^0. Once the film and QPC were close together we applied a voltage to the metal film and measured the changes in the QPC conductance. Only a small change of conductance was measured, because it was not possible to reach an adequate level of parallelism between the S-QPC and the metal film, which was actually touching the sample far away from the QPC. We conclude that the scanning QPC is in principle a viable technique, but further technological developments are needed to make it useful to mesoscopic experiments. Within our design, it is necessary to (1) improve the alignment system between tip and sample and (2) find a way to fabricate the point contacts much closer to the end of the tip, e.g. at a distance of 1 μm or less.

Scanning SET

A very important result in the development of scanning probes able to image the electric field at the surface of a sample with very high resolution was obtained by Yoo et al. [10] with the invention of the scanning single-electron transistor (S-SET). The S-SET microscope uses a single electron transistor to sense the electrically induced charge on its small (100 nm) metal island held in proximity of the sample surface (see

Fig. 5). The advantage of this design lies in the high resolution of the SET sensor, for example, it has enough sensitivity to detect the charge of one electron at 1 μm of distance. Moreover, one can assign a quantitative interpretation to the S-SET signal, because all the important geometrical parameters of the sensor are known. Another advantage is that the operation of the S-SET does not require the application of intense electric fields between the tip and surface, which is particularly important for the study of systems that can be easily perturbed by external fields, such as semiconductors. All these features make the S-SET a very important tool for exploring a whole new class of phenomena in mesoscopic physics.

In particular Yoo et al. have applied the SSET to measure the silicon photo-ionised dopants of a Ga/Al$_x$Ga$_{1-x}$As heterostructure [10]. Moreover, the S-SET has been applied to the study the quantum Hall state at the submicron scale by Yacoby et al. [11], who have used a S-SET to image the local electron compressibility of the Hall liquid. They were able to identify regions with different compressibility, which they interpreted as the experimental evidence of the incompressible strips associated with
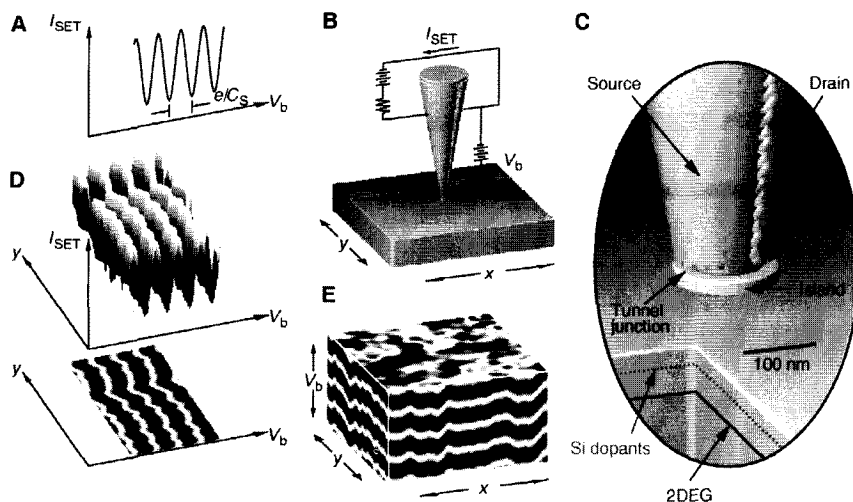
Figure 5: Scheme of the functioning of the scanning single electron transistor (S-SET) by Yoo et al. [10]. (A) Typical current oscillations I$_{SET}$(V$_b$) of a SET. (B) Schematic depiction of the SET probe tip suspended above the GaAs/Al$_x$Ga$_{1-x}$As heterostructure. (C) Magnified view of the tip and cutaway view of the sample. (D) I$_{SET}$(V$_b$) vs. y for a 2-μm line scan; (top) 3D representations after (A); (bottom) 2D greyscale representation of the same data. (E) Greyscale representations of a complete data set I$_{SET}$(V$_b$) vs. (x,y) for a 2×2 μm^2 raster scan over a non-gated region. The top of the data block maps the electric field of the sample surface as detected by the SETSE. The side of the block is taken from (D).

the edge states, as predicted by the most recent theories of transport in the quantum Hall state. More recent work on the same subject [12] has produced clear imaging of localised states in the quantum Hall liquid, also expected from the theory.

The SET is a submicrometer-sized tunnelling device whose current flow is governed by the Coulomb blockade effect. It consists of a small metallic island connected to the source and drain leads by two small tunnel junctions. The current tunnels through the junctions at a rate determined, among other factors, by the island's electrostatic potential with respect to the source and drain. This potential is in turn controlled by the electric field that the island experiences from the external sources, such as fixed charges or capacitively coupled electrodes on a nearby sample (see also Fig. 5C). At low temperatures and for the appropriate voltage bias, the current flowing through the SET fluctuates periodically as this electric field increases. In fact, the current passes through a full period each time the electric field lines terminating on the island induce a charge of exactly one additional electron (see Fig. 5A and 5D). Hence, monitoring the current through the SET as it is scanned over the sample, provides a map of the electric field emanating from the sample surface or, more accurately, a measurement of the electric flux terminating on the tip island.

The fabrication of the SET involves the evaporation of three separate areas of a thin (10 to 20 nm) aluminium film onto a specially shaped glass fibre. The end of the fibre has a shallow conical taper that terminates at the tip in a flat, nearly circular area ~100 nm in diameter (Figs. 5B and 5C). A circular patch of film covering the tip constitutes the field-sensitive island. The films for source and drain leads spread out from the edges of the tip and extend up the sides of the fibre to electrical contacts. The source and drain leads are deposited first by separate evaporations from the side and rear. After an *in situ* exposure to oxygen that creates the oxide tunnel barriers, a final end-on evaporation deposits the island and forms the tunnel junctions. The shapes of the three electrodes are defined by natural shadowing.

Yoo et al. [10] have used the S-SET to image individual electron charges on silicon photo-ionised dopants on a $Ga/Al_xGa_{1-x}As$ heterostructure. Subtracting the signal measured before and after illumination of the sample they could image the charged dopants as small circular dots of apparent size ~100 nm. The spatial resolution being limited by the size of the SET island.

Design of a scanning SET on a SiN cantilever
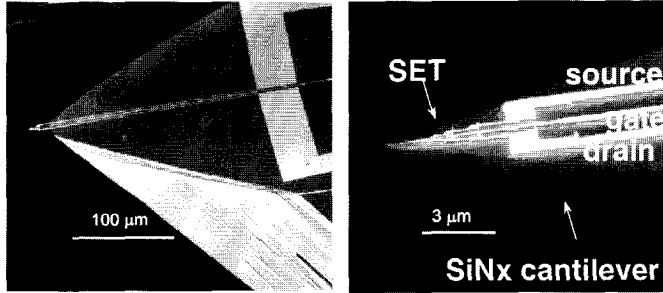
Figure 6: SEM pictures of our design for a scanning SET on a silicon nitride cantilever. The source, drain and gate electrode are nanofabricated with e-beam lithography. A metallic island is also fabricated at the sharp end of the cantilever.

The experiments of Yoo et al. discussed in the previous paragraph show the great potential of the S-SET probes as a tool for the study of mesoscopic phenomena. The major limitation of their design being the large diameter of the SET island, which can hardly be pushed below the limit of 100 nm using an optical fibre as a substrate. We have developed a new design consisting of a silicon nitride cantilever over which a SET is nanofabricated by e-beam lithography. Figure 6 shows a SEM image of such a probe. The SET island-electrode can be fabricated smaller than in the work of Ref. 10, thus improving the spatial resolution of the sensor. Moreover, a colloid can in principle be attached to the end of the cantilever and used as the SET-island, consequently allowing the device to work even at room temperature. We have developed a fabrication recipe for the S-SET probes, which presents many similarities with the one for the S-gate (which will be the subject of chapter 5). Figure 7 shows a scheme of the fabrication recipe for the S-SET [13]. The first step (a,b) is the preparation of the 'bridge' SiN membrane by optical lithography and reactive ion etching using CHF_3. (c,d) Then the SET is written by means of e-beam lithography and shadow-mask evaporation (e,f). The SSET is etched away from the substrate. Although we could fabricate an SET at the end of a sharp cantilever, as shown in Fig. 6, the device was not working properly because the source and drain junctions were blown up probably by the dry etching step (step e). At present we are looking at ways
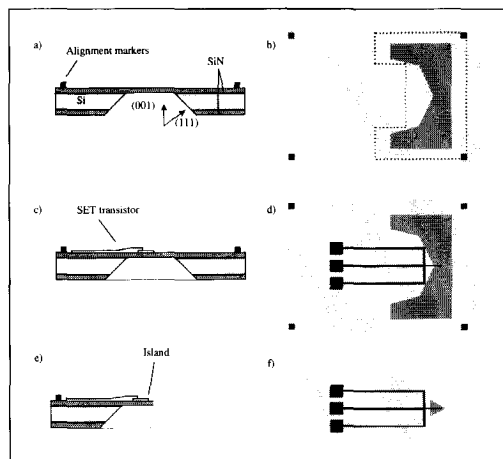
Figure 7: Fabrication process of a SET transistor. a) A silicon nitride membrane is defined by means of optical lithography and wet etching. c) The scanning SET is written with e-beam lithography and defined with the method of 'shadow mask' evaporation. e) The S-SET is (dry-) etched away from the substrate. (b,d,f) are the top views of (a,b,c) respectively.

to improve the fabrication so that we can have a working SET after all the fabrication steps.

Scanning potential microscopy

A typical experiment of mesoscopic physics involves the study of the conductance of a sample as a function of the potential applied to one or more gate electrodes. In order to combine this method of investigation with the accurate positioning capabilities of STM, Eriksson et al. [14] have developed a new scanning probe: the scanning potential microscope (SPoM). As shown in Fig. 8a the SPoM consists of an AFM with a conducting tip that can be polarised with an external bias: the conductance of the sample can be measured as the tip is scanned over the sample as a movable gate. A conducting AFM tip can be utilised (roughly) to perform the same tasks as an STM tip, but with a major difference: the feedback loop for an AFM tip is on the force signal, while for the STM is on the tunnel current. This means, for example, that the SPoM can be used to investigate both insulating and conducting surfaces.

Eriksson et al. [14] have used the SPoM to image the change of conductance of a point contact as the charged SPoM tip is scanned over the sample. The authors have fabricated a ballistic point contact on a $GaAs/Al_{0.3}Ga_{0.7}As$ heterostructure containing a 2D electron gas (2DEG) buried ~50 nm beneath the surface. Low temperature Hall measurements determined the electron mean free path $l_e \approx 5$ μm. The point contact was defined via electron beam lithography with a width of ~3 μm and resistance ~100 Ω. Using the SPoM the authors were able to acquire simultaneously the topography of the sample and a map of the conductance. Figure 8b shows a combined plot generated from the topographic image of the etched-away areas of the point contact and the map of the conductance. The conductance image was obtained applying an ac voltage ~0.5 V_{rms} at 400 Hz between the 2DEG and the tip. The capacitive coupling between the tip and the 2DEG induces a local modulation of the potential, which deflects the electrons passing through the ballistic point contact.

More recently, the SPoM has been applied to the study of the electronic structure of nanotube devices. Tans et al. [15] have used a conducting AFM tip as a movable gate to study the internal potential of a semiconducting carbon nanotube by scanning the tip over it and simultaneously measure the electrical conductance of the tube.

The SPoM has also been used to study the edge and bulk currents [16] and the inter-edge scattering centres [17] in the quantum Hall regime. The quantum Hall effect remains one of the most interesting phenomenon in mesoscopic physics, as shown by
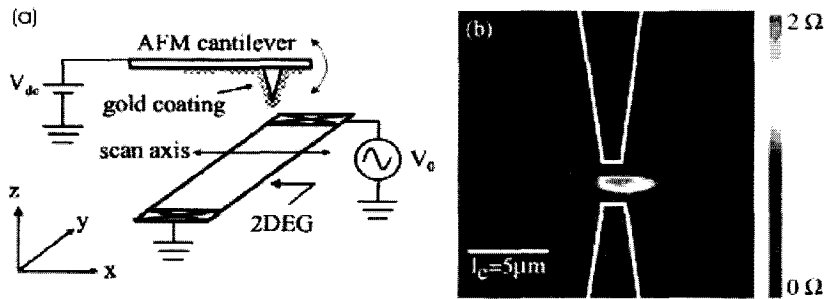
Figure 8: (a) Scheme of the scanning potential microscope. A conducting AFM cantilever is scanned over a sample (e.g. a 2D electron gas). The conductance of the sample can be measured as a function of the lateral displacement of the tip. (b) The scanning potential microscope is scanned over a point contact. When the tip is above the opening of the point contact, the conductance is modulated by the external electric field induced by the tip. From Eriksson et al. [14].

the two Nobel prizes given for researches in the field. Nevertheless yet many controversies and subtle effects on this subject still have to be solved. One important topic, which has been debated over the years, is the existence and the role of the so-called 'edge channels' as the transport mechanism in the quantum Hall regime. Edge channels are extended states that form along the sample edge due to the effect of the confinement potential on the Landau level energies.

To investigate these issues, McCormick et al. [16] have used an SPoM to probe the Hall voltage across a Hall bar for different magnetic field. They find that when the filling factor is close to an even integer value 4, 6, 8, ... the Hall voltage perpendicular to the current, shows an irregular behaviour, while a simple linear I-V characteristic is measured for other values of B. Moreover, the authors have measured the local potential $V(x,y)$ near the edge of the sample and found a very irregular pattern near integer filling four. These observations are in agreement with a picture of the edge channels forming for values of the external field B at plateaux of the Hall effect. The explanation of the authors is that: as the topmost Landau level becomes conducting for values of B in between quantum Hall plateaux. In that case the bulk and edges of the sample are well equilibrated and the Hall profile is linear throughout the sample. As the field is increased through the transition region, the local voltage drop that develops at the edges indicates a width of the edge features that increases as the number of edge states increases. For example the edge state at filling 2.5 has a width of ~300 nm, very close to the resolution of their AFM. A more clear interpretation of their experiments would be possible if the authors could increase the spatial resolution of their probe. Similar techniques have also been used by Woodside et al. [16] to obtain the first direct measurement of the amount of edge state coupling to individual scattering sites. This confirms that the SPOM is a valuable tool for probing inhomogeneous microscopic structures in quantum Hall conductors.

It is particularly interesting to compare the SPoM technique with the experiments with the scanning gate, which will be the subject of chapter 4. To appreciate better the differences and similarities we want to briefly give a quantitative description of what is measured with the SPOM, following Ref. 16. Figure 8a shows the scheme of their measurements: they have used a low-temperature AFM operating in non-contact mode. An AC potential V_0 was applied to the contacts of the sample, producing inside the sample the AC potential $V(x,y)$, whose distribution was measured. The local

potential $V(x,y)$ interacts electrostatically with the sharp, metallised AFM tip, deflecting the AFM cantilever with a force that can be modelled as:

$$F_{ac}(x,y) = \frac{dC}{dz}(V_{dc} + \Phi)V(x,y),$$

where F is the force on the tip, C is the tip-sample capacitance, z is the tip-sample separation, V_{dc} is the voltage applied between tip and sample and Φ is the contact potential difference between tip and sample material. Therefore, the measured force on the tip, F, is directly proportional to the local potential $V(x,y)$ within this model.

Tessmer et al. [18] have developed another STM-like technique to investigate the inhomogeneous charge distribution on a quantum Hall fluid and they called it subsurface charge accumulation (SCA) imaging. The SCA measures the local accumulation of charge in a two-dimensional electron system (2DES) in response to
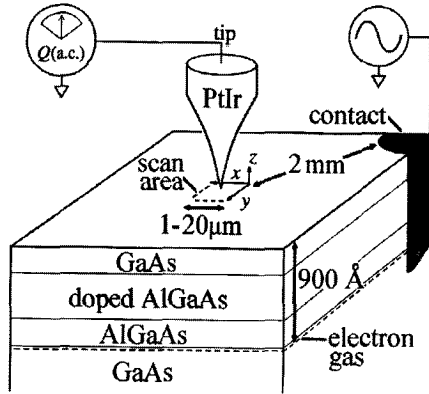
Figure 9: Diagram of the sample and measurement configuration. The two-dimensional electron system (2DES) exists at the interface of $Al_{0.3}Ga_{0.7}As$ and GaAs 900 Å beneath the surface. The a.c. excitation applied to the 2DES causes this layer to charge and discharge due to the self-capacitance of the layer. A sharp metal tip is connected to a high electron mobility transistor (HEMT) with extremely high sensitivity to electrical charge[30] (0.01 electrons Hz) and scanned 50 Å above the sample surface. SCA microscopy produces an image of charge accumulating in the 2DES by detecting charge induced on the tip due to charging in the layer. The spatial resolution is given approximately by the depth of the 2DES below the sample surface. The microscope operates with the sample immersed in liquid ^{3}He (T = 300 mK) and has a 20-μm-long scan range. The static electron density in the 2DES is 3.0×10^{11} cm^{-2} and the transport mobility is 450,000 cm^2 V^{-1} s^{-1}. The small amplitude of the 100 kHz excitation applied to the 2DEG (1–4 mV) and the smallness of the capacitance between the tip and the 2DES (compared to the self-capacitance of the 2DES) ensure that the tip produces practically no perturbation of the 2D system. From Tessmer et al. [18].

an AC excitation. The authors have used it to examine the quantum Hall system over areas as large as 1 μm, and with a spatial resolution of about 100 nm. For magnetic fields near the Hall plateaux they find that some fine structure appears in the SCA images. These structures are seen to change rapidly as the field was varied, even though they reappear on the successive Hall plateau. The SCA works as follows: a sharp conducting tip is positioned ~5 nm above the sample surface using STM feedback system. An AC voltage is applied to the 2DES buried ~100 nm below the surface, through an ohmic contact. The AC excitation causes charge to flow in and out the 2DES, in turn inducing charge to flow in and out the tip. The tip is connected to a highly sensitive charge detector and a lock-in to measure the in-phase and 90^0 out-of- phase charge. As a test of their microscope (before studying quantum Hall features), Tessmer et al. have used it to locally perturb the 2DES. If large voltages (>2 V) are applied to the tip, static and immobile charge can be deposited on the exposed surface of the sample or in the donor layer between the surface and the 2DES, thereby locally altering the electron density in the 2DES. In fact, among the methods to study the quantum Hall effect reviewed in this chapter, the SCA is the most invasive, since it makes use of a sharp metal tip very close to the sample. In more recent work Finkelstein et al. [19] have applied the SCA to study in detail the incompressible strips around filling factors 2 and 4. The authors of Ref. 19 have also developed a more sophisticated theory to explain the SCA measurements taking into account tip-induced effects.

References

[1] A.M. Chang, H.D. Hallen, L. Harriott, H.F. Hess, H.L. Kao, J. Kwo, R.E. Miller, R. Wolfe, J. van der Ziel and T.Y. Chang, Appl. Phys. Lett. **61**, 1975 (1992).

[2] A. Oral, S.J. Bending and M. Henini, Appl. Phys. Lett. **69**, 1324 (1996).

[3] L.N. Vu, M.S. Winstrom, D.J. van Harlingen, Appl. Phys. Lett. **63**, 1693 (1993).

[4] J.R. Kirtley, M.B. Ketchen, K.G. Stawiasz, J.Z. Sun, W.J. Gallager, S.H. Blanton and S.J. Wind, Appl. Phys. Lett. **66**, 1138 (1995).

[5] A. Mathai, Y. Gim, R.C. Black, A. Amar and F.C. Wellstood, Phys. Rev. Lett. **74**, 4523 (1995).

[6] R.C. Black, F.C. Wellstood, E. Dantsker, A.H. Milklich, D. Koelle, F. Ludwig and J. Clarke, Appl. Phys. Lett. **66**, 1267 (1995).

[7] S. Chatraphorn, E.F. Fleet, F.C. Wellstood, L.A. Knauss and T.M. Elles, Appl. Phys. Lett. **76**, 2304 (2000).

[8] B.J. van Wees, H. van Houten, C.W.J. Beenakker, J.G. Williamson, L.P. Kouwenhoven, D. van der Marel and C.T. Foxon, Phys. Rev. Lett. **60**, 848 (1988).

[9] M. Field, C.G. Smith, M. Pepper, D.A. Ritchie, J.E.F. Frost, G.A.C. Jones and D.G. Hasko, Phys. Rev. Lett. **70**, 1311 (1993).

[10] M.J. Yoo, T.A. Fulton, H.F. Hess, R.L. Willett, L.N. Dunkleberger, R.J. Chichester, L.N. Pfeiffer and K.W. West, Science **276**, 579 (1997).

[11] A. Yacoby, H.F. Hess, T.A. Fulton, L.N. Pfeiffer and K.W. West, Solid State Commun. **111**, 1 (1999).

[12] N.B. Zhitenev, T.A. Fulton, A. Yacoby, H.F. Hess, L.N. Pfeiffer and K.W. West. Nature **404**, 473 (2000).

[13] H. de Wit *Afstudeerverslag*, TU Delft 1998.

[14] M.A. Eriksson, R.G. Beck, M. Topinka, J.A. Katine, R.M. Westerveld, K.L. Campman and A.C. Gossard, Appl. Phys. Lett. **69**, 671 (1996).

[15] S.J. Tans and C. Dekker Nature, Nature **404**, 834 (2000).

[16] K.L. McCormick, M.T. Woodside, M. Huang, M. Wu, P.L. McEuen, C. Duruoz and J.S. Harris Jr., Phys. Rev. B **59**, 4654 (1999).

[17] M.T. Woodside et al. *preprint* (2000).

[18] S.H. Tessmer, P.I. Glicofridis, R.C. Ashoori, L.S. Levitov and M.R. Melloch Nature 392, 51 (1998).

[19] G. Finkelstein, P.I. Glicofridis, S.H. Tessmer, R.C. Ashoori and M.R. Melloch, Phys. Rev. B **61**, R16323 (2000).

Chapter 4

Scanning Gate Probes Applied to the Study of Metallic Clusters

L. Canali, L. Gurevich and L. P. Kouwenhoven

Abstract:

In this chapter we discuss the application of the scanning gate probes to the study of small metallic particles. We present the spectroscopic measurements taken with a scanning gate probe on 20-nm gold clusters at low temperatures. Such data provide a good model system to test and interpret the functioning of the scanning gates in the framework of the orthodox theory of single electronics. We are able to derive from the measurements the values of the most relevant experimental parameters of the scanning gates, such as the gate-to-particle capacitance.

Introduction to S-gate measurements on clusters

Since the first experiments of Binnig and Röhrer, the STM has become one of the most valuable tools for the physicists interested in studying the properties of solids at the smallest possible scale, ultimately that of molecules and atoms. In the last decade, for example, the STM has been successfully applied to the investigation of the atomic structure of metallic surfaces, the study of single molecules deposited on conducting surfaces and their (nano) manipulation. The STM has thus proven to be a very versatile instrument in spite of its intrinsic simplicity: it is basically formed by 5 computer-controlled low-noise high-voltage amplifiers piloting a piezotube with a sharp metallic tip mounted on top. The STM is mainly limited by having only one controllable contact, used both for imaging and for acquiring the spectroscopic characteristic. We have already discussed in chapter 3 a series of new scanning probes that have recently appeared in the scientific literature. They all aim to extend and complement the STM by including extra features, which necessarily need extra controllable electric terminals connected to the probe. In this chapter we discuss the functioning of another such device that we called the "Scanning Gate Probe" (S-gate for short). The S-gate is conceptually the simplest extension of the STM: it consists of two metallic contacts, closely spaced but electrically isolated from one another. Chapter 5 contains a detailed description of how we fabricate the S-gates. In the following paragraphs we describe an experiment where the S-gates have been utilised
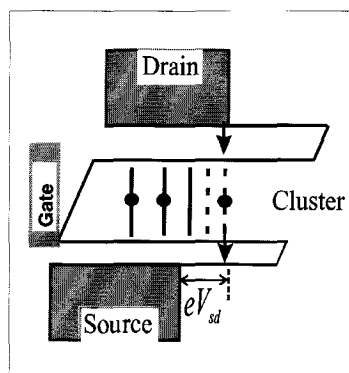
Figure 1: Scheme of the measurements for a double barrier system (e.g. a cluster or a quantum dot). Typically the cluster under investigation is contacted by two electrodes, normally called source and drain, while a third electrode (the gate), is used to modify the transport properties of the particle.

to study the electronic spectrum of metallic nanoparticles.

The study of nanoscale particles generates a large interest in fundamental physics because it unveils one of the most striking and at the same time basic phenomena of quantum mechanics, which states that when a particle is confined to a length scale of the order of its wavelength then it will interfere with itself and manifest a discrete energy spectrum of allowed energy levels. This is a direct consequence of Heisenberg's uncertainty principle, which can be written in more precise mathematical terms as $[x, p_x] = i\ h/2\pi$, where x and p are the position and momentum operators and h is Plank's constant. This principle has been proven experimentally in many ways: for instance a particularly clear verification of it became possible since the 1970s when experiments with systems of reduced dimensionality were first realised [1]. The most relevant experiments of that kind, for our purposes, are the demonstrations of the effects of localisation in quantum mechanics measured on systems of 'zero dimensionality' (also called quantum dots). We especially want to refer to the transport measurements on low-dimensional systems and understand their rationale [2].

Typically, the quantum dot under investigation is contacted by two electrodes, normally called source and drain, while a third electrode, called gate, is used to modify the conducting properties of the dot. The scheme of such measurements is
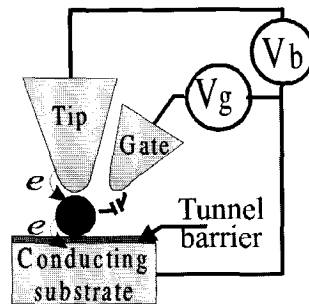
Figure 2: Scheme of the three-terminal measurement of a metallic cluster with a S-gate probe: the tip electrode is used to acquire STM imaging of the sample and locate the particles scattered on the surface. The STM tip is moved atop one selected particle: the STM electronics can be used to stabilize the tip for the desired tunnel resistance. The tip and substrate are used as source and drain electrodes, the third electrode acts as gate. Note that a tunnel barrier has to be present between the particle and the conducting substrate.

represented in Fig. 1. Electrons are emitted from the source electrode into the particle by a tunnelling process (providing that the barrier has a resistance higher than the resistance quantum $h/2e^2 \sim 13$ kΩ). From there they tunnel off into the drain electrode. The probability for an electron to tunnel into the particle is zero if there are no states available in the given energy-window of the particle, in that case the transport is blocked and no current can flow. Conversely, when an extra resonant channel (energy window) opens up for the electronic transport, a peak will be measured in the conductance. See also chapter 2 for a more detailed discussion.

Figure 2 shows how we implement 3-terminal measurements using the S-gate probe: (1) the tip electrode is used to acquire STM imaging of the sample to locate the particles scattered on the surface. (2) The STM tip is moved atop one selected particle. The STM electronics can be used to stabilize the tip for the wanted tunnel resistance. (3) The tip is used as source electrode for the electrons, the substrate is the drain and the second electrode on the chip is used as the electronic gate. Note that a tunnel barrier has to be present between the particle and the conducting substrate (see also chapter 7). (4) A set of I-Vs can be acquired for different gate voltages, and plotted in a single graph (called stability diagram). From the stability diagram we can calculate the values of the capacitances and resistances of the double-barrier system tip-particle-substrate (see also chapter 2).

Au clusters on Pt substrate

The sample we measured was prepared by depositing 20-nm Au clusters on a substrate of sputtered platinum with a monolayer of cysteamine on top (see also chapter 7). Figure 3 shows a low temperature STM topography of the sample, obtained with a S-gate cantilever. The greyscale plot represents a map of the STM tip height above the sample (black means that the tip is stretched towards the sample). Good contrast can be observed between dark areas (which show a granular structure) and smaller areas of brighter shades of grey. By comparing Fig. 3 with other topographies of similar samples but without the cysteamine monolayer and/or clusters, we conclude that the dark area is a topographic image of the platinum film. The granular structure visible in Fig. 3 (with a period of about 5 nm and a peak-to-peak amplitude of 1 nm) is an intrinsic feature of the film. This way we have also
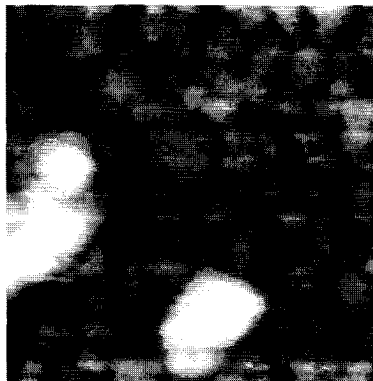
Figure 3: 100x100 nm STM topography at 4.2 K. The substrate is sputtered Pt covered with a monolayer of cysteamine. Au 20-nm clusters, deposited from solution, are visible as white spots on the topography.

proven that the cysteamine layer is 'transparent' to STM topography even at low temperatures, i.e. it does not interact in an observable way with the tip. The brighter areas in Fig. 3 are images of the 20 nm clusters.

We conclude that because: (a) samples with Pt+cysteamine layer do not present such features. (b) The measured height of those areas is of the order of 20 nm. (c) Their spectroscopy is consistent with what we expect for metallic particles of that size. The diameter of the particles appears to be larger than the expected 20 nm. That can be explained as a result of tip-convolution, which means that the S-gate tip apex is round and cannot image objects smaller than its diameter (see also chapter 1). Moreover some colloids are most probably grouped together since they appear stretched in the topography.

Spectroscopic measurements

Figure 4 shows two *I-V* characteristics obtained on a single 20-nm gold cluster. The I-Vs have a ladder-like shape, as expected from the orthodox theory of Coulomb blockade in the case of asymmetric junctions [3] (and $E_C > k_B T$; see chapter 2 for a detailed discussion on the physics of Coulomb charging).
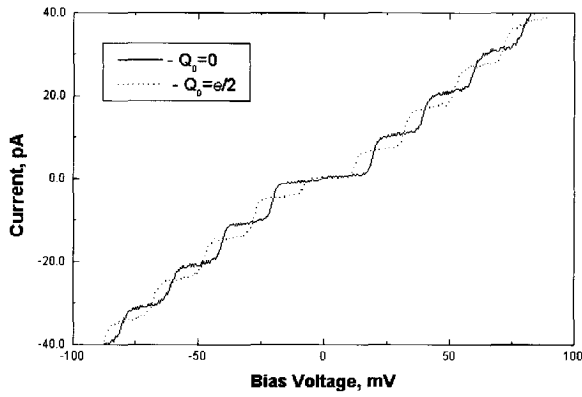
Figure 4: Tunnel current vs. bias voltage for two different gate values (solid line: V_g = 2.4 V; dotted line V_g = 15.6 V), such that the offset charge on the cluster Q_0 is changed by about e/2.
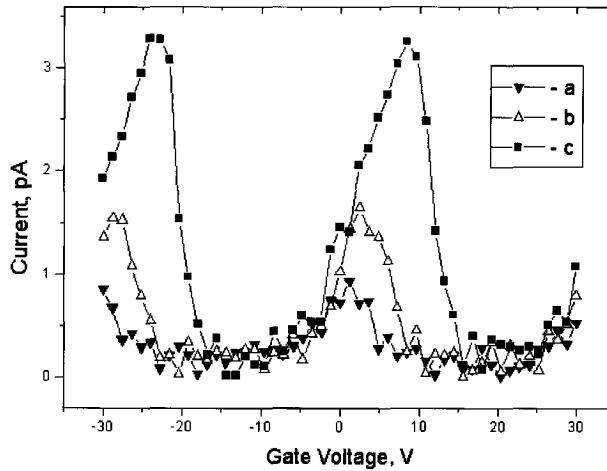
Figure 5: Tunnel current vs. gate voltage spectroscopy, for a fixed bias value V_b (line a: V_b = 2.4 mV, line b: V_b = 4.4 mV, line c: V_b = 8.4 mV). Gate-to-cluster capacitive coupling (C_g) can change the charge in the cluster causing current oscillations (with period e). From the measurements we find $Cg \sim 5 \cdot 10^{-21}$ F.

It is difficult to predict the exact value of the charging energy E_C, because the precise shape of the particle and configuration of dielectrics around it are not known, nevertheless we can estimate $E_C \sim 10$ meV for a metallic particle of 20 nm in diameter. The measured width of the steps (and thus the charging energy of the particle) is 15 meV, in accordance with the expectations. The effect of the gate electrode can be seen in Fig. 4: two different *I-V*s taken with different gate voltages are plotted, corresponding to offset charges on the cluster $Q_0 = 0$ and $e/2$. Another way to illustrate the effect of the gate can be seen in Fig. 5, where three graphs of current I vs. gate voltage V_g are shown for three different values of the bias. The current is periodic in V_g, where each period corresponds to an induced charge on the gate $\Delta Q_0 = e$.

The graphs of Figs. 4 and 5 represent a subset of a larger set of data consisting of 51 *I-V*s taken for V_g varying from -30 V to +30 V. Ideally the measurement should be taken (1) with the STM tip fixed on top of the particle, (2) the STM feedback loop turned off and (3) by sweeping the bias and gate voltages slowly enough not to cause any jump in the offset charge of the cluster. It is normally rather difficult to maintain the STM current very stable for a long time with the feedback loop turned off. Many sources of noise can couple into the experiment during such a time span, mainly mechanical noise (such as noise from the pump-lines, ambient noise, LN_2 boil) or drift (see also chapter 1 for a discussion of the effects of noise on STM). For that reason we have written a program to acquire spectroscopy, this way we can stabilise the STM tip in between each I-V and also control the sweeping of the gate voltage. The program takes advantage of an advanced facility of the software of our control unit [4], which allows an external program to take full-control of the inputs ADCs and output DACs by linking a dynamic (ActiveX^{TM}) library.

Our program acquires three-terminal spectroscopy as follows: before each I-V curve, the STM tip is stabilized by the feedback loop with bias voltage $V_b = 100$ mV, tunnel current $I_T = 50$ pA and gate voltage $V_g = 0$. Then the feedback loop is turned off and the gate voltage is swept to the intended value. Afterwards the I-V data points are acquired and the gate voltage is swept back to zero. The feedback is then turned on again, to stabilize the STM tip, and the program proceeds to acquire the next I-V. Each I-V takes about 30 sec.
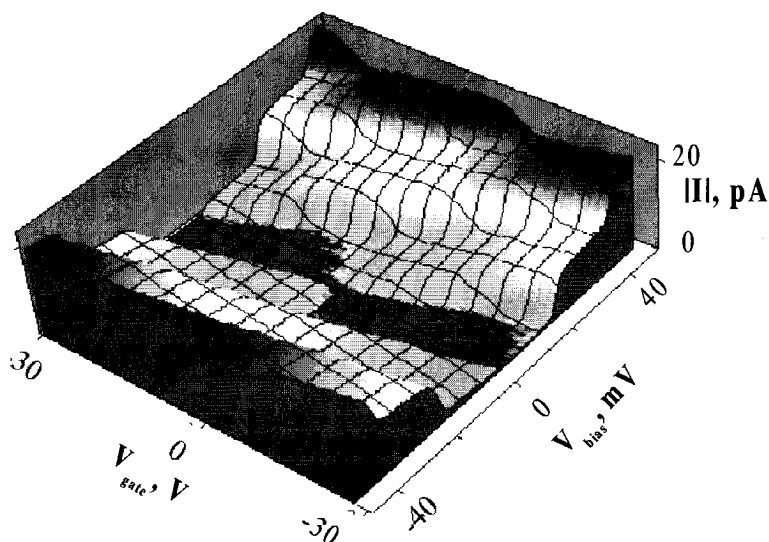
Figure 6: The greyscale plot shows a set of 51 spectroscopies taken for different gate voltages from -30 to + 30 volts. The value of dI/dV is represented with different shades of grey. Such a figure is called the stability diagram of a single-electron transistor. The dark area at the centre of the image corresponds to the Coulomb blockade of transport: the current through the cluster is blocked because the electrons in the leads do not have enough energy to tunnel onto the cluster (their energy is lower than the charging energy of the cluster). Areas represented with different colours correspond to processes where one or more electrons can simultaneously tunnel through. Using the orthodox theory of single electron tunnelling we have fitted the values for the capacitances and resistances of the tunnel barriers and for the gate capacitance $C_1 = 8 \cdot 10^{-18}$ F, $C_2 = 1 \cdot 10^{-18}$ F, $C_g = 5 \cdot 10^{-21}$ F, $R_1 = 2$ GΩ, $R_2 = 50$ MΩ, where C_1 and R_1 refer to the tip-cluster barrier, C_2 and R_2 refer to the cluster-substrate barrier and C_g is the gate-cluster capacitance

A full set of measurements taken at 4.2 K is shown as a 3D greyscale map in Fig. 6. Such a graph is called the stability diagram of a single-electron transistor. The dark area at the centre of the graph corresponds to the Coulomb blockade of transport: the current through the cluster is blocked because the electrons in the leads do not have enough energy to tunnel into the cluster (their energy is lower than the charging energy of the cluster). Areas represented with different shades of grey (and heights) correspond to processes where one or more electrons can tunnel simultaneously through. The discrete electronic spectrum of the cluster could not be resolved, as expected, since the mean electron-level separation for a 20-nm cluster can be

estimated to be less than 1 K. Using the orthodox theory of single electronics (see chapter 2) the barrier capacitances and resistances were estimated from the data are: $C_1 = 8 \cdot 10^{-18}$ F, $C_2 = 1 \cdot 10^{-18}$ F, $C_g = 5 \cdot 10^{-21}$ F, $R_1 = 2$ GΩ, $R_2 = 50$ MΩ, where C_1 and R_1 refer to the tip-cluster barrier, C_2 and R_2 refer to the cluster-substrate barrier and C_g is the gate-cluster capacitance.

Improving the gate-to-sample capacitance

In the previous paragraph we have presented the measurement of the sample-to-gate capacitance C_g for an experiment with 20-nm gold clusters. The value we have found is rather small ($C_g = 5 \cdot 10^{-21}$ F), which means that a high voltage is needed to obtain a measurable effect from the gate and, more importantly, that the gate would probably not have measurable effects on smaller clusters. Nevertheless, the simulations reported in chapter 6 show that the magnitude of C_g depends critically on the layout of the sample (C_g is strongly reduced by the presence of neighbouring particles), and also on the orientation of the tip with respect to the sample. Therefore, we can expect that different samples and/or tips with 'different geometries' may present substantially different C_g couplings. Indeed, we have found a sample with C_g up to 100 times bigger than in the measurements described in the previous paragraph. Figure 7(left) shows the measured I-V_g graph for constant bias voltage. Current oscillations with a period of about 250 mV can be clearly seen. The I-V characteristic (shown in Fig. 7) presents Coulomb blockade steps of about 20 meV.

The spectroscopic measurements of Fig. 7 can be consistently interpreted as the effect of Coulomb charging on a nanometer-sized metallic particle, much like the measurements described in the previous paragraph. There is, although, one important difference between the two experiments. In the case of Fig. 7 the particle was generated in a rather irreproducible way: while the S-gate was being scanned over the surface of $NbSe_2$, the tip crashed into an asperity of the surface and a piece of it broke off (we observed a jump in the STM z-dial readout). After the crash the I-V spectroscopy showed the Coulomb blockade characteristic reported in Fig. 7.

The I-V characteristic showed again a linear behaviour following the shortening of the metallic tip by the application of a voltage pulse. The sudden and uncontrolled appearance of Coulomb blockade steps in the I-Vs (mainly after a crash) had been

previously observed by us and other groups for different STM experiments. This phenomenon is generally interpreted as caused by one or more particles, loosely attached at the apex of the STM tip following the crash. The chemical composition of the particle cannot be clearly understood from the measurements, but from the above discussion we believe that it is made of Pt coming from the broken tip. Another possibility is that the particle is a grain of $NbSe_2$ from the substrate.
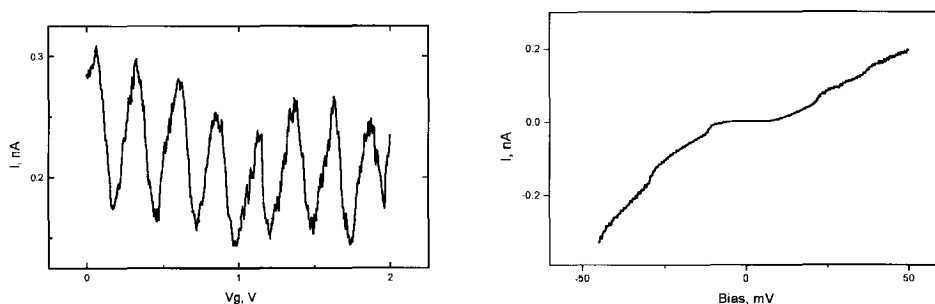
Figure 7: (left) I vs. V_g with fixed bias V_b = 50 mV for a particle generated by a tip crash, T = 200 mK (the measurement was taken in a dilution refrigerator). (right) the corresponding I-V for V_g = 0.

References

Part of this chapter was published in Appl. Phys. Lett. **76**, 384 (2000).

[1] See for example the seminal paper: L. Esaki and R. Tsu IBM J. of Res. And Dev. **14**, 61 (1970).

[2] For a review of transport in semiconductor quantum dots: L. P. Kouwenhoven et al. *Mesoscopic electron transport*, pp 105-215, Kluwer Academic Publisher (1997).

[3] D.V. Averin et al. *Mesoscopic phenomena in Solids*, edited by B.L. Altshuler et al. (Elsevier, Amsterdam, 1991), p 169.

[4] SPM control electronics 'TOPS III', Oxford instruments, Cambridge (1999).

Chapter 5

Fabrication of the Scanning Gate Probes

L. Canali, L. Gurevich and L. P. Kouwenhoven

Abstract:

In this chapter we explain and discuss the fabrication recipe for a new device called the Scanning Gate Probe (S-gate). The S-gate consists of two thin and sharp metal electrodes fabricated close to each other on the opposite sides of a silicon nitride cantilever. The device can be used as a tip for scanning tunnelling microscopy with the extra feature of a gate electrode to alter the transport characteristic of the sample much like the gate in a transistor. The application of S-gates to the study of metallic nanoclusters is discussed in chapter 4.

Fabrication recipe

We microfabricate the scanning gate probes using a multistep process involving e-beam and optical lithography. We start with a Si (100) wafer covered on both sides with a multilayer of SiN_x-SiO_2-SiN_x, 100 nm per layer, deposited by low-pressure
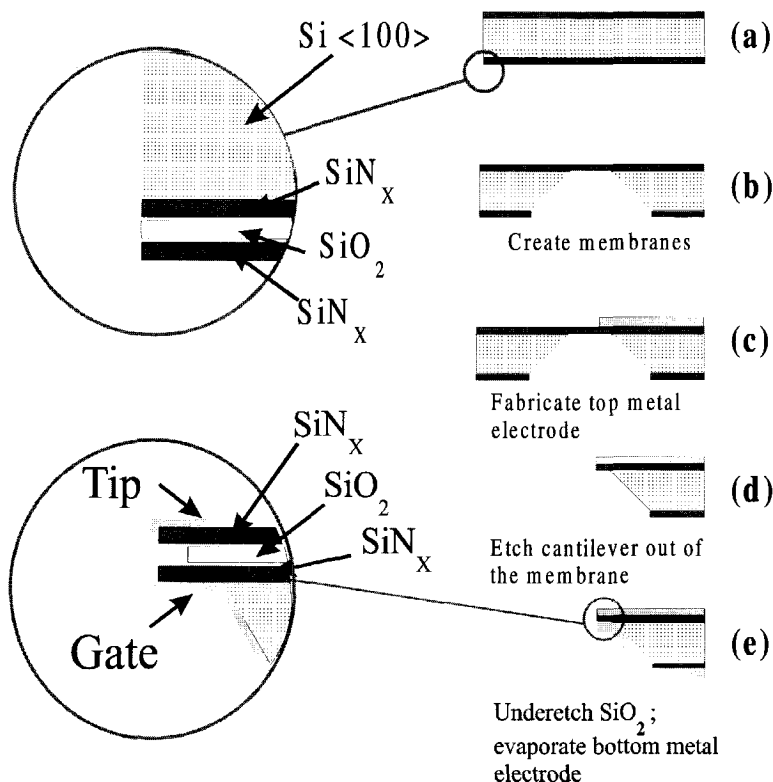
Figure 1: Fabrication recipe for the scanning gate probes. (a) We start with a Si (100) wafer covered on both sides with a multilayer of SiN_x-SiO_2-SiN_x, 100 nm per layer, deposited by low-pressure chemical vapour deposition (top inset). (b) We pattern the backside of the wafer by optical lithography and then we etch through the multilayer by reactive ion etching using CHF_3. Afterwards we etch the silicon wafer through its entire thickness in a 30%-KOH aqueous solution with addition of isopropanol at 80° C. (c) Next we fabricate the Pt tip electrode by e-beam lithography, evaporation and lift-off. The tip is aligned to the sharp end of the silicon chip. (d) An Al-mask is fabricated on top of the membrane and aligned to the tip electrode yet by means of e-beam lithography, evaporation and lift-off. We use the mask to protect the tip while we etch through the multilayer by anisotropic plasma etching with CHF_3 and form a sharp, freestanding cantilever. (e). We underetch the oxide part of the SiN_x-SiO_2-SiN_x multilayer by dipping the wafer in BHF solution to prevent unwanted electrical contacts between the final top and bottom electrodes (lower inset). Last we evaporate the platinum gate electrode on the backside of the chip.

chemical vapour deposition (see inset to Fig. 1a). The thickness of the multilayer ultimately determines the tip-gate separation and thus the main 'quality parameter' of the S-gate device: the gate-to-sample capacitance.

In the first fabrication step, we pattern the backside of the wafer by optical lithography and then we etch through the multilayer by reactive-ion etching using CHF_3. Afterwards we etch the silicon wafer through its entire thickness in a 30%-KOH aqueous solution with addition of isopropanol at 80 ^0C. The solution does not etch the SiN_x-SiO_2-SiN_x multilayer, so that a thin membrane is formed on the topside of the wafer (Fig. 1b). Next we fabricate the top electrode by e-beam lithography, evaporation of Pt and lift-off. The electrode is aligned to the sharp end of the silicon chip (Fig. 1c). We fabricate the top electrode as a submicron wire, instead of simply evaporating a Pt film over the entire surface, because the latter method has shown to produce mainly S-gates with short-circuits between the top and bottom electrodes. Thereafter we fabricate an Al-mask aligned to the top electrode on the silicon nitride membrane. The mask is fabricated with the same techniques as the top electrode, i.e. e-beam lithography, evaporation and lift-off. We use the mask to protect

Figure 2: SEM image of a Scanning Sage Probe (S-gate). The probe consists of two thin and sharp Pt electrodes nanofabricated on a silicon nitride cantilever. One electrode is used to acquire STM topography and spectroscopy (tip), while the other can be used to change the transport characteristic (gate).
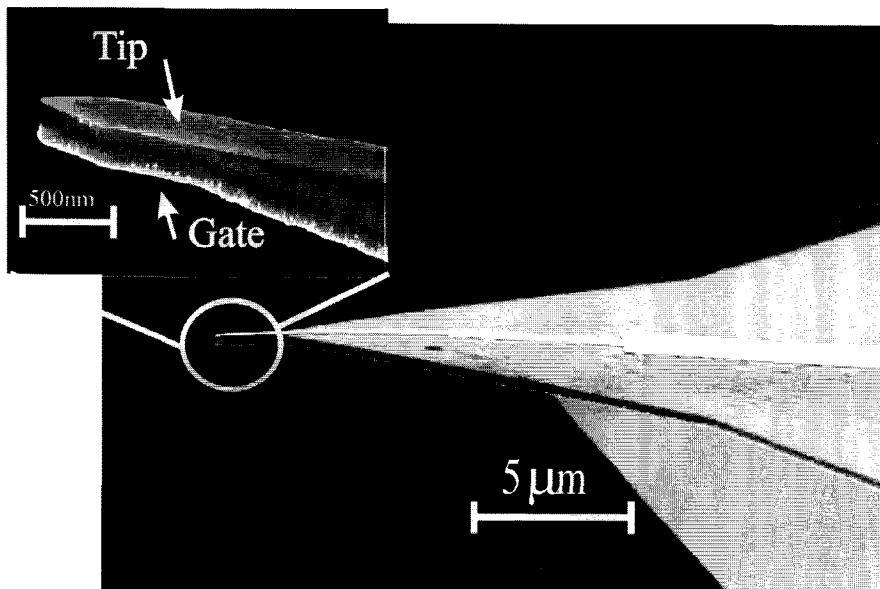
the tip while etching through the multilayer by anisotropic plasma etching with CHF_3 and form a sharp, freestanding cantilever (Fig. 1d). Afterwards we underetch the oxide part of the SiN_x-SiO_2-SiN_x multilayer by dipping the wafer into a buffered HF solution. This is done to prevent unwanted electrical contacts between the top and bottom electrodes (inset to Fig. 1e). Last, we evaporate the platinum electrode on the backside of the chip (Fig. 1e).

After fabrication the scanning gate probes can be mechanically detached from the wafer. At present, the S-gates are fabricated in batches of 8 at a time with a yield of about 70%. The probes consist of two closely separated metal electrodes (with a distance of about 200 nm) extending onto the sharp ends of a silicon nitride cantilever (see also Fig. 2). The whole chip has a size similar to commercial AFM tips ($\sim 2 \times 4 \times 0.5$ mm^3). They are easy to handle and can be installed on many existing STM heads by using an ad-hoc tip-holder (see also the last paragraph of this chapter).

Characterization of the S-gate tips

After fabrication the S-gate tips are inspected with a scanning electron microscope (SEM). In particular we image the apex of the tip to ascertain their actual shape and discard the devices that have fabrication faults. As mentioned in the previous paragraph, we are currently using a relatively long fabrication process were all the steps have to be successful to obtain a working probe. A good S-gate device will have the tip-end composed of two flat electrodes, sharp at the very end and (electrically) separated, i.e. the image of a good cantilever should be similar to Fig. 2. Figure 3 shows some of the typical fabrication faults that can be imaged with the use of a SEM: (a) the etching of one of the electrodes was not uniform: large grains (probably of Si) are visible on it. Such an electrode would make a very blunt tip and thus considerably reduce the STM resolution. It is anyhow still possible to use the second electrode as tip and the blunt one as a gate. (b) The top electrode is much longer than the lower one, while it could still be used as an STM tip, it would substantially screen the gate action of the second electrode (see also the calculations reported in chapter 6). (c) There is a short circuit between the two electrodes. The device can be used to perform STM, but no gate effect would be possible. (d) Major alignment problems between the two electrodes make the device most probably useless.

Electrical characterization

It is often agreed that the imaging of the atomic lattice of highly oriented pyrolithic graphite (HOPG) is a reliable quality test for STM set-ups (intended as including the scan head, electronics and vibration damping system). Fig. 4 shows an STM topography obtained with a S-gate at 4.2 K on HOPG. A periodic structure is clearly visible, representing the lattice of C-atoms at the surface (a conclusion that we draw by comparing that image with analogous topographies obtained with higher resolution

(a)   (b)

(c)   (d)
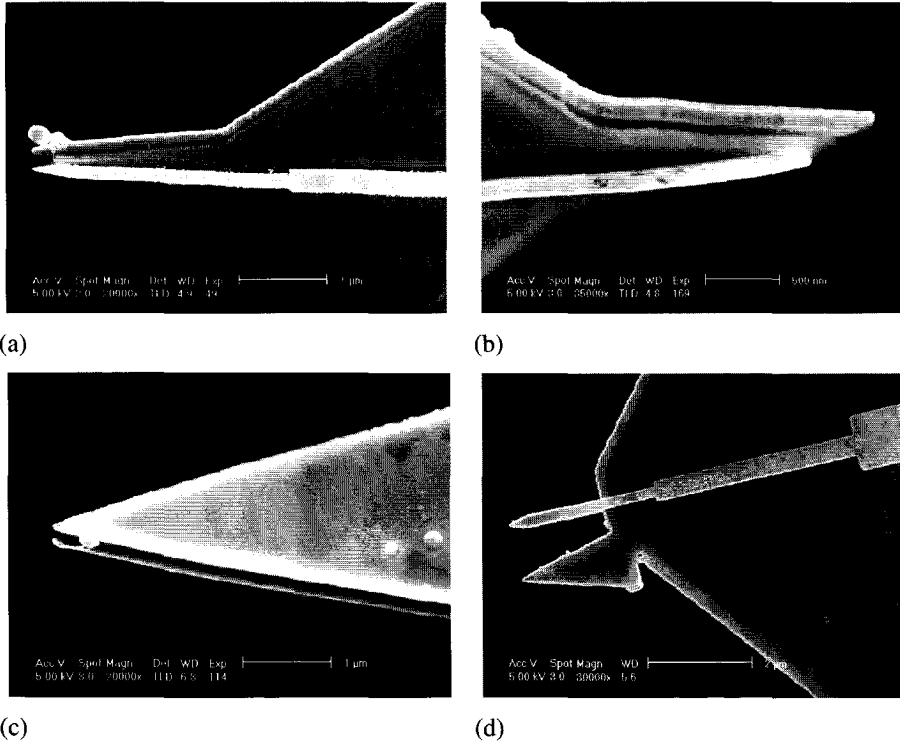
Figure 3:The fabrication of S-gates is a complicated process involving optical and e-beam lithography. All the steps in the fabrication have to be correct in order to yield a working probe. SEM inspection is necessary to identify and select the probes that can be used for a gate STM experiment. A showcase of typical problems is represented by these four SEM micrographs: (a) the evaporation of one of the electrodes was not uniform; (b) the top electrode is much longer than the lower one; (c) there is a short circuit between the two electrodes; (d) Major alignment problems between the two electrodes
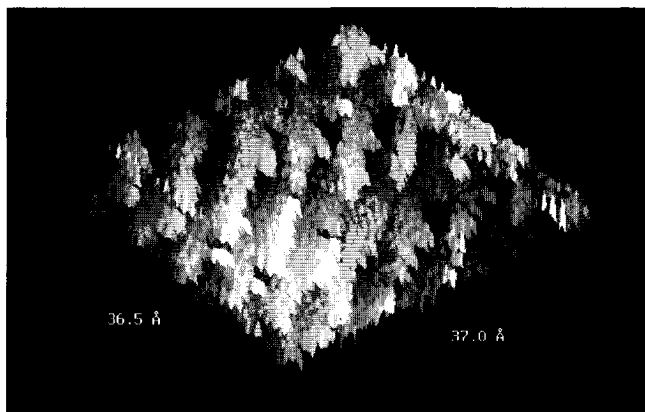
Figure 4: STM topography on the freshly cleaved surface of graphite (HOPG) obtained at 4.2 K with a S-gate. Atomic features are resolved, which proves that the S-gate microscope can achieve subnanometer resolution. The topography shown here has been rotated to face the direction of a C-lattice plane. No smoothing has been performed on the image in order to give the reader a quantitative idea of the resolution obtained by the probe.

using standard STM tips). The resolution of the S-gates depends critically on the shape of the last atoms of the tip (see also the discussion of chapter 6), that cannot be controlled with our current fabrication process and also cannot be easily investigated by SEM imaging. Moreover the shape of the tip can change during scanning, for example when a piece of the tip is detached by colliding with an asperity on the sample which could not be compensated by the STM feedback loop. From the S-gate topography of Fig. 4 and also the many topographies acquired while studying metallic clusters with the S-gate probes (see also chapter 4), we estimate a value for the 'average resolution' of S-gates between 0.1 and 5 nm. A recipe to produce sharper tips or to sharpen the existing ones would greatly benefit, among others, the study of molecules and small metallic clusters.

S-gate tip holder

A special tip holder has been made to mount the S-gate tips on our low temperature STMs (see Fig. 5). As it is shown by the simulations discussed in chapter 6, it is important that the gate and tip electrodes are both perpendicular to the sample to maximise the gate-sample capacitance. Nevertheless, practical reasons suggest

mounting the tip with a small angle to the sample, so that the tip electrode will be closer to the sample than the gate electrode, even if the former is slightly shorter than the latter. Besides, a small tilt (30^0) makes the optical alignment of the tip easier. The alignment of the S-gate tip is usually done by watching the reflection of the tip on the substrate under a microscope: we bring the two images, the real one and its reflection, very close to each other using the coarse approach motion of the STM.

The tip holder has to contact two wires independently, the tip and the gate. Moreover, the S-gate has to be easily mountable and removable from the holder. A photograph of the tip holder is shown in Fig. 5: A S-gate chip is glued on it with conducting (silver) epoxy glue, which makes contact to two separate wires carrying the tip and gate 'signal'. The S-gate holder is designed to be mounted on our STM set-up able to reach millikelvin temperatures (described in chapter 1). Note that, in our design, the sample is mounted on the STM plunger, whereas the S-gate is fixed below it.
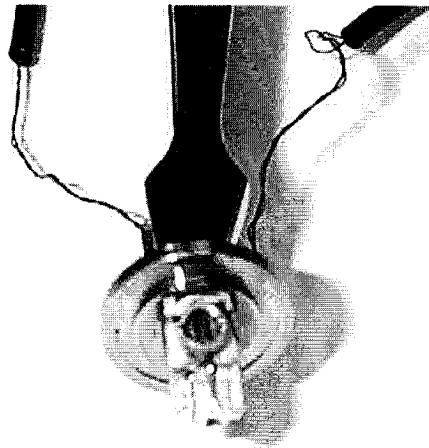
Figure 5: Picture of a S-gate probe mounted on its custom holder. The probe is glued with conducting silver epoxy to a Teflon rigid support. Two thin copper wires are glued to the opposite sides of the chip to provide electrical connection to the tip gate electrodes.

Chapter 6

Modelling the Scanning Probes by Capacitance Calculations

L. Canali, P. Basten and L. P. Kouwenhoven

Abstract:

In this chapter we address the issue of modelling the functioning of our nanofabricated scanning gate probes (S-gates). We have developed a computer model to simulate the scanning of a S-gate probe over a sample taking into consideration a set of experimental layouts of particular interest for the investigation of nanoclusters. The results of the calculations give useful directions on how to improve the preparation both of the probes and the samples. Similar calculations have been performed for our design of a scanning single electron transistor. From the computer model we are able to correlate the resolution of our scanning devices with the geometry of their tip electrodes.

Modelling of the S-gate probes

Scanning gates (S-gates) are scanning probes made of two sharp metallic electrodes, to be used as tip and gate for STM-like experiments. They are fabricated by means of nanolithography, as explained in chapter 5. The main parameter defining the quality of the scanning gate probes is the gate-to-sample capacitance C_g. The higher C_g, the more effect the gate has on the transport properties of the system. It is therefore beneficial for the experiments to be able to calculate C_g and to understand which factors of the sample and device design influence it most. Taking into account the experimental results of chapter 4, we choose, as model system, a S-gate positioned over a metallic particle deposited onto a metallic surface (see also Fig. 1). The modelling allows us to calculate C_g as a function of different experimental parameters. We interpret the results of the simulations by considering C_g small when a large voltage is needed to induce one extra electron charge on the particle (for instance when C_g x 1V << e, considering 1V as a typical value for the gate voltage). In particular, we are able to calculate C_g in the case of an isolated particle under the tip and to understand why measuring on a monolayer of particles can be particularly difficult with the S-gates.

General description of the calculations

We have modelled the S-gate experiment as an electrostatic problem with four conductors: the tip, the gate, the substrate and the particles. Each simulation run generates an output consisting in a 4x4 capacitance matrix **C**, which solves the electrostatic problem in terms of self- and mutual- capacitances of the conductors. We are mainly interested in the capacitive coupling between the gate electrode and the particles. Such value is contained in the matrix **C**.

The capacitance matrix is calculated using a package called FASTCAP [1], which implements a particularly fast algorithm to solve complex electrostatic problems. We have described the geometry of our problem to the program by dividing the conducting surfaces in a fine mesh of small conducting panels connected together. The program calculates the appropriate charge distribution and arranges the boundary conditions in a self-consistent way. A discussion on how to implement a FASTCAP
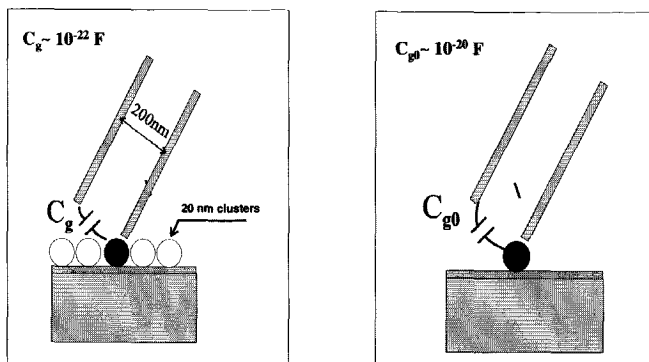
Figure 1: Model geometry for the numerical calculation of the gate-to-cluster capacitance C_g in a S-gate experiment. The S-gate is modelled as 2 metallic parallelepipeds separated by 200 nm, we assume $\varepsilon_r = 1$ for simplicity. One parallelepiped models the tip and is positioned ~ 1 nm above the clusters, the other models the gate electrode. Calculations give C_g of the order of 10^{-20} F, for the case of an individual cluster. When the sample is covered by a monolayer of clusters, however, this value is reduced by two orders of magnitude. It is thus very important to prepare samples with isolated clusters.

simulation is postponed to the appendix of this chapter. In our calculations the tip and gate electrodes are modelled as rectangular parallelepipeds with dimensions 30 x 30 x 500 nm^3. The two electrodes are parallel to each other and separated by a vacuum barrier of 200 nm. They are positioned above the 'sample' with a small tilt of 30^0 (from the normal). The model S-gate can then be moved over the sample in the 3 spatial dimensions to calculate $C(x,y,z)$ maps for different sample configurations.

Results of the simulations

We use FASTCAP to model the experiments described in chapter 4, by calculating the capacitive coupling of the gate electrode to a metallic particle just below the tip. As shown in Fig. 1, one of the electrodes (the tip) is positioned above a metallic particle of a few tens of nanometers in size (in the actual model the particles are approximated to a cubic shape). A dielectric barrier separates the particles from the metallic substrates. Such a model is in many ways approximate and can only be used to calculate the order of magnitude of the gate-to-cluster capacitance C_g or, rather, the relative change of C_g for different sample layouts. That is because the exact shape and arrangement of the electrodes and of the metallic particles cannot be known precisely

and is different for each combination of S-gate and cluster samples (as discussed in chapter 5). Moreover the tip shape (and length with respect to the gate) can vary throughout an experiment, e.g. during scanning or because of a voltage pulse applied to the tip (as in the experiment discussed at the end of chapter 4).

The first and most important problem we address with the simulations is to estimate the feasibility of the S-gate experiments, i.e. whether a microfabricated probe has sufficiently high capacitive coupling to a sample to be able to do interesting mesoscopic experiments. As shown for the model geometry of Fig. 1, we find typical values $C_g \sim 10^{-20}$ F, which are very small but still comparable, for example, with those of the experiments discussed in chapter 2. Another important problem, which we first faced during the testing of the first S-gate sensors, is to understand whether the preparation of samples with isolated particles is really important to improve their coupling to the gate. The intuitive idea about it, is that the presence of neighbouring particles (as for example in a monolayer of particles on the surface) may disperse the electric field-lines coming from the gate, toward a large number of particles, each attracting their own 'share' of field lines. Simulations with FASTCAP show that that is indeed the case and that C_g can be drastically reduced by the presence of nearby particles (see also Fig. 1). For this reason we have developed recipes to prepare samples with isolated particles, which are discussed in chapter 7.

Modelling of the S-SET

The scanning single electron transistor (S-SET) is a sensor-probe consisting of a single electron transistor (SET) microfabricated on top of a scanning probe tip. In chapter 3 we describe the functioning of the S-SET of Yoo et al. [2] and our design of S-SET on a silicon nitride cantilever. The latter was said to have potentially better spatial and charge resolution. In this paragraph we want to investigate further that conjecture by means of computer modelling, while we refer to chapter 3 for a description of the S-SET geometry. For the purposes of this discussion we consider the SET simply as a device (or black box) able to measure charge with very high sensitivity. Namely, the SET measures the charge on its island-electrode nanofabricated at the end of the tip. The charge on the island-electrode is proportional
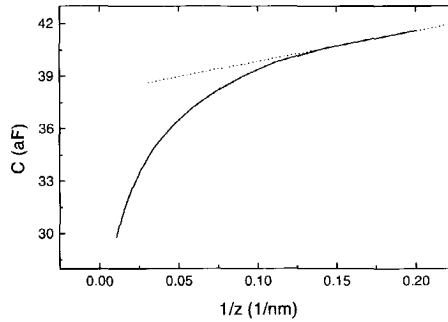
Figure 2: Calculation of the island-to-substrate capacitance of our model S-SET as function of 1/z. This simple calculation can be compared with the expected asymptotic limit C ∝ 1/z for z → 0, represented as a dotted line in figure. See also the appendix to this chapter for a discussion of how the calculations are performed and how these kind of electrostatic problems are mapped into FASTCAP

to the local electrostatic potential above the sample, because the electrode is scanned in close proximity of the sample surface and is capacitively coupled to it.

We have run a few numerical calculations with FASTCAP to model the sample-to-island-electrode capacitance for different configurations. The calculations allow us to draw some conclusions on the resolution of the S-SET. The T-shaped S-SET island is modelled into FASTCAP as a parallelepiped. This means that only the 'leg' of the T is taken into account, whereas the crossbar or 'cap' of the T is neglected. We also ran a simulation using a T-shaped island and observed no significant difference in the output, but a considerable increase in the calculation time. The parallelepiped representing the SET-island will be referred to as the tip. The tip has a rectangular cross section of 70 x 200 nm^2 and a length of 1 µm (calculations with longer tips do not produce significantly different results). The tip is positioned above a conducting plane of area 5 x 5 $µm^2$, forming an angle of 60^0 with it. The tip and sample are divided into small panels by FASTCAP to perform the numerical integration (the same considerations about the panelling of the S-gates hold here too).

Figure 2 reports the graph of tip-sample capacitance $C(z)$ as function of the tip-sample distance z, calculated by FASTCAP for a S-SET tip above a conducting plane. For distances to the sample smaller then the island dimensions a parallel plate picture predicts that the capacitance varies as $1/z$. At large z, the capacitance drops to zero, as expected. This behaviour is observed in the calculation reported in Fig. 2. The

calculated values for the tip-sample capacitance give us useful information on the magnitude of the signal we can expect from the S-SET. The calculated $C(z)$ can be used, for example, to set up the (coarse) approach for the S-SET by monitoring the SET current oscillations (as in Ref. 2). Let us say, for instance, that one decides to approach the S-SET at about 20 nm from the surface. From Fig. 2 we read $C(z=20nm)$ = 36 x 10^{-18} F, which gives an induced charge Q = CV $\sim 3e$ when the sample bias V = 10 mV. Which means that the coarse approach can be stopped when 3 oscillations on the SET current are detected, at that point the SET will be 20 nm from the conducting surface (within the approximations used to model the tip).

Another problem of great interest to understand the performance of the S-SET as a sensor device, is to estimate its spatial resolution. A simple but effective way to do that is to scan the S-SET at a height h over a conducting surface that has an insulating slit of width W in the middle. The mutual capacitance tip-surface vs. lateral displacement shows a dip in correspondence of the insulating slit. When such a dip is measurable by the S-SET, we can say that the resolution of the S-SET is W or better. Note that the resolution will also depend on h. We have chosen a similar approach to numerically estimate the resolution: we have modelled the experimental configuration with two conducting semiplanes separated by a slit of width W, with the S-SET

Figure 3: Calculated capacitance coupling between the S-SET and a sample with an insulating slit of width W = 100 nm as a function of the lateral displacement x and for different tip-sample distances h. The dip in the C(x) curve is a measure of the slit by the S-SET. The graph shows that it is progressively more difficult to resolve the slit as h increases.

scanning across at an height h. Using FASTCAP we have calculated a series of $C(x)$ graphs for different W and h. The results of the calculations are shown in Fig. 3 for

distances h = 25, 40 and 70 nm. As expected the tip-sample capacitance is smaller at larger distances, and variations in the capacitance ΔC while moving over the slit are less pronounced. Scanning over a slit with aperture 100 nm at a height of 25 nm results in a ΔC of about 1.8 aF (the 'depth' of the feature), which corresponds to a relative drop of about 4.5 %. The width of the capacitance-drop at half the maximum value (FWHM) is approximately 100 nm. Figure 4 shows a group of $C(x)$ curves with constant h and variable W. The dip in the capacitance can be seen to decrease substantially for decreasing W and becomes smaller than 1 % when $W \sim h$.

To derive an estimate of the S-SET resolution from the $C(x)$ calculations, we first have to understand the charge sensitivity of the device, i.e. estimate the smallest capacitance variation that the SET sensor can measure. For that reason we have microfabricated an SET test sample (with junctions parameters similar to the S-SET design) and measured its I-V-V_g characteristics and noise levels at 350 mK [3]. From the measurements we could estimate a sensitivity of about $3{\cdot}10^{-4}$ $e{\cdot}\text{Hz}^{-1/2}$, e.g. the device can detect a single electron at a distance $\sim$1 mm when used with an integration time of 1 sec. Another way of saying it, is that with a sample bias of 100 mV (typical value for mesoscopic experiments) and an integration time of 1 sec, the SET can measure down to $\Delta C \sim 5{\cdot}10^{-22}$ F. This value for ΔC is very small and definitely represents the most optimistic estimate for the resolution. Other factors have to be taken into account as possible source of noise that can deteriorate the resolution, such as: acoustical (vibrational) noise, cross-capacitances with the environment (the SET is surrounded by metal) and (electronic) drift of the Coulomb peaks. Considering all those factors we estimate the sensitivity at about 1% of the measured signal.

Looking at the calculations reported in Fig. 4, this means that in order to resolve a slit of aperture W, the height h of the SET-island above the sample should be of the same order of magnitude: $h \sim W$. Note that the spatial resolution is a function not only of the amplitude of ΔC, i.e. the depth of the feature, but also of the width of it. Smaller tips are less sensitive to capacitance changes, but can provide a higher resolution.

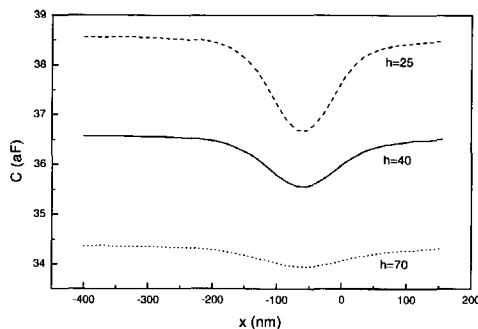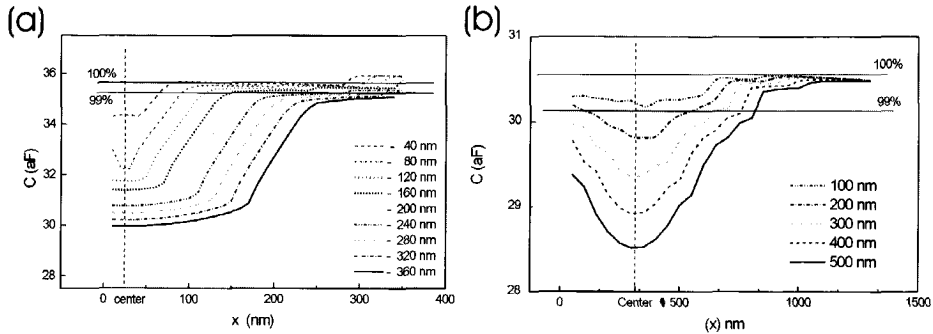*Figure 4: Calculated capacitance coupling between the S-SET and a sample with an insulating slit of width W nm as a function of the lateral displacement x and for different tip-sample distances h. The dip in the C(x) curve is a measure of the slit by the S-SET. (a) h = 25 nm and W is varied between 40 to 360 nm, The drop in capacitance near the centre of the slit is roughly constant for large W, which means that the S-SET resolution is better than W. (b) h = 100 nm and W varied between 100 and 500 nm.*

This means that the cross section of the end of the tip convolutes with the S-SET image diminishing the resolution. The width of the feature of 200 nm in the simulation corresponds to approximately twice the thickness of the tip (70nm).

As discussed previously for the scanning gate sensor, the highest capacitive coupling between the island and the sample is obtained when the S-SET is oriented perpendicularly to the sample. Note that practical reasons suggest mounting the tip with a small tilt in the actual experiments. We have run a capacitance calculation to understand whether a tilt of 30^0 would limit significantly the resolution of the S-SET. Fig. 5 shows the calculation of $C(x)$ over an insulating slit similar to the calculations that we have just discussed. The main feature to note is that the cross-capacitance between tip and sample is smaller in case of the tilted tip. This is to be expected because the centre of mass of the tip is farther away from the sample in the case of a tilted tip, which leads to a lower mutual capacitance. Because of the larger distance also the drop in the capacitance is smaller for a tilted tip.
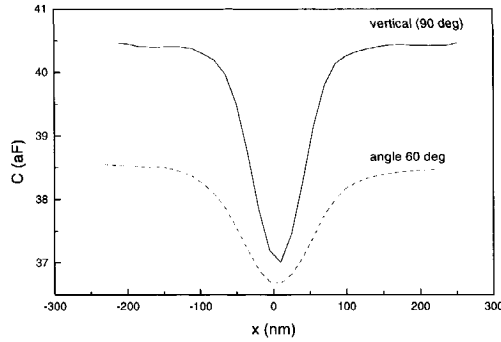
Figure 5: Calculation of the tip-to-sample capacitance C(x) for an S-SET position at a height h = 25 nm over an insulating slit of width W = 100 nm. The solid line is the calculated C(x) for a S-SET positioned vertically over the sample, while the dotted line corresponds to a tip making an angle of 60^0 with the sample.

Appendix: FASTCAP calculations

The calculation of the mutual capacitance between two conductors can be stated as a simple mathematical problem: the solution of the Poisson's differential equation

$$\nabla^2 \phi(\mathbf{r}) = -4\pi\rho(\mathbf{r}),$$

where $\rho(\mathbf{r})$ is the charge distribution and $\phi(\mathbf{r})$ is the electrostatic potential (in the CGS unit system). The boundary conditions of the differential equation are: (a) the electrostatic potential on the surface of each conductor is constant, (b) the integral of the $\rho(\mathbf{r})$ over the surface of each conductor gives its total charge. The solution of the problem is a difficult task which normally requires numerical solutions. Because of the linearity of Poisson's equation we can write a general relationship between the charge Q_i and voltage V_i of the conductors even without knowing the exact solution of the electrostatic problem:

$$\begin{pmatrix} Q_1 \\ Q_2 \\ \vdots \\ Q_i \end{pmatrix} = \begin{pmatrix} C_{1,1} & C_{1,2} & \cdots & C_{1,j} \\ C_{2,1} & \vdots & \vdots & \vdots \\ \vdots & \vdots & \vdots & \vdots \\ C_{i,1} & \cdots & \cdots & C_{i,j} \end{pmatrix} \bullet \begin{pmatrix} V_1 \\ V_2 \\ \vdots \\ V_j \end{pmatrix},$$

which can also be written in the more compact form $Q = C \cdot V$, where we can recognise the n-conductor generalisation of the usual definition of capacitance. For our purposes, the electrostatic problem translates into the computational problem of calculating the capacitance matrix. For example the total electrostatic energy can be calculated from C, as $\frac{1}{2}Q \cdot V = \frac{1}{2}V \cdot C \cdot V$. Since the energy has to be positive this also proves that C is a Hermitian matrix and that the diagonal elements $C_{i,i} > 0$. Conversely, the non-diagonal elements (called mutual capacitances) can be shown to be negative. The exact calculation of the capacitance matrix can be a very heavy computational job even for a simple geometry because of the non-uniform charge distribution near the sharp edges of the conductors. This kind of problem is well known and studied in the field of numerical methods applied to differential/integral equations. Without going into details, it is sufficient for our scopes to know that ad-hoc algorithms (called fast multipole algorithms) have been developed which rapidly calculate approximated capacitance matrices [4]. Such an algorithm is implemented in a shareware program called FASTCAP [1]. We have compiled and run FASTCAP under Linux on a PentiumII[TM] 450-Mhz PC to perform the calculations described in this chapter.

The first step to set up the model is to describe the objects (conductors) to the program. This is done via a script language that allows the description of simple geometrical forms such as cubes, parallelepipeds, planes, pyramids, etc and their
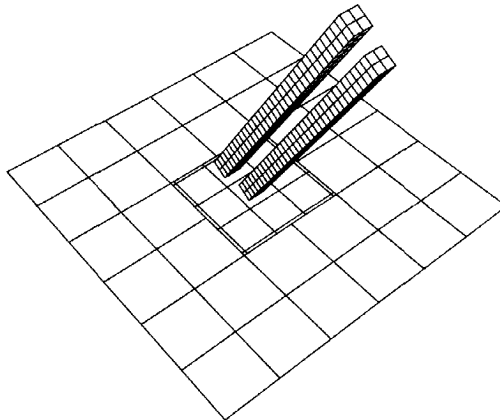
Figure 6: 3D image of the model S-gate used by our FASTCAP simulations. The amount of panelling and the size of the underlying 'substrate plane' used in the actual simulations are much larger than what is shown in the picture (simplified for reasons of clarity).

combination in the 3D simulation space. Each conductor surface is divided by the program into a fine mesh of small 'panels'. Each panel has a floating charge, which is self-consistently calculated. A finer mesh insures that the error introduced by the discrete numerical integration will have a smaller effect in the final result. Because simulations with objects that have many panels use a vast amount of memory (the memory occupation grows quadratically with the number of panels) and clock cycles, dense panelling should be used only in the areas where rapid change of potential is expected, such as near the edges of conductors and close to fine details of the objects. Since FASTCAP does not have an internal algorithm to specify the appropriate panelling density for a desired accuracy of the results, the approach taken was to manually increase the number of panels of the objects in the simulation till a reasonably good convergence (i.e. within 10% or better) in the output matrix C was observed.

References

[1] K. Nabors et al. *FastCap* (1992). Available from: http://rle-vlsi.mit.edu/~white.

[2] M. J. Yoo et al. Science **276**, 579 (1997).

[3] P. J. K. Basten *Afstudeerverslag*, TU Delft 1998.

[4] K. Nabors et al. SIAM Journal on scientific computing **15**, 713 (1994).

Chapter 7

Sample Preparation

L. Canali, L. Gurevich and L. P. Kouwenhoven

Abstract:

The fabrication and characterisation of the most important substrates for STM studies are discussed together with our recipes for the preparation of ultra-flat metallic films. We have developed and utilised different techniques to passivate noble-metal substrates with organic self-assembled monolayers and to deposit small metallic particles on them. The samples have been characterised by AFM and STM topography.

Sample preparation: an important factor for good STM imaging

Since the very first STM experiments of Binnig and Röhrer it has become clear that the STM can attain the highest resolution of any other microscope, providing that two important experimental parameters can be optimally controlled: the sharpness of the tip and the flatness of the sample. It is simple to prove, and also intuitive, that an atomically sharp tip will produce better lateral resolution than a blunt one. The flatness of the sample, however, proves to be an equally crucial factor for obtaining good topographic resolution. That is because the feedback loop has a finite response time: even in the case of an extremely sharp tip, the control electronics may not be able to maintain a constant current while scanning over sharp protrusions of the sample surface. As a result of that, the tip may experience a series of small crashes inside the scanning area. Other limiting factors for the resolution do not depend from the tip and sample preparation and are to be addressed at the stage of STM design (or set-up preparation). Among others, they include: electrical noise, thermal gradients and vibrational noise coupling into the STM (see also chapter 1). In this chapter we want to address the issue of optimisation of the sample preparation for STM and S-gate experiments.

General principles of the measurements on clusters

A typical STM experiment on clusters consists of two steps: (1) imaging of the sample by acquiring topographies in constant current mode, (2) positioning the tip over a single cluster to measure its spectroscopic characteristic.

A good topographic image, for this kind of experiments, means an image showing a flat and impurity-free substrate, over which the clusters can be detected with high contrast: i.e. appearing as small 'protruding hillocks' over a flat background. The concentration of clusters on the surface has to be high enough to show many of them in the scan area (typically 1 μm^2 at 4 K). At the same time the particles have to be isolated from one another, so that they can be measured individually. To improve our understanding of the sample preparation, we have run simulations of the gated STM experiments on clusters (see also chapter 6). We find that the capacitance between the tip and clusters can be reduced up to two orders of magnitude when the particles are

too close together. It is therefore very important to prepare samples with well-isolated particles.

Another key issue for a suitable sample preparation is that the clusters must be well fixed on the substrate, i.e. they should not be pushed around by the STM tip. To prevent this from happening we have to make sure that (a) the clusters have a strong bond to the substrate and/or the passivating monolayer, (b) that the STM tip is as far as possible from the surface, i.e. we want to use the highest possible tunnel resistance to acquire the topographies (in practice about 100 GΩ for our set-up).

Once an isolated cluster is found on the substrate by STM topography, the gated STM tip can be positioned over it to acquire the 3-terminal spectroscopic characteristic (I-V-V_g). This kind of measurement is generally done with the cluster electrically connected between the tip and the substrate via two tunnel barriers (see also chapter 4). One of the tunnel barriers is generally provided by a dielectric layer deposited on the substrate. A few important properties have to be met by such a layer: (a) it should be thin and homogeneous, (b) the I-V characteristics should have a large band gap (c) and it has to be able to bond the clusters. An alternative to the use of (mono)layers as tunnel barriers, is to have the clusters encapsulated in a dielectric shell. In that case, the shell has to be thick enough to provide good tunnel barriers for transport experiments and also able to bond to the metallic substrate.

From this discussion it is clear that the optimal sample preparation has to satisfy a series of stringent requirements, which can only be met by a few specific arrangements of substrate + monolayer + clusters. In the following paragraphs we describe some the solutions we have adopted to fulfill those requirements.

Substrates for STM

Highly oriented pyrolytic graphite (HOPG) is one of the most studied surfaces by STM, because it is relatively easy prepare and to image the lattice of carbon atoms at its surface. HOPG is a layered material, its surface is relatively inert to air and can be prepared simply by peeling off a thin layer from it. The result is a freshly cleaved surface likely to show terraces that are atomically flat over areas of about 100×100 nm^2. Moreover HOPG presents unusually large atomic corrugation, which makes the imaging of the surface atomic structure accessible for many STM set-ups (provided

that they have sufficient vibration damping mechanisms). For this reason the imaging of HOPG is largely used as the calibration test for (new) STM scan-heads (one such image, used as a test for the S-gate sensors, is shown in chapter 5). Unfortunately, we have not been able to develop an appropriate method to deposit metallic nanoparticles on the C-surface with a double tunnel-barrier configuration and, therefore, we cannot utilise HOPG as a substrate for our experiments on metallic clusters.

Mica is another layered material often used for STM/AFM experiments. Mica can be easily prepared to present large and atomically flat terraces. It is an insulator and therefore cannot be directly utilised for STM. However, when a thin film of noble metals (mainly Pt or Au) is deposited on its flat surface, mica can provide some of the flattest substrates for STM studies. Similar applications are found for the (insulating) surfaces of Si/SiO_x and quartz. All these substrates are available from commercial sources. Quartz and Si/SiO_x are normally shipped as thin wafers, preprocessed to present optically polished surfaces. Another good reason to use Si/SiO_x and quartz as substrates, is that they have a high melting point so that they can stand, almost unaltered, up to the very high temperatures required to evaporate and/or anneal metallic films.

Flat Au surface

A very important starting point for many STM experiments is the preparation of a flat and defect-free Au surface. Such a surface has been extensively used in our studies of metallic colloids, alone or in combination with different passivating monolayers.

We prepare most of our samples by evaporating a thin film of Au on the flat insulating surface of quartz: Fig. 1 shows an AFM topography of such a Au film. We can see that the sample presents flat terraces of about 20 nm in diameter next to more rough areas. The roughness measured on the terraces is ~1 nm peak-to-peak. Outside the terraces it is an order of magnitude larger. The fact that a vast portion of the sample has a considerable roughness is a problem for our STM experiments. This is because it becomes very difficult to image the colloids by STM topography, when the roughness of the substrate is of the same order of magnitude than their diameter. To solve this problem we have developed a technique to improve the flatness of the Au film by annealing it in a Bunsen-burner flame. We used a hydrogen flame to heat up
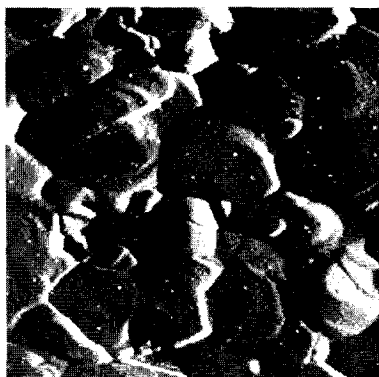
Figure 1: Non-contact AFM image 1×1 μm² of gold film prepared by evaporation. The surface has a granular structure. On top of each grain atomically flat areas of about ~20 nm in diameter can be found.

the film to about 1100 ^{0}C for roughly 30 to 60 seconds. Afterwards the sample was let to cool down in air. Figure 2 shows an AFM topography of a flame-annealed Au film. The improvement from a simply evaporated film (as in Fig. 1) is prominent. From the topographies we can conclude that H-flame annealing leads to the formation of large atomically flat grains oriented in the direction of lowest free energy (111) [1], separated by grooves ~20 nm in height.

After flame annealing, the samples were cut into small pieces that could fit our STM sample holder (approximately 3 × 3 mm² in size). The quartz substrates have to be relatively thin (~0.5 mm) to be cut easily. The grooves between the flat Au grains can hamper the formation of a homogeneous distribution of clusters, since the particles can easily be trapped at the grain-boundaries or can be pushed there by the scanning STM tip.

Another method to prepare flat Au surfaces consists in evaporating Au on the freshly cleaved surface of mica and then stripping off the Au film using tetrahydrofuran (C_4H_8O). The surface of Au that was in contact with mica will be exceptionally flat, as if it was stamped out of the cleaved surface of mica.
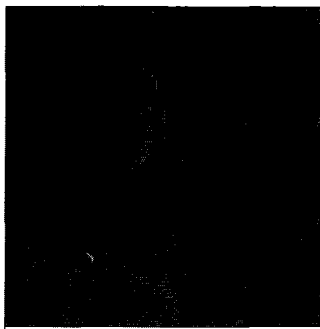
Figure 2: Non-contact AFM image 1×1 μm² of evaporated Au, flame annealed with H-flame. The flatness of the film is greatly improved compared to non-annealed Au.

Passivating monolayers

The study of single electronic effects on clusters requires the presence of a tunnel barrier between the particles and the underlying metallic substrate, otherwise no charging effects can be observed. A simple way to provide a tunnel barrier is by passivating the surface with a dielectric layer. Such a layer must be able to bond to the metal surface on one side and to the clusters on the other. Moreover it has to be so thin that the STM tip can simply hover above it while measuring the topography of the underlying metal. The layer has also to be homogeneous and possibly have a large gap for the electronic transport, so that it does not add any spurious features to the spectroscopy. All these properties can be met, for example, by self assembled monolayers (SAMs) of organic molecules. SAMs are spontaneously ordered arrangements of molecules on a surface. The ordering being the result of the interplay of many different chemical forces: among others there will be the attractive forces that bond the functionalised ends of the molecules to the substrate (e.g. the thiol group can bond to a gold substrate) and the van der Waals interactions between adjacent molecules in the layer (a force that is stronger for longer molecules). The chemical and physical properties of SAMs have been the subject of intense studies in the last decade and a large variety of recipes are available in literature to prepare SAMS with different chemical compositions [2]. A very interesting property of SAMS, for our purposes, is that their chemical specificity can be engineered by changing the freestanding end-groups of the molecules forming the monolayer. In the following

paragraphs we will describe the preparation of different (functionalised) monolayers that can bond to metallic substrates, on one side, and to clusters on the other. The quality of the monolayers and their ability to bond clusters have been tested at room temperature with a commercial STM/AFM [3] before mounting the samples in our low-temperature STM.

Platinum and cysteamine

The first sample that we have tested with a S-gate probe (see also chapter 4) consists of 20-nm gold particles deposited on a flat platinum film passivated with an organic monolayer. The Pt film is prepared by sputtering and presents peak-to-peak roughness of about 1 nm over approximately the entire scan area (~1 μm^2). The particles can be resolved by STM imaging, since their diameter is ~10 times bigger than the roughness of the substrate. A self-assembled monolayer is used to provide the tunnel barrier and fix the clusters by chemical bonds. To form the monolayer we dip the substrate (a Si/SiO$_x$ wafer covered with 50 nm of sputtered Pt) into a 0.1 mM solution of cysteamine in 1:1 mixture of ethanol and hexane for about 12 to 24 hours. The clusters are deposited from a charge stabilised aqueous solution, by letting one or more droplets of the solution evaporate on the Pt + cysteamine surface.

The cysteamine monolayer both bonds the clusters to the substrate and forms the tunnel barrier between the clusters and the Pt film. Figure 3 shows a scheme of the sample layout. The cysteamine molecule (NH_2-CH_2-CH_2-SH, also called 2-aminoethanthiol) is composed of a short hydrocarbon chain terminated at the two ends by N and S atoms. Therefore, there are two possible orientations of this molecule on the substrate: the first, as in Fig. 3, with the S-end attached to the Pt substrate, the second is with the N-end attached to the substrate. The latter orientation can be expected in presence of surface oxide [4], in that case a strong nitrogen-oxygen bond can be formed. Anyhow, it is not possible to discern with an STM topography between the two possible orientation of the cysteamine molecule.
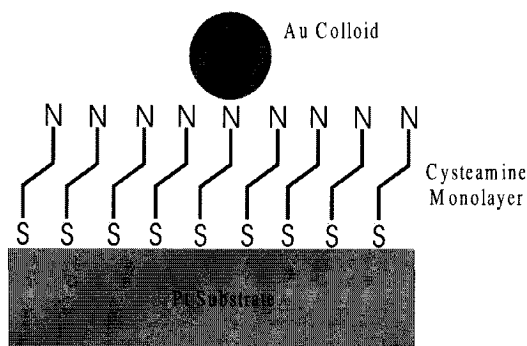
Figure 3: Preparation of a sample with gold colloids for a (gated) STM experiment. Clusters are deposited on a Pt film covered by an organic monolayer, which provides a tunnel barrier between the clusters and metal substrate. The monolayer is also responsible for binding the clusters and preventing them from moving over the substrate. To form the monolayer, we dipped the Si-SiO$_x$ wafer covered with a 20-50 nm Pt film into a 0.1mM solution of cysteamine in 1:1 mixture of ethanol and hexane for ~12÷24 hours. Cysteamine molecules are rather short (they contain only two carbon atoms) and have both thiol and amine end groups capable of attaching to metal surfaces.
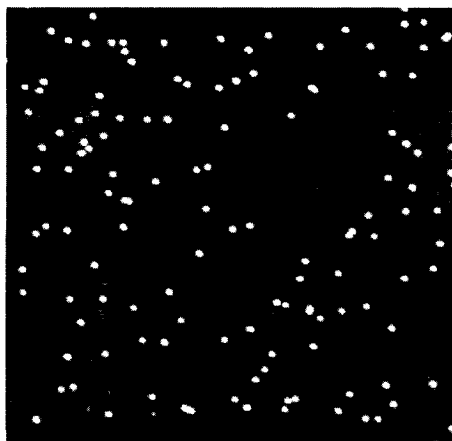
Figure 4: The figure shows a 3 × 3 μm^2 tapping-mode AFM image of a sample consisting of Pt-substrate + cysteamine monolayer + 20-nm Au clusters. The clusters are visible as bright spots, they are randomly spread out on the sample and appear isolated from one another.

After preparation, the sample is inspected with a commercial STM/AFM [3] at room temperature to check that: (a) the concentration of clusters on the surface, (b) that the particles are separated from each other and (c) that the clusters are well fixed on the surface during scanning and spectroscopic measurements. A tapping-mode AFM topography of the sample is shown in Fig. 4. Gold clusters appear as white dots in the image, separated from one another and with relatively high concentration. More details on the low-temperature STM measurements of this sample are reported in chapter 4. From those measurements we were able to estimate the colloid-sample resistance and prove that the cysteamine monolayer is thin enough for the STM tip to hover over it during the acquisition of topographies.

Alkanethiol and -dithiol monolayers

The study of small metallic clusters becomes increasingly interesting as the size of the particles decreases. From the physical point of view, small particles represent a good model system to study electronic confinement, i.e. the 'quantum box effect'. This effect can be seen when the diameter of the particle under study is of the same order of magnitude as the wavelength of the electrons inside it. In that case the electrons 'interfere with themselves' and their energetic spectrum changes from continuous to discrete. Many physical properties of the particles can be affected by the discretisation of the spectrum [5] (e.g. transport characteristic, luminescence, heat capacity, etc).

Figure 5: STM image 120x120 nm^2 of the 6-alkanethiol passivated gold surface. The patterns on the surface are due to the reconstruction of the Au surface induced by the SAM.

Many of these effects have presently been demonstrated only at low temperatures. If the particles are small enough, however, it is possible to observe the effects of the discretisation of the spectrum even at room temperature (more details about the physics of size quantisation are discussed in chapter 2).

We have discussed in the previous paragraph a recipe to deposit colloids on the surface of platinum. It was not possible to use such method to prepare samples with smaller particles (~5 nm) because the roughness of the sputtered Pt film did not allow good imaging. Therefore we decided to use substrates of Au, which can be prepared as very flat films (as discussed earlier on in this chapter). We have then developed suitable techniques to passivate the Au films with a dielectric layer and subsequently deposit clusters on them. The passivating layer needed to: (a) have at least one sulphur end-group that can bond to the gold surface, (b) be able to form a SAM on the surface. A (chemically) simple family of such molecules are the n-alkanethiols: they are constituted by a short chain of carbon atoms, saturated by H-bonds; and have one S-atom at the end of the carbon chain (see Fig. 6). N-alkanethiols have variable lengths depending on the number of carbon atoms in the chain (indicated by n). The sulphur atom will always attach to the Au surface, independently of n.

However, it has been proven experimentally [6] that short molecules (n < 6) do not form an ordered monolayer. That can be explained considering that their short alkane chains do not generate enough van der Waals attraction between molecules to arrange them in an ordered layer. When n ≥ 6, on the other hand, n-alkanethiols can spontaneously form a SAM on the surface of noble metals. Moreover, Kergueris et al. [7] have calculated the gap for electronic conduction and found a very large value of
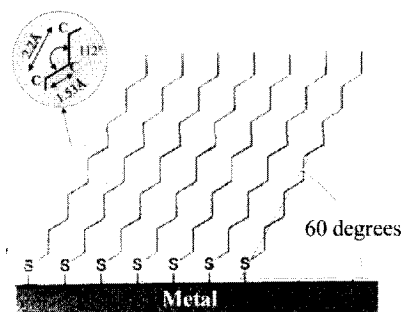

Figure 6: Scheme showing the formation of n-alkanethiols SAM. The molecules bond to the gold surface with the S-terminated end forming an angle of 60⁰.

the order of 10 eV. Figure 6 shows the scheme of the spatial arrangement of the thiol-Au bond: the molecules are arranged parallel to each other and with an angle of 60^0 to the surface.

The preparation of the thiol samples starts with the cleansing of the substrates with ethanol and/or oxygen plasma. The cleaned substrates are then immersed in a ~1 mM ethanolic solution of alkanethiols for 12 to 24 hours. To prevent oxidation, all solutions are prepared and stored in the N_2 glove box. Moreover, the ethanol is saturated in N_2 atmosphere in advance. After deposition the samples are rinsed a few times in pure methanol and ethanol and blown dry with N_2. The samples are stored in vacuum or N_2 glove box before use. From the literature and our own experience, we know that the organic SAMs degrade quickly in air on the timescale of a few hours. This is most probably due to reactions with O_2 and/or, as some authors suggested [8], with O_3 present in air. The thiol layer produces a smooth and flat passivating layer. The SAM removes the herringbone reconstruction of the Au (111) surface [9] and generates a new arrangement of the surface gold atoms in the form of irregularly shaped islands. Moreover, the monolayer increases the mobility of Au atoms on the surface and the new reconstruction can be seen to change in time.

The outward end of the thiol molecules can be functionalised to create a chemically specific surface, e.g. to bond metallic particles. For example, if a second sulphur atom is attached at the end of the alkyl chain of the thiol molecules the resulting monolayer would show a very high affinity for binding noble metals, e.g. gold clusters. For this reason we have experimented with a class of compounds called n-alkanedithiols, which have a chemical structure very similar to n-alkanethiols but with sulphur atoms at both ends of the alkane chain. Unfortunately these molecules do not form an ordered SAM, instead, both S atoms have a high affinity to bond to the gold substrate and form an irregular coverage of the metallic surface.

We have prepared a few samples passivated with 6-alkanedithiols, which should have a relatively large concentration of free thiol groups according to Ref. 10, but we found that layer is not uniform both for topography and spectroscopy; besides the Au clusters do not adhere well to such a layer. We have then tried to go round the problem of forming a SAM with dithiols, by using the 'insertion method' (analogously to the work of Ref. 11), which consists of: (a) preparing a SAM of thiols
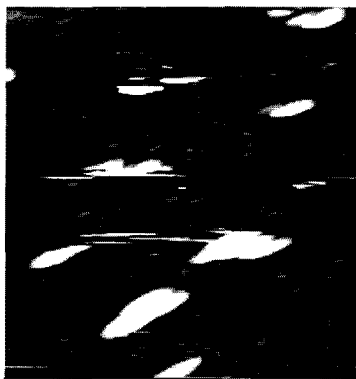
Figure 7: STM image 100x100 nm² showing 20-nm Au clusters deposited on a sample passivated with alkanethiols-dithiols. The clusters are not well fixed on the surfed. The STM tip drags them along the scan direction, eventually pushing them outside the scan area.

on the gold surface, then (b) adding dithiols in between the thiol molecules or, possibly, substituting them in the monolayer so that they stand up on the substrate.

The preparation of the dithiol samples require an extra step starting from the previously described recipe for thiol SAM: the sample with a thiol monolayer is immersed in a ~1 mM ethanolic solution of alkanedithiol for 12 to 24 hours. Some of the thiol molecules in the SAM will be exchanged for dithiols, which will, in this case, stand upright with one of their thiol end pointing outwards. After the preparation of the functionalised monolayer we can deposit metallic colloids on the surface. The main experimental problem we face with this kind of sample preparation is that the clusters are weakly bound to the substrate and thus can move by effect of the interactions with the STM tip. Figure 7 shows an STM image of a thiol+dithiol sample with 20-nm clusters deposited on top. A few features in the STM topography indicate that the tip is pushing the clusters around the substrate: (a) many clusters (the white dots in the image) appear stretched in one direction (toward the upper right corner of the scan field), (b) the clusters look as if they were grouped together by the sweeping motion of the STM tip, (c) some clusters disappear from the image half way through their imaging, probably because the STM breaks the chemical bonds between them and the passivating layer.

ATP monolayer

The thiol SAM, discussed in the previous paragraph, provides a good passivation layer for the gold surface, nevertheless it cannot bond metallic clusters unless we functionalise the free ends of the alkane chain. This is because the S-terminated (functionalised) molecules will bind to the Au substrate with both ends rather than standing upright as the C-terminated ones. A way to solve this problem is to use SAMs of molecules with asymmetric end groups. For instance molecules with thiol- and amino- ending groups deposited on a gold surface would form a SAM terminated by amino-groups, which are able to form bonds, for example, with oxide groups (see also the discussion on Pt + cysteamine in the previous paragraph)

Following the work of Rosink et al. [12] we have prepared a gold sample with a self-assembled monolayer of 4-aminothiophenol (ATP). This molecule is composed of an aromatic ring terminated by N- and S- atoms at the opposite ends of the molecule. ATP is known to form a SAM on a gold substrate [12] with the S-ending attached to the film and the N-ending pointing outwards (as shown in Fig. 8a).

The recipe for preparing the ATP SAM is similar to the one for the thiol molecules: the substrates are first cleaned and then immersed in a 1 mM ethanolic solution of
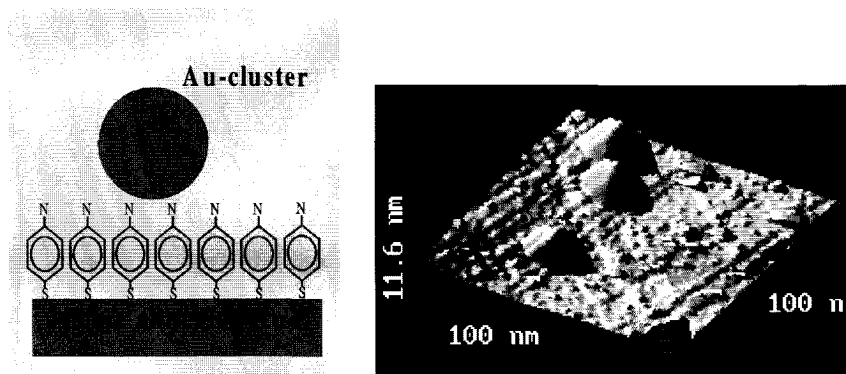
Figure 8a,b: (a, left) Gold clusters are attached to the surface of gold using a self assembled monolayer of 4-aminothiophenol (ATP). One end of the molecules bonds to the substrate with a thiol-Au bond. The other end of ATP terminates with N, which can bond directly to Au clusters or better to the special protective shell used in some experiments (phen*, as explained in the text). (b,right) Low temperature STM image of a sample prepared as from the scheme (a). A few clusters are visible in the scan area 100x100 nm².
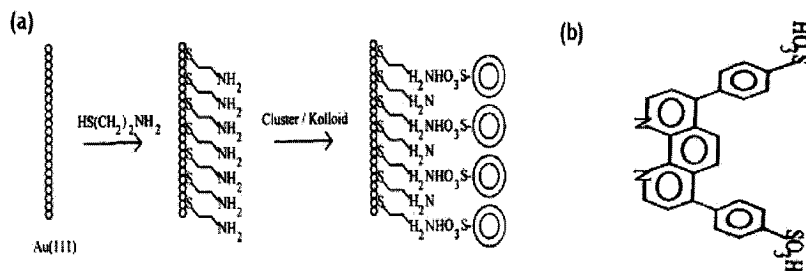
Figure 9: (a) A gold substrate is passivated with a SAM of cysteamine which can bond to Au clusters prepared with a phen* shell. (b) Structure of the phen* molecule.

ATP for 12 to 24 hours in N_2 atmosphere. Then we rinse the samples a few times in pure methanol and ethanol and blow them dry with N_2 to remove the excess ATP from the surface. The samples are stored in vacuum or N_2 atmosphere before use, to prevent oxidation. The ATP SAMs are then imaged with a room temperature STM [3] to make sure that the monolayer is flat and homogeneous. Next we deposit the clusters from solution and image the sample again. Figure 8b shows such an image taken with a low temperature STM: the substrate is flat and the clusters are clearly visible and isolated for one another.

Ligand-stabilised colloids

The colloids we have used in combination with the thiol and ATP monolayers are stabilised in solution by effect of their charge, i.e. the colloids are kept apart from one another by means of electrostatic repulsion. Another common method to stabilise the colloids in solution, is to surround them with an organic shell. The shell encloses the particle and bonds to it with its functional ends on the inner side, while the hydrophilic end groups face the outside and allow the solvability of the particle. In collaboration with Schmidt et al. [13] we have prepared a sample consisting of 4-nm Pd ligand-stabilised colloids on the flat Au surface.

The colloids are stabilized by an organic shell made of batho-phenanthroline (phen*) molecules. The chemical structure of the phen* molecule is shown in Fig. 9b: the two

functional ends of the molecules are the N-end (attaching to the metal particle) and the HSO_3-group (facing outside). The particles are deposited on a gold film passivated with an ATP SAM, prepared as described in the previous paragraph. The HSO_3 group forms a chemical bond with the amino-group of ATP so that the colloids can be strongly fixed to the substrate. A similar shell-to-SAM bond can be formed with cysteamine, as represented in the scheme of Fig. 9a. The clusters are deposited on the SAM from the cluster solution by letting the sample incubate in solution for a few hours.

The colloids are stored in solution with a modified phen* shell: the end-group is $NaSO_3$, instead of HSO_3, because the latter is not stable on a timescale longer than a few hours. The Na^+ ion has to be exchange to H^+ to have the shell bond to the SAM monolayer as described previously. This can be done with an ion-exchange reaction using the mixed bed exchanger Merck 4836 (see also Ref.13).

A very small cluster: Au 55

The study of very small metallic particles is particularly interesting because their spectroscopic features (e.g. the discretisation of their electronic spectrum) can be resolved at room temperature, which is experimentally easier than using low-temperature STM set-ups and has also because of their potential for industrial
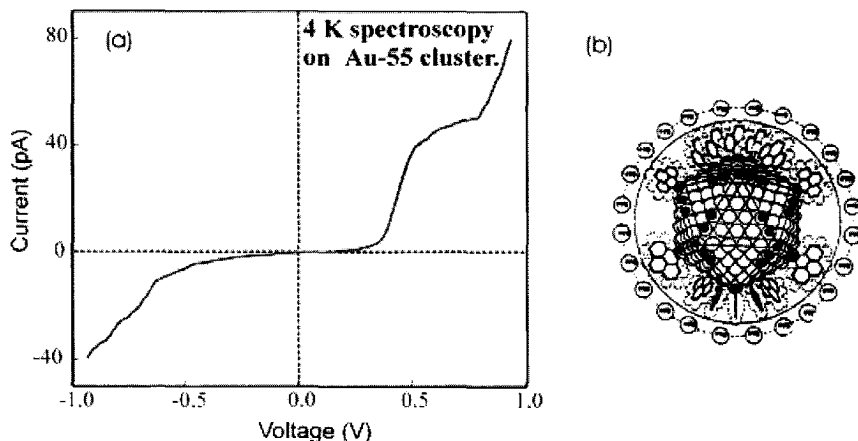

Figure 10: (a) I-V characteristic of the Au_{55} cluster measured at 4K. The discrete spectrum of the particle generates steps in the I-V characteristic. (b) Drawing [14] of a Au_{55} cluster surrounded by a organic shell.

applications. For these reasons we have studied Au_{55}, one of the smallest stable metallic particles with a regular arrangement of atoms (see also chapter 2).

Au_{55} clusters are prepared in solution by Schmid et al. [14] with a ligand-stabilised shell $(Ph_2PC_6H_4SO_3H)$. Figure 10b shows a drawing of the structure of the cluster surrounded by its shell. Note that the shell is not covering the molecule completely, so that the cluster can have different non-equivalent orientations when deposited on the substrate, possibly leading to different interactions between the particle and the substrate. We have measured the spectroscopy on such a cluster deposited on a gold substrate with a thin insulating layer of chromium oxide on top. Figure 10a shows the *I-V* spectroscopy taken at 4.2 K (to improve the stability of the STM): large Coulomb blockade steps can be seen, of the order of 1 eV as expected for a particle of 1 nm in diameter. Considering our results on S-gate experiments (see chapter 4 and 5), Au_{55} is definitely too small to have a significant capacitive coupling to the electrical gate of our probes with the present fabrication techniques.

References

[1] W. Haiss D. Lackey, J.K. Sass, K.H. Besoke, J. Chem. Phys. **95**, 2193 (1991).

[2] A. Ulmann, *Ultrathin organic films,* Academic Press 1991.

[3] We have used the 'Nanoscope' multimode scanning probe microscope by digital instruments. The AFM images were taken in the so-called tapping mode. See also http://www.di.com/appnotes/TapMode/TapModeMain.html.

[4] J.J. Hickman, P.E. Laibinis, D.I. Auerbach, C. Zou, T.J. Gardner, G.M. Whitesides and M.S. Wrighton, Langmuir **8**, 357 (1992).

[5] see for example G. Schmid and F. Chi-Lifen, Advanced Materials **10**, 515 (1998).

[6] G.E. Poirier and E.D. Pylant, Science **272**, 1145 (1996).

[7] C. Kergueris, J.P. Bourgoln and S. Palacin, Nanotechnology **10**, 8 (1999).

[8] G.E. Poirier, T.M. Herne, C.C. Miller and M.J. Tarlov, J. Am. Chem. Soc. **121**, 9703 (1999).

[9] G.E. Poirier, J. Vacuum Science and Tech. B **14**, 1453 (1996).

[10] D.L. Klein, P.L. McEuen, J.E. Bowen-Katari, R.Roth and A.P. Alivisatos, Appl. Phys. Lett. **68**, 2574 (1996).

[11] L.A. Bumm, J.J. Arnold, M.T. Cygan, T.D. Dunbar, T.P. Burgin, L. Jones, D.L. Allara, J.M. Tour and P.S. Weiss, Science **271**, 1705 (1996).

[12] J.J.W.M. Rosink, M.A. Blauw, L.J. Geerligs, E. van der Drift, B.A.C. Rousseuw and S. Radelaar, Optical Materials **9**, 416 (1998).

[13] S. Peschel, Ph.D. thesis, Essen 1997.

[14] G. Schmid, S. Peschel and T. Sawitowski, Z. Anorg. Allg. Chem. **623**, 719 (1997).

Chapter 8

Low Temperature STM on Semiconductor Nanoclusters

L. Canali, L. Gurevich, M. Janus, E. Bakkers, D. Vanmaekelbergh
and L.P. Kouwenhoven

Abstract

We have studied CdSe nanoclusters by low-temperature STM spectroscopy. The clusters have been coated with an organic shell and deposited on a flat metallic surface to obtain a double tunnel barrier configuration. In the case of asymmetric barriers, the STM dI/dV spectroscopies show a series of resonances in the conduction band of CdSe that we interpret as the manifestation of size quantisation. In the case of symmetric barriers, the degenerate levels inside the clusters give rise to a series of satellite resonances in the tunnelling spectra due to charging effects.

Introduction

The study of semiconductor nanocrystals has attracted much attention in recent years because of their peculiar physical properties and possible applications. Various techniques of colloidal chemistry permit the creation of semiconductor nanocrystals with sizes in the nm scale [1]. Moreover the size of the particles can be controlled with a good degree of accuracy, allowing an extra degree of freedom in engineering the properties of these nanocrystals. The electronic spectrum of these particles has been investigated by several groups [2-5]. In particular, STM studies of the the dI/dV spectra of semiconductor nanoclusters have been performed by Banin et al. [6] on InAs colloids and by Alperson et al. [7] on electrochemically deposited CdSe quantum dots on a gold substrate. These authors have experimentally verified that the spectra of semiconductor nanoclusters are fundamentally different from their metallic counterpart because the former have single-level spacings substantially larger than their charging energy, while the converse is true for metallic clusters.

The electronic spectrum of semiconductor clusters can be modelled, in first approximation, with the quantum levels in a spherically symmetric potential-well with hard-wall boundary conditions. Moreover, it is possible, in certain conditions, to observe the *Aufbau* (build-up) of the electronic states inside the nanocluster by tunnelling spectroscopy [6].

In this chapter, we discuss a low-temperature STM experiment on 4-nm CdSe clusters. We measure the dI/dV spectra of the clusters if a double-barrier geometry for the case of symmetric and asymmetric double-barrier junctions. The different symmetries of the barriers mean different occupations of the electrons inside the clusters, which we observe to have profound effects in the tunnelling spectra.

Sample preparation

We prepare our sample by depositing CdSe clusters on a flat Au substrate. A dielectric shell is used to cap the particles and obtain a double tunnel barrier junction, analogously to the experiments reported in chapter 4 and 7. Figure 1 shows an STM image of one of our samples taken at 4.2 K. The triangular structures in the topography are atomically flat terraces from the flame annealed gold substrate. On top

of that we can see a sub-monolayer of nanoparticles. After imaging we position the STM tip on top of an isolated dot to acquire its spectroscopic characteristic. Besides, we can move the tip over a flat area to acquire reference I-V spectra.

The recipe for preparing high quality gold substrates is described in chapter 7. We report in this paragraph the details for the preparation of the CdSe suspensions and samples [8]. First, we dissolve 0.8 g of selenium into 15 g TOP (tri-n-octylphosphine) to prepare the 1.0 M stock solution of TOPSe. For the preparation of the TOPCd stock solution 2.0 g Me_2Cd (STREM chemicals) is dissolved in 15 g TOP. Stoichiometrical amounts of both stock solutions are combined and diluted with TOP to 10 mL and loaded into a 10-mL syringe. A sample of 25 g trioctylphosphineoxide (TOPO) is heated to 400 °C and subsequently cooled down to the desired temperature in the range between 300 and 350 °C. Then the contents of the syringe are quickly added, with a single injection, to the vigorously stirring TOPO solution. Immediately, the solution turns orange/yellow and the temperature drops to 180 °C. The temperature is then increased to 250 °C and stabilised to establish steady growth and annealing of the particles for several hours. The solution is cooled down and the clusters are removed from the TOPO and washed with anhydrous methanol. Finally, the clusters are dispersed in toluene.

Figure 1: Low-temperature STM topography of a Au (111) substrate covered with a submonolayer of CdSe clusters capped with an organic shell (type I sample). The topography allows the controlled positioning of the STM tip over the clusters to acquire their spectroscopy characteristic.
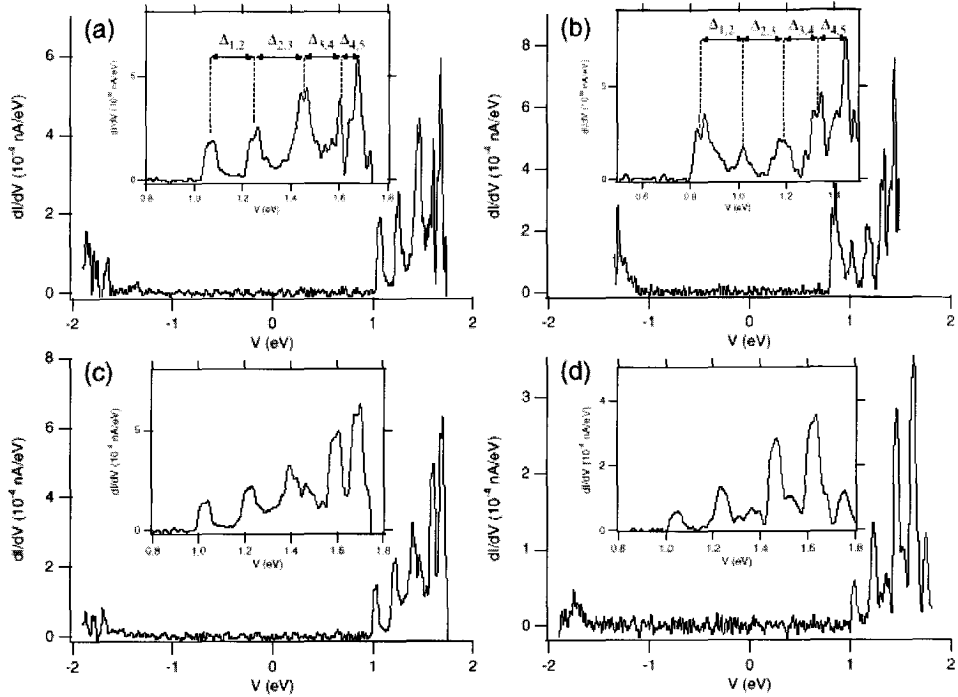
Figure 2: STM spectroscopies measured on single CdSe clusters at 4 K. A large gap of about 2 eV stems from the semiconducting properties of the particles added to the effect of size quantisation. The resonances visible outside the gap originate from the quantum levels inside the cluster. Spectra (a,c,d) are measured on a type I sample with the same set-point, while (b) is taken on a type II sample.

The injection temperature determines the final size of the particles. For the experiments discussed in this chapter we have used CdSe clusters nearly spherical in shape and with diameter 4.3 ± 0.4 nm [9].

Two different types of samples have been utilized. *Type (I):* The original suspension of TOPO-capped clusters is dried under argon and the particles are redissolved in pyridine, which replaces the TOPO. This pyridine capping is subsequently replaced by hexanedithiol molecules by adding a drop of hexanedithiol to the pyridine solution. The particles are interconnected via the hexanedithiol molecules and form supercrystals that precipitate. Ultrasonic vibrations destroy these supercrystals but leave the individual particles undamaged in solution. We deposit the clusters on a flame-annealed gold substrate by leaving the sample in a beaker containing the hexanedithiol-capped CdSe suspension for 16 hours. After that the samples are rinsed

thoroughly with methanol to keep only the clusters that are strongly bound to the substrate. *Type (II) samples.* The gold substrates are annealed and provided with a Self Assembled Monolayer (SAM) of compound **2R**(4,4'-(tetrahydro-4H-thiopyran-ylidene)). This molecule consists of a double carbon ring with two sulphur atoms on the opposite sides. One the first sulphur atoms bonds to the gold substrate, while the other is used to bond a submonolayer of TOPO-capped CdSe clusters.

Measurements

Figure 2 shows the tunnelling spectra acquired above a single CdSe cluster. Spectra 2a, 2c and 2d are taken on a particle capped with TOPO and deposited on a 2-SAM on gold (type II sample). The values of the tunnel current and sample bias used for the STM feedback (the set-point) are 5 pA, 1.4 V. Spectrum 2b is taken on a hexanedithiol-capped nanocrystal, anchored to a bare gold surface (type I sample) with set-point 50 pA, 1.5 V. In all the spectra of Fig. 2 five main peaks are observed
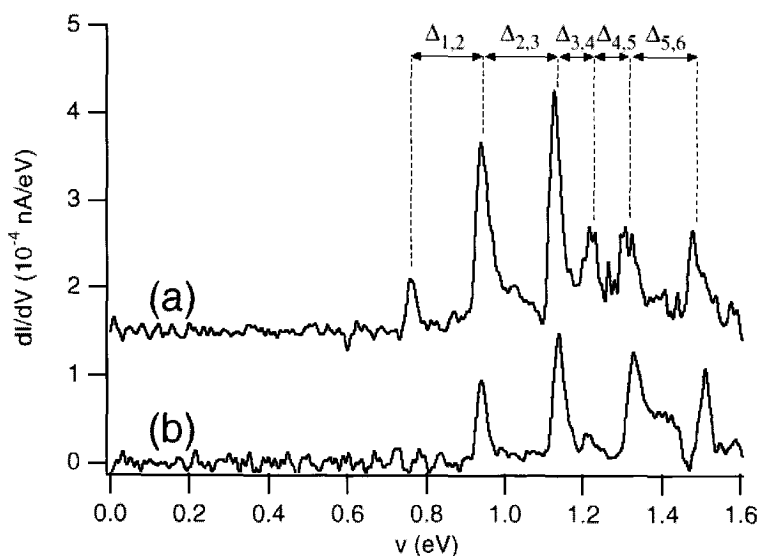

Figure 3: Tunnelling spectra measured on the same CdSe cluster at 4 K for two different values of the tip-particle distance; corresponding to set-point (a) 30 pA, 1.4 V and (b) 10 pA, 1.4 V.

at positive bias with peak spacings $\Delta_{1,2} = 188 \pm 8$ meV, $\Delta_{2,3} = 194 \pm 15$ meV, $\Delta_{3,4} = 150 \pm 20$ meV, and $\Delta_{4,5} = 92 \pm 12$ meV. The relative intensity of the peaks is different for consecutive spectra taken above a single cluster. The peaks at negative bias have a much lower intensity than the peaks at positive bias and are not well resolved. The width of the zero-conductance gap in graphs 2a, 2c and 2d is 2.5 ± 0.1 eV, while it is slightly smaller in graph 2b. We note that samples of type I and II give similar results in spectroscopy, which means that the details of the bond between clusters and substrates do not influence the tunnelling density of states.

In Fig. 3, two consecutive tunnelling spectra obtained above the same cluster at different tip-dot distances are shown. Spectrum 3a (set-point 1.4 V, 30 pA) shows 6 peaks in the positive bias region. The peak spacings are: $\Delta_{1,2} = 181$ meV, $\Delta_{2,3} = 188$ meV, $\Delta_{3,4} = 100$ meV, $\Delta_{4,5} = 85$ meV and $\Delta_{5,6} = 167$ meV. The peak observed at 770 meV is absent in spectrum 3b (set-point 1.4 V, 10 pA), moreover we note that the relative intensity of the peaks does not correlate between the different spectra.

Figure 4 shows tunnelling spectra taken on four different single CdSe clusters when the tip is brought closer to the particle than in the case of Fig 2 and 3 (set-point 60 pA, 1.2 V). This means that the two tunnel barriers become more symmetrical. In all these spectra we note a few main resonances followed by satellite peaks of decreasing intensity. The spacings between the main peaks in the spectra of Fig. 4 are: $I = 316 \pm 13$ meV, $II = 207 \pm 8$ meV, and $III = 160 \pm 10$ meV. While the typical spacing between the satellite peaks is 75 ± 10 meV. Figure 5 shows a tunnelling spectrum for an even smaller tip-dot distance. In the positive bias range two peaks are observed, followed by a series of six peaks with decreasing intensity. In the inset the peaks are shown in more detail. The spacing between the main peaks is $\Delta_{1,2} = 173$ meV, and $\Delta_{2,3} = 247$ meV and the spacing of the satellite peaks is of the order of 40 ± 10 meV. In this case some structure is also visible for negative bias values.
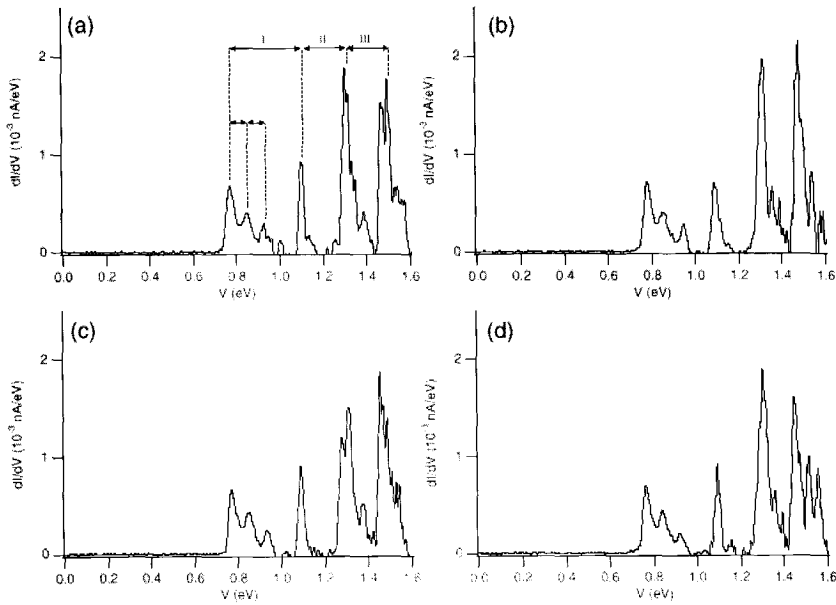
Figure 4: Tunnelling spectra measured on single CdSe clusters at 4 K for a tip-particle distance corresponding to a set-point (60 pA , 1.2 V).
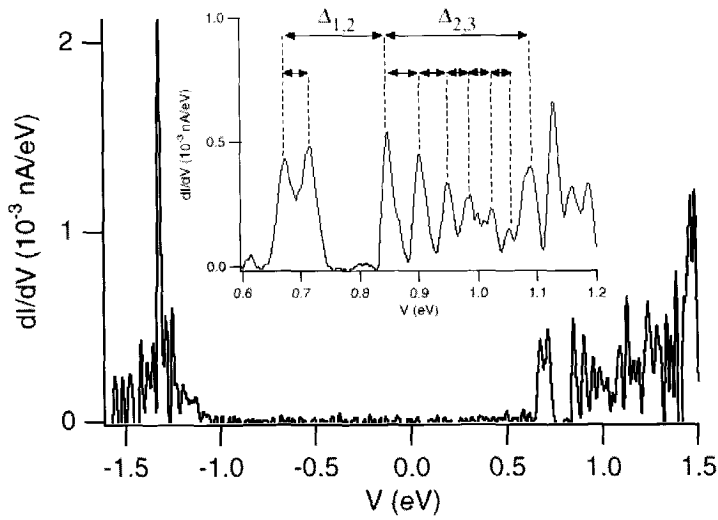

Figure 5: Tunnelling spectrum measured on a single CdSe cluster at 4 K for a tip-particle distance corresponding to a set-point (80 pA, 1.5 V).

Interpretation of the tunnelling spectra

The set-points used to acquire the spectra of Fig. 2 correspond to a large tip-sample separation (it can be estimated as > 0.5 nm with the formulae discussed in chapter 1). Moreover we know that the clusters make a chemical bond to the substrate via their shell. Therefore it is reasonable to model our measurements with a double tunnel-junction geometry with asymmetric barriers. Calling Γ_{in} the tunnelling rate from the tip to the cluster and Γ_{out} the tunnelling rate from the cluster to the substrate. In the case of Fig. 2 we have $\Gamma_{in} \ll \Gamma_{out}$, i.e. the tunnel barrier between the clusters and the substrate has the lowest resistance. Moreover, the bias voltage drops mainly over the junction of lowest capacitance, which is the one between the tip and cluster. Therefore, we interpret the structure at positive bias in the dI/dV characteristics as corresponding to modulations in the density of states of the conduction band of the clusters, and the structure at negative bias as referring to the valence band.

The dI/dV spectra of Fig. 2 show a gap around 0 and a series of peaks outside it. The gap stems from the semiconductor gap of CdSe (1.8 V), while the peaks can be interpreted as a manifestation of the size quantisation effect: the electrons trapped in the cluster behave like particles in a quantum box and thus show a discrete spectrum of levels. We can compare the measured mean level spacing of the peaks at positive bias with the mean level spacing calculated for the first few levels of a quantum box of equivalent diameter: ~200 mV, which is in good agreement with the measurements of Figs. 2 and 3. More complicated effects, such as the polarisation energy of the particles, have to be taken into account for a more precise calculation [10]. Charging effects are of the order of 50 meV and thus negligible in first approximation, as it will be explained in the following discussion.

We model the data of Figs. 2 and 3 by approximating the cluster to a spherical quantum box: the first peak corresponds to the first non-degenerate S electron level, the second peak to the three-fold P degenerate level, etc. We remark that the peaks at negative bias, corresponding to the valence band levels, are not resolved. This is probably due to the complex electronic structure of the valence band of CdSe [5].
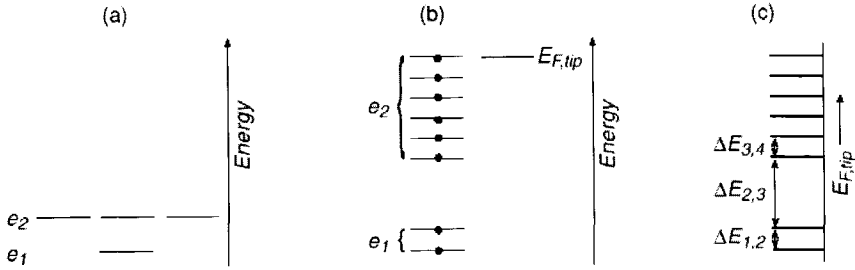
Figure 6: Schematic representation of the effects of electron-electron interactions on the tunnelling spectra. (a) The S- and P- levels in the cluster are shown with their degeneracy (1 and 3). Multiple occupancy in the cluster means that electrons have to 'pay' an extra charging energy to enter the particle. (c) In the case of full occupancy the S- and P- levels will show up as 8 peaks in the dI/dV spectroscopy.

Spectrum 3a shows six peaks at positive bias. Their positions are in fair agreement with the electron energy levels calculated for an electron in a box. For spectrum 3b the tip has been further retracted with respect to its position for spectrum 3a by increasing the tunnel resistance, this causes a drastic decrease of the intensity of the first peak below the noise level. The spatial distribution of the probability density of the orbitals may be important to determine the overall the tunnelling probability. The first level has an *S*-orbital character and the maximum of the probability density is at the centre of the particle. The next three-fold degenerate level has a *P*-orbital character and the probability density for the electronic wave function is higher outside the centre than in the case of *S*-orbitals. If the tunnel junction has a very high resistance, the orbitals with a lower probability density at the surface, as the first S-type level, will have a smaller overlap with the wavefunction of the electrons in the tip. This can be the cause of a reduction of the total tunnelling rate for electrons into the *S*-orbitals (see also chapter 1).

Figure 4 shows four dI/dV spectra, which present a few main peaks followed by a series of satellite peaks. These spectroscopies differ from the measurements of Fig. 2 and 3 mainly for the set-point used in the feedback loop (i.e. in the tip-to-sample distance). We assume that this change is enough to alter the double barrier configuration into a symmetric one, i.e. $\Gamma_{in} \sim \Gamma_{out}$. The fact that the entrance and

escape rate from the cluster are of the same order of magnitude, means that more than one electron can be present in the particle at the same time. Consequently, we observe a change in the tunnelling spectra: when two electrons enter the particle sharing the same level we observe two peaks separated by the charging energy E_c (we neglect exchange interactions for simplicity). Figure 6 illustrates the splitting of the degenerate levels due to multiple occupancy inside the particles: Fig 6a shows the degenerate level as measured in the case of asymmetric barriers. When more electrons are inside the particle, the energy to add an extra electron into level E is equal to $E + n \cdot E_c$ (Figs. 6b and 6c).

The spectrum in Figure 5 was also measured with a small tip-dot distance and shows two peaks followed by a series of six peaks. The first two peaks correspond to the first non-degenerate level and are split by the Coulomb charging effect. The next six peaks correspond to the second three-fold degenerate energy level. The peak splitting of the main peaks was ~170 meV and that of the satellite peaks is ~40 meV. The peak spacing of the satellites corresponds to the total charging energy, multiplied by a numeric factor, which is due to the fact that the bias is distributed over two junctions. The value we measure for the charging energy is in agreement with the measurements of Klein et al. [3] for CdSe nanocrystals of comparable size. A simple estimate for δ can be obtained by calculating the charging energy of a sphere of the same diameter as the CdSe clusters using $\varepsilon_{CdSe} \sim 10\ \varepsilon_0$, we obtain $\delta \sim 60$ meV, which is in reasonable agreement with the experiments. The spectrum if Fig. 5 agrees with the model of Fig. 6c for the case of full occupancy of the orbitals and completely lifted degeneracy. The decreasing intensity of the satellite peaks can be explained by considering that the intensity of the n-th satellite peak is proportional to the probability p_n to have n electrons in the cluster, and that p_n is a decreasing function of n.

Considering the spectra of Fig. 4, we see that the first main peak is followed by two satellite peaks and, therefore, cannot correspond to the first non-degenerate level, where we expect a main peak followed by only one satellite peak. Accordingly, the first set of peaks might correspond to the second three-fold degenerate level, indicating that the first non-degenerate level is not observed in these experiments.

Conclusions

We have studied the electronic excitation spectra of CdSe clusters in a double barrier tunnel-junction configuration. We have utilised a low-temperature STM, which allows the imaging of the clusters deposited on a gold substrate and the controlled acquisition of their spectroscopic characteristics. Two different classes of spectra have been found for different tip-cluster distances, namely measurements with asymmetric barriers for large tip-cluster separation and spectra with symmetric barriers for small separation. The former class presents peaks in the dI/dV spectra that we interpret as the manifestation of single electronic levels due to size quantisation. In the case of symmetric barriers we see an extra structure of satellite peaks, which we interpret as the effect of multiple occupancy in the cluster causing the splitting the degenerate levels into a series of smaller peaks separated by the charging energy of the cluster.

Three-terminal measurements with a scanning gate on this system would provide a better way to understand the nature of the resonances in the dI/dV spectra, for example allowing the study of the level shifts as a function of the applied gate voltage.

References

[1] A.P. Alivisatos, Science **271** 933 (1996)

[2] B. Alperson, S. Cohen, I. Rubinstein and G.I. Hodes, Phys. Rev. B **53**, 17017 (1995).

[3] D.L. Klein, P.L. McEuen, J.E.B. Katari and A.P. Alivisatos, Appl. Phys. Lett. **68**, 2574 (1996).

[4] R.P. Andres, T. Bein, M. Dorogi, S. Feng, J.I. Henderson, C.P. Kubiak, W. Mahoney, R.G. Osifchin and R. Reifenberger, Science **272**, 1323 (1996).

[5] R. Roth, A.K.L. LIM, A.P. Alivisatos and P.L. McEuen, Nature **389** 699 (1997).

[6] U. Banin, Y. Cao, D. Katz and O. Millo, Nature **400**, 542 (1999), O. Millo, D. Katz, Y.W Cao and U. Banin, Phys. Rev. B **61**, 16773 (2000).

[7] B. Alperson, I. Rubinstein, G. Hodes, D. Porath and O. Millo, Appl. Phys. Lett. **75**, 1751 (1999).

[8] C.B. Murray, D.J. Norris and M.G. Bawendi, J. Am. Chem. Soc. **115**, 8706 (1993).

[8] E. Bakkers Ph.D. thesis, chapters 5 and 6, Utrecht (2000).

[10] A Franceschetti and A. Zunger, Appl. Phys. Lett. **76**, 1731 (2000).

Chapter 9

Low Temperature STM on InAs (110)
Accumulation surfaces

L. Canali, J. W. G. Wildöer, O. Kerkhof and L. P. Kouwenhoven

Abstract:

The properties of InAs (110) surfaces have been investigated by means of low-temperature scanning tunnelling microscopy and spectroscopy. A technique for *ex-situ* sulphur passivation has been developed to form an accumulation layer on such a surface. Tunnelling spectroscopy at 4.2 K shows the presence of localised states in the accumulation layer, probably due to the formation of a surface 2D gas. Measurements in high-magnetic field demonstrate Landau quantisation of the energy spectrum, both in the accumulation layer and the 3D bulk conduction band.

Introduction

The properties of 2D electron gases (2DEG) subject to high magnetic fields have generated a large amount of theoretical and experimental work. In particular, the study of edge channels and electron-electron interactions [1] is currently a field of great interest. Spatially resolved imaging of edge channels was performed by van Haren *et al.* [2], using a special technique to obtain macroscopically wide channels. More recent work on the subject of imaging the edge channels and the quantum Hall fluid in general, are reviewed in chapter 3. For measurements with the highest spatial resolution one would like to exploit the potential of STM techniques. However, this requires a semiconductor system having a clean 2DEG at the surface. InAs is a good candidate material, since it is known that it can have a surface 2DEG [3]. Wildöer *et al.* [4] have performed low-temperature scanning tunnelling microscopy and spectroscopy on InAs (110) surfaces that were cleaved *in situ* at 4.2 K. A clean surface was obtained and Landau quantisation was observed. In that study, however, no clear evidence was found for the formation of a surface 2DEG.

In this chapter we report on the development of a suitable system for STM studies on a 2DEG: the sulphur-passivated InAs (110) surface. We present evidence of the presence of 2D subbands and their Landau quantisation in high magnetic fields, investigated by low-temperature STM.

From the work of Tsui [3], it is known that an oxide layer at the surface of n-type InAs pins the Fermi energy above the bottom of the conduction band, thereby forming a surface accumulation layer. We have found that the oxidation of the InAs surface is not a practical *ex-situ* technique for STM investigation, since the oxide grows too thick already after a few minutes of exposure to air. We have therefore studied different passivation techniques for InAs taking advantage of its chemical similarity with GaAs, for which a vast literature of passivation methods is available. Such techniques mainly use reactive S-containing solutions and/or gases. In practice, we have focused on two among the most practical and relatively less toxic wet techniques: one employing a solution of $(NH_4)_2S$ as in Ref. 5, the other one using a solution CH_3CSNH_2/NH_4OH at 90 $^\circ$C as in Ref. 6.

(a)

(b)
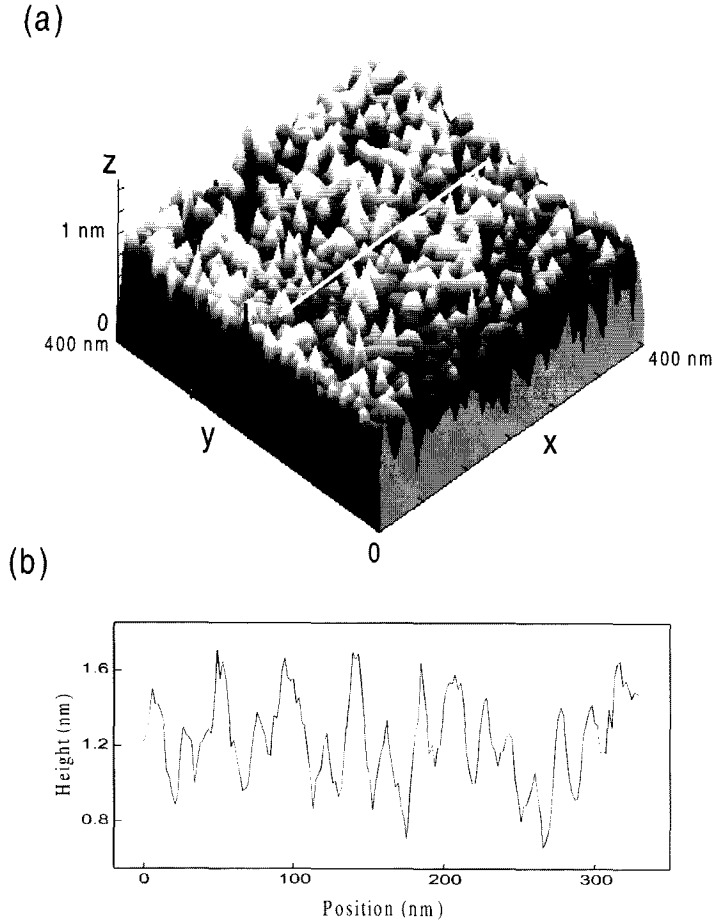
Figure1: (a) STM topographic image at 4.2 K of the InAs (110) surface S-passivated with CH$_3$CSNH$_2$/NH$_4$OH for 40 seconds. The image shows a rms roughness of 0.5 nm over an area of 400 × 400 nm^2. (b) Line profile along the line indicated in the topography.

Sample preparation and characterisation

We use InAs wafers with a doping concentration $n = 2.4 \cdot 10^{16}$ cm^{-3}, corresponding to a Fermi energy $E_f \cong 13$ meV above the conduction band. Passivated samples are prepared by cleaving in solution after scribing a mark on the (100) surface. We study different samples with passivation times between 5 seconds and 20 minutes. After

passivation, samples are rinsed in de-ionised water and blown dry with nitrogen gas. They are then quickly mounted in our STM [7], being thus exposed to air for about 10 minutes. The STM vacuum-can is then pumped out for about 90 minutes (at room temperature) in order to sublimate the excess sulphur [8]. Helium exchange gas is allowed in the STM vacuum can just before cooling down to 4.2 K in a cryostat equipped with a 7 T superconducting magnet (see also chapter 1). The STM tips are cut in ambient from Pt(90%)Ir(10%) wire.

Figure 1 shows a typical topographic image of the S-passivated InAs surface at 4.2 K. The surface has a root-mean-square (rms) roughness of about 0.5 nm over an area of 400×400 nm^2. Topographies for areas of 10×10 nm^2 can show an rms roughness of about 0.1 nm. Despite this flatness, topographic images do not show atomic resolution. Similar results were found for GaAs by Gwo et al. [5]. We find that the thickness of the sulphur passivation layer amounts to a few monolayers, unlike the case of oxygen passivation.

Different measurements taken on samples with passivation times between 5 seconds and 10 minutes show that the flattest surfaces are obtained for passivation times shorter than 2 minutes. For longer passivation times the rms roughness increases up to a few nanometers. Concerning the rms roughness, we find similar results for both the above-mentioned passivation methods. From Auger spectroscopy measurements we find that the content of oxygen at the surface is significantly lower for the samples passivated with CH_3CSNH_2/NH_4OH than for the ones passivated with $(NH_4)_2S$.

Spectroscopic measurements

Figure 2 shows the I-V characteristic of a S-passivated InAs sample. The onsets of the conduction and valence band are found at about 0 and -400 mV respectively, and are indicated by arrows in Fig. 2. These values are in good agreement with the value for the gap of bulk InAs at 4.2 K: 420 meV. Other authors [4,9] have encountered tip-induced band bending while measuring STM spectroscopy on InAs cleaved in situ. The actual tip-sample voltage was found to be less than the applied bias of about 200 mV, for low-doped samples. We find that our samples do not present appreciable tip-induced band bending. In Fig. 3 (a) a typical spectroscopic measurement at 4.2 K is

reported. Three peaks are seen for negative bias positions: $V_0 = -131$ mV, $V_1 = -85$ mV, $V_2 = -37$ mV, and a fourth smaller peak, $V_3 = -17$ mV. We ascribe these peaks to tunneling from 2D electronic subbands in the accumulation layer at the InAs surface (see Fig. 4). The exact calculation of the confinement potential in the accumulation layer requires numerical self-consistent calculations [10]. We can use a simple expression for the energy values of the 2D subbands when we approximate the confining potential by a triangular well [11]:

$$ E_k = \left(\frac{\hbar^2}{2m^{**}} \right)^{1/3} \left[\frac{3\pi eF}{2} \left(k + \frac{3}{4} \right) \right]^{2/3} \tag{1} $$

Here F is the electric field, $k = 0, 1, \ldots$ is the subband index, and the zero for the energy is taken at the bottom of the well. From Eq. 1 we find $E_k / E_0 = (4k / 3 + 1)^{2/3}$. The energy of the quantum states measured from the bottom of the conduction band is $E_k = \mathcal{E}_p + eV_k$, where V_k are the measured peaks positions, and $\mathcal{E}_p$ is the Fermi-energy
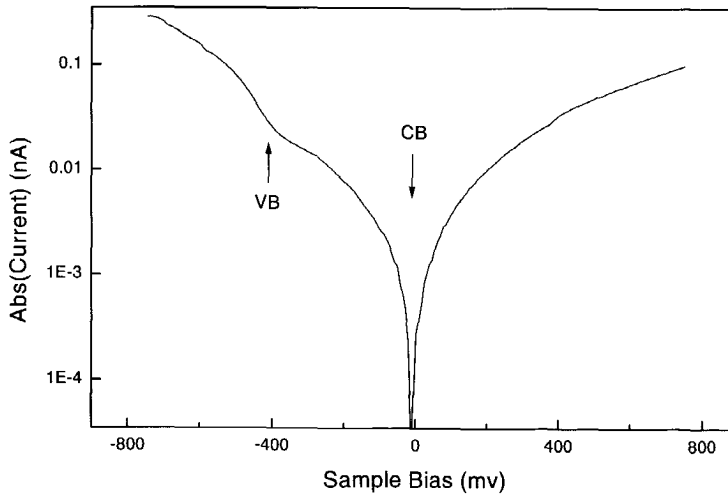
Figure2: STM spectroscopy at 4.2 K of the InAs (110) accumulation surface S-passivated with CH₃CSNH₂/NH₄OH for 40 seconds. From the dI/dV / I/V characteristic, the onset of the conduction (CB) and valence (VB) band are found at about 0 and -400 mV, respectively. This is in good agreement with the value of the gap of InAs (420 meV).
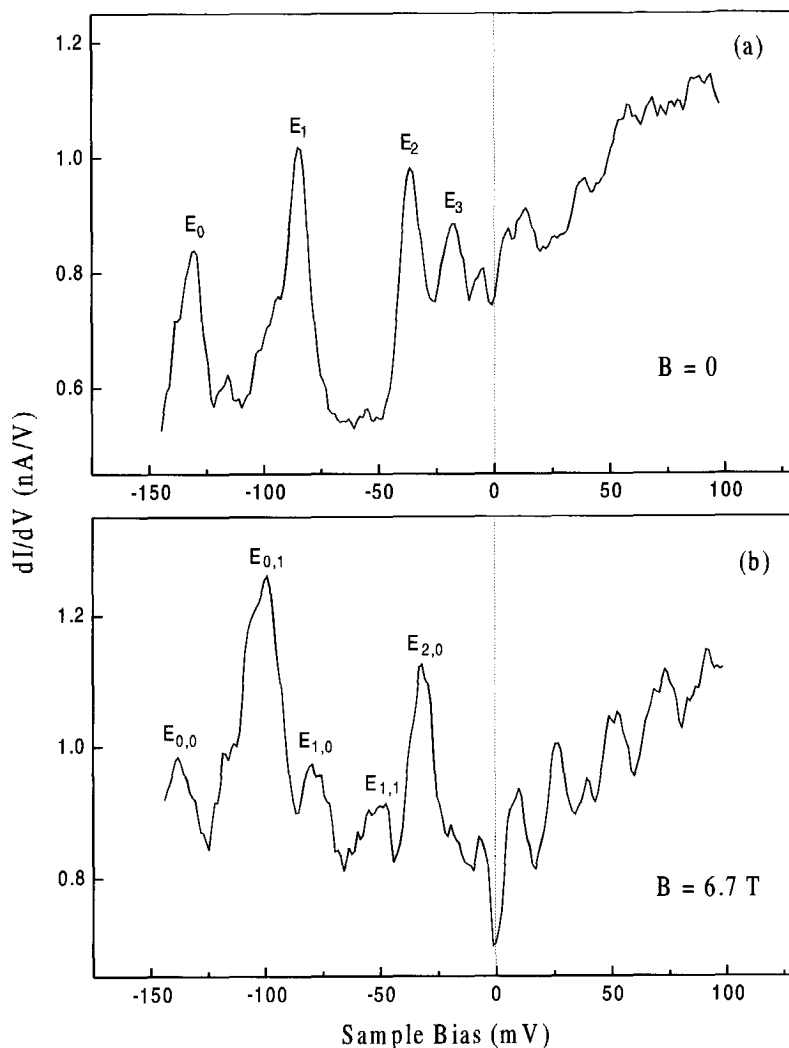
Fig.3. (a) STM spectroscopy at 4.2 K of the InAs (110) accumulation surface S-passivated with CH₃CSNH₂/NH₄OH for 40 seconds. Four peaks can be resolved for negative sample bias at the values: -131, -85, -37 and -17 mV. This graph is calculated by numerical differentiation of the measured I-V characteristic.. (b) STM spectroscopy as in (a) but with a magnetic field B = 6.7 T perpendicular to the surface. Peaks at negative sample bias values of: -138, -99, -79, -49 and -32 mV are observed indicating Landau splitting of the 2D subbands. Additional peaks for positive bias values: 10, 26, 50, 73 and 91 mV are due to Landau quantisation in the conduction band of InAs. The tunnel resistance is about 1 GΩ. I-Vs are measured after turning the feedback control off. We average I-Vs over 25 curves each consisting of 201 points with acquisition time of 1.3 ms per point.

pinning value (see Fig. 4). From the 4 observed peaks we obtain: $\mathcal{E}_p = 194 \pm 5$ meV.

From Eq. 1 and the calculated value for $\mathcal{E}_p$ we find for the accumulation electric field

$F \approx 4 \cdot 10^6$ V/m. The accumulation length $L_a = \mathcal{E}_p / F$ is about 50 nm. From Eq. (1) and

the given values of $\mathcal{E}_p$ and F we can calculate the peak positions: $V_0 = -128$ mV, $V_1 = -78$ mV, $V_2 = -37$ mV, and $V_3 = -10$ mV, with an uncertainty of ± 5 mV; in good

agreement with the measured values.

Peaks in the dI/dV vs. V characteristics for negative bias are observed in all our S-passivated samples. Peaks are absent in those areas where a tip crash has removed the surface layer. We find that the position of the peaks vary on the order of 10% (that amounts to ± 10 meV for the lowest level) for tip displacements of the order of 1 nm.

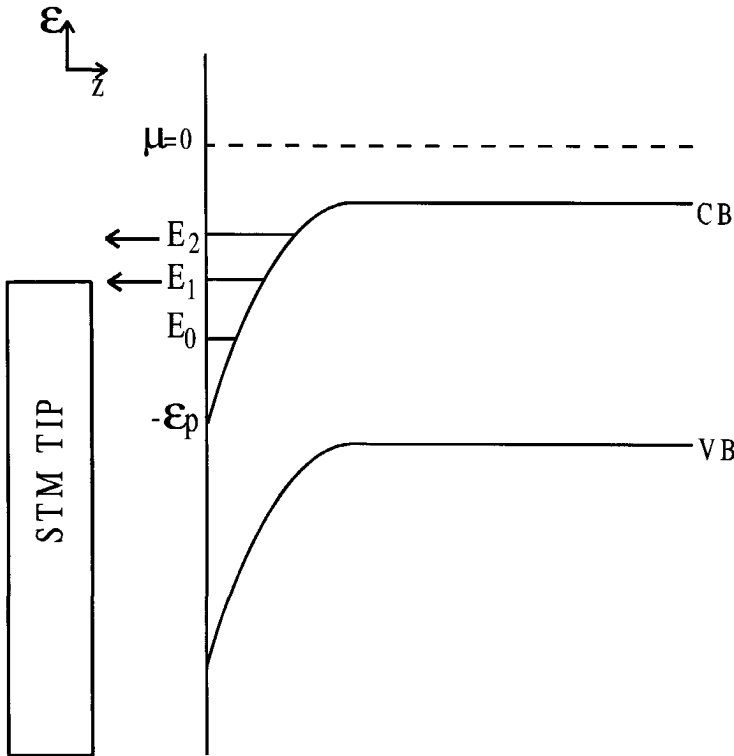*Figure4: Schematic band diagram of n-type InAs for the case of Fermi energy pinning. The conduction band bottom at the surface is bent at the energy $-\varepsilon_p$ below the Fermi level. If the electric field in the accumulation layer is sufficiently strong, quantised 2D states are present at the surface (indicated with E_k). When the Fermi level of the tip is aligned with a 2D state, a peak in the dI/dV is expected.*

After moving the tip around a few nanometers and coming back to the initial spot we find a different tip-sample distance and slightly different peak positions. What may happen is that the tip touches the S-layer and eventually traps some sulphur atoms in an uncontrollable way.

We conclude that the change of peak voltage values as a function of the lateral displacement of the tip does not provide direct information on the electronic localisation length. Instead it depends in a complicated and irreversible way on the configuration of the sulphur atoms around the STM tip and on the properties of the InAs accumulation layer.

In the simplest picture of the STM, the dI/dV characteristic is expected to measure the density of states of the probed system. This result is derived within the approximation of taking the tunnelling matrix element between tip and sample as a constant. In the case of an ideal 2DEG a step-like characteristic is expected, a new step arising for energies corresponding to the bottom of a 2D subband. Previous experiments [12,13], with planar tunnel junctions made of Pb-Oxide-InAs, have demonstrated the presence of a surface 2DEG. In those experiments the electric field is expected to be much more uniform than in ours, while the dI/dV characteristics can still be interpreted as in the case of STM [12]. In Ref 12 and 13 peaks were found in the dI/dV with a broadening between 25 and 40 meV. Peak positions were interpreted as the onsets of 2D subbands and the broadening as due to electrical field inhomogeneity. Moreover the measured values for the bottom of the 2D subbands measured in Ref. 12 and 13 are in good agreement with our results. Therefore we think to have reproduced and extended those results in our STM spectroscopies. We interpret our peaks as arising from the discontinuity in the density of states of the surface 2DEG, that is expected when the Fermi energy of the tip is aligned with the bottom of a 2D subband. The measured width of our peaks is about 15 meV.

Comparing dI/dV vs. V spectroscopy for the two passivation-methods we find that samples passivated with CH_3CSNH_2/NH_4OH, for times less than 2 minutes, give spectroscopic characteristics with the best reproducibility and the highest resolution. In particular, on the sample that was passivated with CH_3CSNH_2 / NH_4OH for 40 seconds we found an area of about 10×10 nm^2 where the peak positions reproduced within 10 meV. Spectroscopies taken in that area are shown in Fig. 3.

Spectroscopy in high magnetic field

Figure 3 (b) shows the dI/dV vs. V characteristic with a magnetic field B = 6.7 T applied perpendicular to the surface. This characteristic has been measured at the same point as Fig. 3 (a), but with the caveat that the magnetic field can cause a lateral displacement of the tip of the order of a few nanometers. We now discuss a simple model to interpret the oscillations present in high magnetic field characteristics.

Landau quantisation is expected for sufficiently strong magnetic field $\hbar\omega_c > \Gamma$, where $\hbar\omega_c = \hbar eB/m^*$ is the cyclotron energy, i.e. the energy separation between different Landau levels, and Γ is the broadening of the Landau levels due to disorder. Landau levels have energies $E_{k,n} = E_{k,0} + \hbar\omega_c(n+1/2)$, where k = 0, 1,... is the electric field quantisation number as in Eq. 1, and n = 0, 1,... is the Landau level index. The magnetic field changes also the value of the Fermi energy with respect to the bottom of the conduction band in the bulk InAs. Most probably, also the value of the electric field in the accumulation layer changes such that the bias position of the "electric
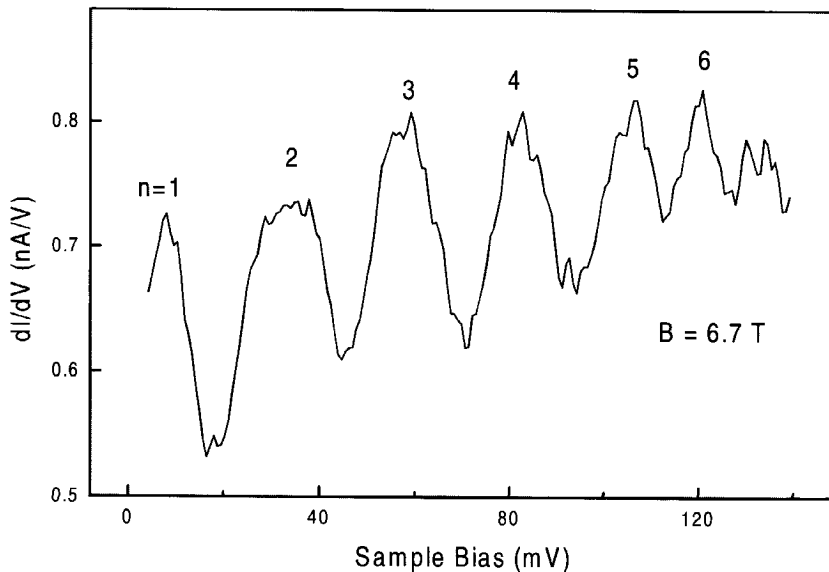
Figure5: STM spectroscopy at 4.2 K of InAs (110) accumulation surface S-passivated with CH₃CSNH₂/NH₄OH for 30 seconds. Six peaks can be resolved for positive sample bias: 8, 35, 59, 83, 106, 121 mV, indicated with n = 1,..6. They are due to tunnelling of electrons into empty Landau levels in the conduction band of InAs.

peaks" ($E_{k,n=0}$) is expected to be shifted a few meV from the B = 0 peaks. We expect peaks in the dI/dV characteristic from the Landau levels at a distance of $\hbar\omega_c(6.7\ T) =$ 33 meV from the 'electric peaks'.

Comparing the two characteristics in Fig. 3 (a) and (b), respectively for B = 0 and 6.7 T, we see that the "electric peaks" present in (a) reproduce also in (b) with a shift of ±7 meV. Two extra peaks are present in (b) that can be interpreted as due to tunnelling from the levels $E_{0,1}$ and $E_{1,1}$ with a measured cyclotron energy of 39 meV and 30 meV, respectively. We note that for lower magnetic field and/or for other samples the spectra manifested magnetic field dependence but no clear peak splitting was found. From this fact we find an upper boundary for the Landau level broadening $\Gamma \approx 35$ meV.

In Fig. 3 (b) peaks in the *dI/dV* vs. *V* characteristic are also present for positive sample bias. We interpret these peaks as due to Landau quantisation in the conduction band of InAs. The energy spectrum of electrons in the conduction band in presence of a magnetic field directed along the z-axis is $E_{k_z,n} = \hbar^2 k_z^2/2m + \hbar\omega_c(n + 1/2)$, where k_z is the wave vector in the z direction. The spectrum is continuous, but the density of states contains singularities at the energies $\hbar\omega_c(n + 1/2)$. These singularities are also expected to give rise to peaks in dI/dV characteristics. The Fermi energy in bulk InAs, for the given electron density and B = 6.7 T, is located at about 4 meV above the first Landau level. Peaks in the dI/dV, for positive bias, are then expected to be due to tunnelling of electrons into the empty Landau levels with numbers n = 1, 2,...

Figure 5 shows the *dI/dV* characteristic in a magnetic field $B = 6.7$ T for a sample passivated with CH_3CSNH_2/NH_4OH for 30 seconds. Six peaks can be clearly distinguished, due to tunnelling into the Landau levels n = 1 to 6. The level spacing gives a measure of the cyclotron energy $\hbar\omega_c = 23 \pm 4$ meV. From this value we can calculate the effective mass: $m^*/m_0 = 0.033 \pm 0.006$, which is higher than the value of the mass at the bottom of the conduction band: $m^*/m_0 = 0.024$. We attribute this discrepancy to mass non-parabolicity in the conduction band of InAs [12,13]. Peaks due to Landau quantisation in the conduction band have been observed for different samples in magnetic fields above 6 T.

Conclusions

We have developed a technique for *ex-situ* near-monolayer passivation of InAs, we have measured, by STM spectroscopy, discontinuities in the tunnelling density of states at the S-passivated (110) surface of InAs and shown the presence of Landau quantisation in high magnetic fields. We have interpreted our measurements as the first direct observation by STM of a 2D electron gas at the surface of a semiconductor. We have shown that our system avoids the problems of tip-induced band banding, and we have studied Landau quantisation in the conduction band of InAs, where up to six Landau levels have been clearly resolved.

Notes: since the publication of this work, R. Dombrowski et al. [14] have studied the tip induced band bending induced by the STM tip on the freshly cleaved InAs (110) surface. They measured peaks in dI/dV below the conduction band and investigated their behaviour under high magnetic fields. The authors have interpreted the measured peaks as the manifestation of tip-induced localised states.

We have recently become aware of the work of Kemerink et al. [15] who have successfully improved the S-passivation of a III-V heterostructure by annealing it for 10 min. at temperatures between 200 and 400 ^{0}C.

References

This work was published in: Appl. Phys. A **66**, 113 (1998).

1. D. B. Chklovskii, B. I. Shklovkii, and L. I. Glazman, Phys. Rev. B **46**, 4026 (1992);
A. A. Koulakov, M. M. Fogler, and B. I. Shklovskii, Phys. Rev. Lett. **76**, 499 (1996).

2. R. J. F. van Haren, W. de Lange, F. A. P. Blom, and J. H. Wolter, Phys. Rev. B **52**, 5760 (1995).

3. D. C. Tsui, Phys. Rev. Lett. **24**, 303 (1970).

4. J. W. G. Wildöer, C. J. P. M. Harmans, H. van Kempen, Phys. Rev. B **55**, R16013 (1997).

5. S. Gwo, K-J Chao, C. K. Shih, K. Sadra, and B. G. Streetman, Phys. Rev. Lett. **71**, 1883 (1993).

6. E. D. Lu, F. P. Zhang, S. H. Xu, X. J. Yu, P. S. Xu, Z. F. Han, F. Q. Xu, and X. Y. Zhang, Appl. Phys. Lett. **69**, 2282 (1996).

7. J. W. G. Wildöer, A. J. A. van Roy, H. van Kempen, and C. J. P. M. Harmans, Rev. Sci. Instrum. **65**, 2849 (1994).

8. Y. Nannichi, J. -F. Fan, H. Oigawa, and A. Koma, Jpn. J. Appl. Phys. **27**, L2367 (1988).

9. R. M. Feenstra, Phys. Rev. B **50**, 4561 (1994).

10. An-zhen Zhang, J. Slinkman, and R. E. Doezema, Phys. Rev. B **44**, 10752 (1991).

11. *Quantum semiconductor structures*, pp 19-20, C. Weisbuch, and B. Vinter, Academic press (1991).

12. D. C. Tsui, Phys. Rev. B **4**, 4438 (1971).

13. H. Reisinger, H. Schaber, and R. E. Doezema, Phys. Rev. B **24**, 5960 (1981).

14. R. Dombrowski, chr. Steinebach, Chr. Wittneven, M. Morgenstern, and R. Wiesendanger Phys Rev. B **59**, 8043 (1999).

15. M. Kemerink, J. W. Gerritsen, P. M. Koenraad, H. van Kempen, and J. H. Wolter, Appl. Phys. Lett. **75**, 3656 (1999).

Chapter 10

Local Probing of the Giant Magnetoresistance

S.J.C.H. Theeuwen, L. Canali, S. Radelaar, C.H. Marrows,

B.J. Hickey, J. Caro and L.P. Kouwenhoven

Abstract:

We use a low-temperature scanning tunnelling microscope in contact mode to measure the local giant magnetoresistance (GMR) of a Co/Cu magnetic multilayer. We find GMR modulations of the order of 10% with occasional values up to 60%. We attribute the variations of the GMR modulations to fluctuations of the structure of the multilayers. The GMR curves are processed in order to subtract the background signal generated by the magnetostriction of the STM scan head.

Introduction

The giant magnetoresistance (GMR) of Co/Cu magnetic multilayers (MLs) has recently been studied using mechanical [1] and nanofabricated [2] point contacts, with diameters down to about 5 nm. These contacts have a geometry intermediate between current-perpendicular-to-plane (CPP) and current-in-plane (CIP), so that thei GMR should exceed the current-in-plane (CIP) GMR. however, the point-contact GMR ratio (=$\Delta R/R_{sat}$, with ΔR the resistance change and R_{sat} the saturation resistance) is only about 5%, which is smaller than the corresponding CIP ratio of the whole ML. It is not clear whether this low GMR is an intrinsic property of point contacts or GMR nano-structures in general, or due to dead layers at the bottom of the ML stack [2], or damage introduced to the ML [1,2]. In this chapter we use a scanning tunnelling microscope (STM) to form a point contacts to a GMR ML (see the inset of Fig. 1 for a cross-section). Contact formation is by very gently touching the tip to the high-quality top layers of the ML, thus avoiding the previous drawbacks. The small contact size combined with the scanning capabilities of the STM enable the mapping of the local GMR of the ML.

Description of the samples

The magnetic multilayers comprise 25 repeats of a [Co(2 nm)/Cu(x nm)] period with x = 1, 2 nm, corresponding to the first and second peak of anti-ferromagnetic coupling between the Co layers, respectively. They are deposited on a Nb(100nm)/Cu(4nm) composite buffer and capped with a 3.4 nm (x = 1 nm) or 2.4 nm (x = 2 nm) thick Au layer to prevent oxidation [3]. The complete stack is sputtered on a Si substrate without breaking the vacuum. Before making point contacts to these MLs, we perform CIP control measurements. These yield a regular in-plane field and perpendicular field GMR. The CIP GMR ratios of the MLs at 10 K (*i.e.* above T_c of Nb) and corrected for the parallel conductance of the Nb buffer, are 30% and 20% for the first and second peak, respectively.

The point contacts are made at 4.2 K by contacting the surface of the ML with the Au- or Pt/Ir- tip of a low temperature STM [4], mounted in a magnet cryostat. The measurements are also taken at 4.2 K, where Nb is superconducting. Thus, the small

CIP series resistance of the ML is completely shunted by the Nb, leaving only the point-contact contribution. The sample is mounted in the STM with the film plane perpendicular to or at an angle of 25° with the magnetic field, which is parallel to the tip. This allows magnetoresistance (MR) measurements in the perpendicular and approximately in-plane (further called in-plane) orientation of the ML.

Experiments

We first test contact-mode operation of the STM by contacting a 100 nm thick Au film with a Pt/Ir-tip. Using the STM coarse approach, the tip is moved towards the film to a distance of ~0.5 nm from the surface. Then we switch off the feedback and gently touch the surface with the tip by tuning the piezo voltage. The contact resistance is controlled between several tens of mΩ and about 13 kΩ. While retracting the tip, we repeatedly observe quantised conductance plateaux around integer multiples of the quantum of conductance: $n \times (2e^2/h)$, with $n = $ 1-5 [5]. Point-contact spectra taken from several contacts display a clear phonon peak at the position characteristic of transverse acoustic phonons in bulk Au [6]. This signature of ballistic electron transport through the constriction, and the observation of conductance plateaux demonstrate our ability to controllably make good contacts.

Point contacts to both types of Au capped ML films are made as described for Au films. We have made dozens of runs, contacting a fresh tip to a ML. In each run many contacts with different resistances are made at different spots (resulting in what we call a sequence of resistances). We vary the resistance at one spot by moving the tip with the z-piezo. Often the point-contact MR is flat, in spite of careful contacting. Nevertheless, enough contacts yield an MR maximum with characteristics of a GMR. The MR ratio is in the range 1÷80% for resistances below 80 Ω, reaching for this type of ML unprecedented values in excess of hundred percent for resistances above 80 Ω. These high values are reminiscent of the recently reported large MR of atomic size Ni-Ni contacts [7], which is attributed to an abrupt domain wall.
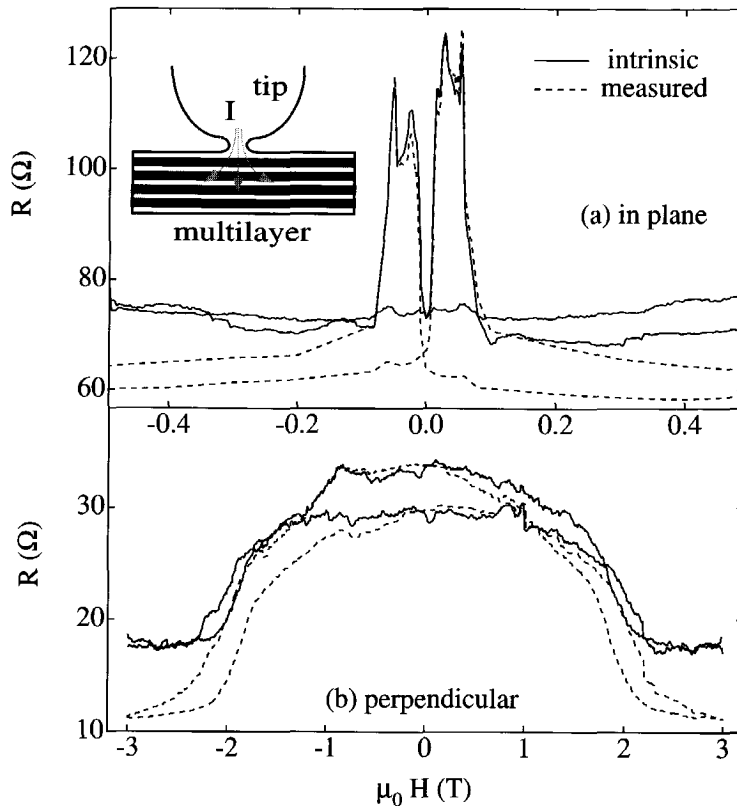
Figure 1. Magnetoresistance traces of point contacts between a Pt/Ir tip and a [Co(2nm)/Cu(2nm)]$_{25}$ multilayer for the in-plane (a) and perpendicular orientation (b). Dashed lines: as-measured curves. Solid lines: GMR after correction for the tip-displacement. Inset: schematic cross-section of a contact between the tip and a multilayer. The contact has a close-to-CPP geometry.

The behaviour of MR ratio versus contact resistance shows a stronger scatter for MRs taken from different spots than for a sequence of MRs from a single spot. We relate part of this scatter to variation of the ML quality, e.g. spread in layer thickness, interface roughness, and relative alignment of the magnetization of the Co layers at H = 0. The variation is resolved due to the small contact size and limited probing depth, implying absence of averaging over a large area and many bi-layers.

MRs coming from two sequences of contacts to a second-peak ML are shown in Figs. 1a and 1b (dashed lines), for the in-plane and perpendicular orientation. The field scale and hysteresis of the MRs are consistent with those of the CIP-controlled GMR. The MR ratios are about 80% for Fig. 1a and 200% for Fig. 1b, both larger than the CIP ratio. In Fig. 2 we plot for second-peak ML contacts and for in-plane fields the MR ratio versus resistance, using the resistance in saturation, the better-defined magnetic state. The open symbols are data points for as-measured curves. The square and triangular symbols represent two sequences, the point at 57 Ω corresponding to the curves plotted in Fig. 1a. Circular symbols (below 25 Ω) represent contacts at different spots. As can be seen, for $R < 25$ Ω (diameter > 10 nm) the ratios are small ($\approx 5\%$), which we attribute to damage in the ML due to the indentation of the tip. In this range the coercive field increases strongly with decreasing resistance, as shown in Fig. 2 (left axis) as well. In the range 40÷80 Ω, the coercive field saturates nearly at
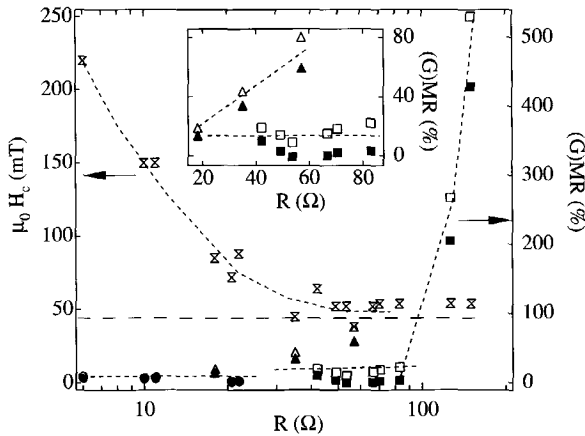
Figure 2. (G)MR ratio (right axis) of [Co(2nm)/Cu(2nm)]$_{25}$ contacts versus the saturation resistance for the in-plane field orientation. Open symbols: as-measured. Solid symbols: GMR. Corresponding coercive fields (left axis, hour-glass symbols) versus saturation resistance. Inset: expanded plot of the (G)MR for the intermediate resistances. Dashed line at 45 mT: coercive field of the CIP control GMR. Other lines guide the eye.

the film value (45 mT). This means that small indentations by the tip affect the ML only weakly. In this range the two sequences behave differently, the MR ratios varying between $10 \div 80\%$ (inset of Fig. 2). Above 80 Ω (diameter < 3 nm) a strong increase of the MR ratio sets in, reaching a huge value of 530% for $R = 150$ Ω.

Globally, contacts to first-peak MLs behave similarly. They also show a strong increase of the MR ratio above an onset resistance, even up to values the maximum second-peak MR ratio. Among the sequences the onset resistance varies in the range $5 \div 60$ Ω. Besides, the MR of these contacts has a saturation field of 200 mT instead of 2 T for the CIP-controlled GMR. This may arise from the weaker coupling of the top Co layer, which is only exchange coupled to one Co layer, giving smaller saturation field. However, we believe that the deviating field scale and the turn-up to large MR ratios with increasing contacts resistance have an origin extrinsic to the ML, involving the effect of magnetic fields on the STM scan head.

Displacement effect

These point contacts are very sensitive to a small displacement of the tip relative to the film, so that a field-dependent displacement intrinsic to the STM may play a role. To check this, we measure the MR of contacts to a Au film, which should be much weaker [8] than the effect in Fig. 2. The resulting MRs are negative, parabola-like and, most importantly, strong (up to 200%). This is exemplified in Fig. 3a. Therefore, we interpret this resistance change as a field-dependent deformation of (parts of) the STM, resulting in increasing indentation of the film by the tip with increasing field, and thus a lower resistance. This agrees with the increasing tunnel current with increasing magnetic field measured in tunnelling mode of the STM. We attribute the deformation to magnetostriction of the STM, which means that the length of STM changes in presence of a magnetic field [9]. The Au contact senses the magnetostriction, so that the ordinate of Fig. 3 actually represents magnetostriction. Thus, part of the ML contact-MR arises from this displacement effect. The magnetostriction effect of the ML itself is negligible [9].

The field scale of the overall displacement effect in Fig. 3a is comparable to that of the MR of Fig. 1b and much larger than the MR of Fig. 1a. Thus, the overall displacement can strongly affect the perpendicular GMR, but can hardly alter the in-

plane GMR. More serious for the latter, however, is the fine-structure present in the curve of Fig. 3a close to $H = 0$. This fine-structure, plotted in Fig. 3b on an expanded scale, together with scaled MRs representative of first- and second-peak contacts of intermediate resistance ($40 \, \Omega < R < 80 \, \Omega$), has a hysteretic maximum at about 55 mT, independent of the contact resistance. The fine structure corresponds to a displacement of about 0.4 nm, as follows from the piezo voltage change of its tunnelling mode counterpart. Quite incidentally, the field position and shape of the fine structure are very similar to those of the MR of the first-peak contacts (see Fig. 3b). This indicates that the MR of the first-peak contacts mainly originates from the displacement. However, such a strong similarity does not hold for the fine structure and the MR of the second-peak contacts, which are clearly separated (Fig. 3b). Rather, the field position of the second-peak contact is very close to the peak of the CIP-controlled GMR, while its shape is clearly narrower. The latter property agrees with the absence of averaging over many domains in a point-contact MR. Under the reasonable assumption of a unique field scale of the displacement effect, part of the second-peak point-contact MR thus is a GMR. Apparently, the second-peak contacts are less sensitive to the displacement than first-peak contacts, which is probable related to the different few top layers (2 nm Cu/2.4 nm Au instead of 1 nm Cu/3.4 nm Au). The conclusion that part of the MR is GMR agrees with the peak-position (coercivity) increase for $R < 25 \, \Omega$ in Fig. 2, which is absent for Au contacts. The coercivity increase is caused by the destruction of the exchange coupling between neighbouring Co layers due to indentation-induced damage in the ML. For the two resistances above 80 Ω the MR maximum of the second-peak contacts has shifted to the fine structure of the Au contacts. This means that the MR is increasingly caused by the displacement effect.

To correct the MR of the second-peak contacts for the displacement, a calibration of this effect specific for a second-peak ML with a 2.4 nm Au cap is needed. Such a calibration being inaccessible, we use the MR of the Au contacts for this purpose.

Their parabola-like MR and fine structure, $\delta R/R(H=H_{sat})=[R(H=0)-R(H=H_{sat})]/R(H=H_{sat})$ are plotted as a function of $R(H=H_{sat})$ in Fig. 3c. Here H_{sat} is the saturation field of the ML point-contact MR for the in-plane ($\mu_0 H_{sat}=0.1$ T) or perpendicular ($\mu_0 H_{sat}=3$ T) geometry. $\delta R/R(H=H_{sat})$ increases strongly with

increasing resistance, which agrees with the intuitively expected stronger relative change of the contact area per unit tip displacement for smaller contact areas.

This behaviour is similar to that of the MR in Fig. 2, emphasizing the importance of the displacement for the MR of the ML contacts. To correct the MR ratios of Fig. 2 we use the worst-case line through the error bars of $\delta R/R(H=H_{sat})$ (see Fig. 3c). We add the interpolated δR to the saturation resistance of the ML point-contact MR to obtain the GMR ratio. This correction overestimates the displacement effect, since for
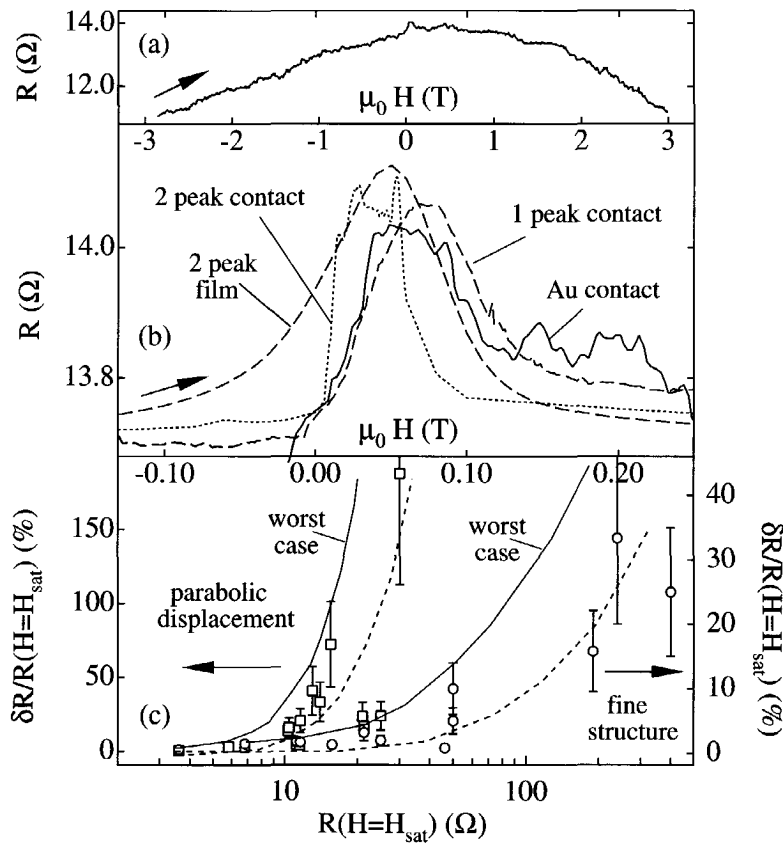
Figure 3 (a) MR of a Au point contact. (b) Expanded view of the fine-structure in the MR at low field of panel (a) together with (G)MRs, with scaled resistance values, representative of first- and second-peak contacts and of the second-peak film. (c) $\delta R/R(H=H_{sat})=[R(H=0)-R(H=H_{sat})]/R(H=H_{sat})$ for Au contacts between 0-3 T (parabolic) and 0-0.1 T (fine-structure) as a function of $R(H=H_{sat})$. Solid lines: worst-case estimate, used as correction. Dashed lines guide the eye.

the same resistance the diameter of a Au contact is smaller than that of a ML contact [10]. GMR curves are obtained by subtracting a Au-contact MR curve with an scaled amplitude equal to the corresponding δR of the worst-case estimate.

In Fig. 2 the filled symbols denote the GMR ratios. The ratio is $\leq 5\%$ for $R < 25\ \Omega$, where the signal is mainly a GMR. For the other extreme, $R > 80\ \Omega$, we find strongly enhanced ratios of over 200%. Large GMR ratios are very well possible for the mixed CIP+CPP geometry of the contacts in combination with a good local magnetic structure. However, these properties do not explain such a strong enhancement. Although the enhancement may be due to a size effect, e.g. collimation [11], it is more likely to arise from inadequacy of the correction procedure for $R > 80\ \Omega$. In this range, which is somewhat limited in Fig. 3c, the resistance is most sensitive to displacement, and the field position of the ML contacts MR has shifted towards the fine structure of the displacement. For intermediate resistances $40\ \Omega < R < 80\ \Omega$, on the contrary, a GMR must remain after correction because of the field-scale arguments discussed in the context of Fig. 3b. For unknown reasons, the two sequences studied in detail in this range behave differently (see inset Fig. 2). For one sequence the ratio takes values up to 10%, while for the other it increases with resistance up to 60%. The in-plane GMR curve corresponding to the 60% point is the solid line in Fig. 1a, while the solid line in Fig. 1b is the corrected perpendicular GMR with ratio 90%. The resulting GMR ratios in the intermediate range have to be reasonable, as follows from the saturation of the GMR, as illustrated in Fig. 1.

Conclusions

In conclusion, we have measured the MR of point contacts made by contacting the tip of an STM to a Co/Cu multilayer. Part of the MR is a magnetostriction effect in the STM, which dominates for contacts to first-peak multilayers, but leaves a clear GMR for contacts to second-peak multilayers. For the latter, restricting ourselves to sequences of resistances measured at a spot, we obtain GMR ratios up to 60%, depending on the local quality of the multilayer.

References

This chapter has been published in Appl. Phys. Lett. **77** (2000).

[1] M.V. Tsoi, A.G.M. Jansen, and J. Bass, J. Appl. Phys. **81**, 5530 (1997).

[2] K.P. Wellock, S.J.C.H. Theeuwen, J. Caro, N.N. Gribov, R.P. van Gorkom, S. Radelaar, F.D. Tichelaar, B.J. Hickey, and C.H. Marrows, Phys. Rev. B **60**, 10291 (1999).

[3] C.H. Marrows, N. Wiser, B.J. Hickey, T.P.A. Hase, and B.K. Tanner, J. of Phys. Cond. Matt. **11**, 81 (1999).

[4] Thesis of J. Wildoër *Low temperature scanning tunneling microscopy on mesoscopic systems* (TUDelft, 1996).

[5] A.I. Yanson, G.R Bollinger, H.E. van den Brom, N. Agrait, and J.M. van Ruitenbeek, Nature **395**, 783 (1998).

[6] P.A.M. Holweg, J. Caro, A.H. Verbruggen, and S. Radelaar, Phys. Rev. B **45**, 9311 (1992).

[7] N. Garcia, M. Munoz and Y.W. Zhao, Phys. Rev. Lett. **82**, 2923 (1999).

[8] P.A.M. Holweg, J.A. Kokkedee, J. Caro, A.H. Verbruggen, S. Radelaar, A.G.M. Jansen and P. Wyder, Phy Rev. Lett. **67**, 2549 (1991).

[9] See, e.g. R.M. Bozorth in *Ferromagnetism* (D. van Nostrand, Totonto, 1951), who also reports that the magnetostriction of Co is $\approx 10^{-5}$. For the 50 nm thick Co in the ML the thickness change thus is 0.5×10^{-3} nm.

[10] We estimate the diameter for a contact resistance R using Wexler's formula $d = \left(\rho_{tip} + \rho_x\right)/4R + 1/R \cdot \sqrt{\left(\rho_{tip} + \rho_x\right)^2/2 + 16/3\pi \cdot R \cdot (\rho \cdot l)_x}$, with ρ_{tip} the resistivity of the tip and ρ_x the resistivity of the Au or ML film and l the mean free path [G. Wexler, Proc. Soc. 89, 927 (1966)]. The product $\rho l \approx 1$ fΩm^2 for all metals [J. Bass, Landolt Börnstein New Series Vol. III/15a (Springer, Berlin, 1982)] and $\rho_{ML}/\rho_{Au} \approx 20$, so that $d_{ML}/d_{Au} = 1 \div 20$.

[11] Collimation is a narrowing of the angular injection distribution. It is a well-known effect in ballistic constrictions in GaAs [C.W.J. Beenakker and H. van Houten, Solid State Physics-Advances in research and applications **44**, 1 (1991)] For neck-shaped ML constrictions collimation not only leads to a stronger CPP current, but also to a higher probability of back-scattering through the orifice for specular scattering at

the interfaces. A collimated current along specific crystallographic directions leads to enhanced reflection probabilities, and thus an enhanced GMR.

Summary of the thesis 'Novel scanning probes applied to the study of nanostructures', by L. Canali, T.U. Delft (2000).

This thesis presents the results of a number of projects aimed at the study of the electronic properties of nanostructures and mesoscopic systems with the highest possible resolution both in space and energy. The experiments described here are built from the combination of three key experimental methods: scanning tunnelling microscopy, low-temperature transport techniques and lithographic microfabrication. The scanning tunnelling microscope (STM), is a well-known instrument for the imaging of conducting surfaces with very high resolution. It uses a sharp tip that is kept at a very small distance above the surface of a sample, close enough to allow a tunnel current to flow. By moving the tip across the sample a topographic image of the surface can be obtained. Moreover the STM can be used as a displaceable and variable contact to study the transport properties of the sample by means of I-V and dI/dV contact- and tunnel-spectroscopies. Under certain conditions, tunnel-spectroscopies allow the local density of states (LDOS) to be probed as a function of energy and position. Many mesoscopic samples present features in the LDOS with a width of just a few meV. Consequently we have developed and utilised STM set-ups capable of reaching and operating at milliKelvin temperatures, which are described in chapter 1.

Since the invention of STM, there has been a large effort in building a series of instruments that extend the basic functioning of STM. Typically, a sensor or probe is mounted on an STM-like tip and scanned above a sample to measure local properties of the samples. In this thesis, we present three such probes that we have developed. The first two probes are intended for the study of the local distribution of charges on mesoscopic samples and are described in chapter 3. In the following two chapters we discuss the fabrication and application of the third and most successful of our probes: the scanning gate (S-gate). S-gates consist of two metallic electrodes that can be used simultaneously in an STM-like experiment: one as the tip, the other as the gate for electronic transport. The gate electrode allows the STM to acquire three-terminal measurements, which can be of great help, for example, to understand the electronic structure of samples containing nanoparticles and colloids. The S-gates have been tested by using them to measure the stability diagram of 20-nm single Au colloids deposited on platinum. We have measured Coulomb blockade and Coulomb steps in

the tunnelling spectroscopies on the colloids and we have been able to see modulation in the current of period e by applying a voltage to the gate electrode.

Sample preparation is a crucial issue for successful scanning probe experiments. The STM imposes a number of serious constraints in the type of samples that can be measured: the substrates have to be conducting, flat and defect-free. Moreover, in our experiments, the nanoparticles have to be well fixed to the substrates and at the same time have a tunnel barrier between them and the substrate. In chapter 7 we present our solutions to these problems using: (a) substrates consisting of flame-annealed gold covered with thiol-terminated self-assembled organic monolayers, (b) flat metallic substrates over which we deposit clusters enclosed in a dielectric shell that bonds to the substrate. With these methods we have been able to prepare and measure samples with clusters ranging from 20 to 2 nm in diameter.

In chapter 8 we present a low-temperature STM study of CdSe nanoclusters. There we describe the synthesis used to prepare the nanoclusters, the preparation of the samples and the low-temperature STM spectroscopies. The dI/dV spectroscopies of CdSe clusters show a sequence of resonances in the conduction band that we interpret as the manifestation of size quantisation in the particles. Spectroscopies taken with small tip-sample separation show extra satellite peaks next to the main ones, which are due to the splitting the degenerate levels because of multiple electronic occupancy inside the clusters.

In chapter 9 we study the surface two-dimensional electron gas (2DEG) at the accumulation layer of the InAs (110) surface. We have developed a sulphur passivation method to protect the surface 2DEG from contact to air and to pin the Fermi level at the surface. We have measured peaks in the density of states in the accumulation layer of InAs by STM spectroscopy at low-temperature. We can model those peaks as quantum levels in a triangular potential-well.

In chapter 10 we discuss an experiment where the STM is used as a movable contact to probe the local variations of giant magnetoresistance (GMR) in Cu/Co multilayers. We find GMR modulations typically of 10% with peaks up to 60%, depending on the local quality of the multiplayer.

Samenvatting van het proefschrift 'Nieuwe scanning probes toegepast bij de studie van nanostrukturen' door L. Canali, T.U. Delft (2000).

Dit proefschrift presenteert de resultaten van een aantal projekten met als doel het bestuderen van de elektronische eigenschappen van nanostrukturen en mesoskopische systemen met de hoogst mogelijke resolutie in plaats en energie. De experimenten die hier beschreven zijn, zijn opgebouwd uit een combinatie van drie belangrijke experimentele methodes: de scanning tunneling mikroskoop (STM), lage-temperatuur transport technieken en lithografische mikrofabricage. De STM is een bekend instrument voor het afbeelden van oppervlakken met zeer hoge resolutie. Er wordt gebruik gemaakt van een scherpe tip die op zeer kleine afstand boven het sample wordt gehouden, dicht genoeg om een tunnelstroom te laten lopen. Door de tip over het sample te laten bewegen, kan een topografische afbeelding van het oppervlak worden verkregen. Bovendien kan de STM gebruikt worden als een verplaatsbaar en variabel kontakt voor het bestuderen van de transporteigenschappen van het sample door middel van I-V- en dI/dV-kontakt- en tunnel spektroskopie. Onder zekere omstandigheden, maakt tunnelspektroskopie het mogelijk de lokale toestandsdichtheid af te tasten als funktie van energie. Veel mesoskopische samples laten kenmerken in de lokale toestandsdichtheid zien met een breedte van slechts een aantal meV. Derhalve hebben we STM set-ups ontwikkeld en gebruikt die in staat zijn te opereren bij milliKelvin temperaturen, welke beschreven zijn in hoofdstuk 1.
Na de ontdekking van de STM, is er veel moeite gestoken in het bouwen van een aantal instrumenten dat de basisfunktie van de STM uitbreidt. In het algemeen wordt er een sensor of probe aangebracht aan een STM-achtige tip en wordt gebruikt boven een sample om de lokale eigenschappen van de samples te meten. In dit proefschrift presenteren we drie zulke probes die we ontwikkeld hebben. De eerste twee probes zijn bedoeld voor het bestuderen van de lokale distributie van ladingen op mesoskopische samples en worden beschreven in hoofdstuk 3. In de volgende twee hoofdstukken behandelen we de fabricage en toepassing van de derde en meest succesvolle probe: de scanning gate (S-gate). De S-gate bestaat uit twee metalen elektrodes die gelijktijdig gebruikt kunnen worden in een STM-achtig experiment: één als de tip, de ander als de gate voor elektrisch transport. De gate elektrode stelt de STM in staat 3-punts metingen te verrichten, welke zeer nuttig kunnen zijn voor het begrijpen van de elektronische struktuur van de samples zoals nanodeeltjes en

colloïdes. De S-gate is getest door het meten van een stabiliteitsdiagram van een 20-nm Au colloïde afgezet op platina. We hebben Coulomb-blokkade en Coulomb-stappen gemeten in de tunnelspektroskopie op de colloïdes en we zijn in staat geweest een modulatie van de stroom te zien met een periode e door een spanning aan te leggen op de gate-elektrode.

Sample-preparatie is cruciaal voor succesvolle scanning probe experimenten. De STM legt een aantal serieuze beperkingen op aan het soort samples dat gemeten kan worden: het substraat moet geleidend zijn, vlak en vrij van defekten, bovendien moeten de nanodeeltjes goed vastzitten aan het substraat en tegelijkertijd een tunnelbarrière hebben tussen hen en het substraat. In hoofdstuk 7 presenteren we onze oplossingen voor deze problemen door gebruik te maken van: (a) substraten bestaande uit flame-annealed goud bedekt met self-assembled organische mono-lagen met thiol-groepen aan de uiteinden, (b) vlakke metalen substraten en clusters omgeven door een diëlektrische schil die aan het substraat bindt. Met deze methodes zijn we in staat geweest samples te prepareren en te meten met afmetingen tussen de 20 en 2 nm.

In hoofdstuk 8 presenteren we een lage-temperatuur STM-studie van CdSe-nanoclusters. Daar zullen we de synthese beschrijven die gebruikt is om de clusters te prepareren, alsmede de preparatie van de samples en de lage-temperatuur STM-spektroskopie. De dI/dV-spektra van CdSe-clusters laten een opeenvolging van resonanties in de geleidingsband zien die we interpreteren als een manifestatie van quantisatie in de deeltjes. Spektra verkregen met kleine afstanden tussen de tip en het sample laten extra resonanties zien ten gevolge het opheffen van de ontaarding binnen de clusters.In hoofdstuk 9 bestuderen we het 2-dimensionale elektronengas (2DEG) in de accumulatielaag van het InAs (110) oppervlak. We hebben een zwavelpassivatie-methode ontwikkeld voor het beschermen van het oppervlak-2DEG tegen lucht en om het Ferminiveau aan het oppervlak te pinnen. We hebben pieken gemeten in de toestandsdichtheid in de accumulatielaag van InAs door STM-spektroskopie bij lage temperatuur. We kunnen die pieken modelleren als quantumniveaus in een driehoekige potentiaalkuil.

In hoofdstuk 10 bespreken we een experiment waar de STM is gebruikt als een verplaatsbaar kontakt om de lokale variaties af te tasten van de "giant magnetoresistance" (GMR) in Cu/Co multilagen. We vinden GMR modulaties van typisch 10% met pieken tot 60%. We schrijven deze variaties toe aan inhomogeniteiten van de multilagen.

Riassunto della tesi di dottorato 'Nuove sonde per microscopia ad effetto tunnel applicate allo studio delle nanostrutture', di L. Canali, Politecnico di Delft, Paesi Bassi (2000).

Questa tesi presenta i risultati di una serie di progetti volti allo studio delle proprietà elettroniche di sistemi mesoscopici e di nanostrutture, misurate ad alta risoluzione sia nelle variabili spaziali che di energia. Gli esperimenti qui descritti sono costituiti dalla combinazione di tre fondamentali metodi di fisica sperimentale: la microscopia ad effetto tunnel, le tecniche di trasporto a bassa temperatura e le tecniche litografiche di microfabbricazione. Il microscopio ad effetto *tunnel* (STM) è uno strumento noto per la sua capacità di studiare superfici conduttrici ad altissima risoluzione. L'STM utilizza una punta ad ago che viene portata in prossimità della superficie del campione, così da instaurare una corrente ad effetto tunnel. Muovendo la punta sulla superficie del campione si ottiene una rappresentazione topografica di quest'ultimo. Inoltre, l'STM può essere usato come contatto elettrico variabile e posizionabile per lo studio delle proprietà elettriche dei campioni, tramite l'acquisizione di spettroscopie I-V e dI/dV, sia a contatto che in modalità *tunnel*. Sotto particolari condizioni, le spettroscopie *tunnel* riescono a misurare la densità locale degli stati (LDOS) in funzione delle variabili energia e posizione. La struttura della LDOS di molti campioni mesoscopici presenta delle modulazioni di appena pochi meV, per questo motivo abbiamo sviluppato ed utilizzato degli STM in grado di raggiungere e funzionare a temperature di pochi millesimi di grado Kelvin, che vengono discussi nel capitolo 1. Successivamente all'invenzione dell'STM molti gruppi di ricerca si sono cimentati nella costruzione di strumenti che ne estendano le funzionalità base. L'esempio tipico consiste in un sensore o una sonda che viene montata su un STM al posto della punta e viene utilizzata per misurare delle particolari proprietà locali del campione in funzione delle coordinate spaziali. In questa tesi discutiamo tre diverse sonde che abbiamo sviluppato: due sonde per lo studio della distribuzione locale di carica in campioni mesoscopici vengono discusse nel capitolo 3, mentre una terza e più proficua sonda chiamata *scanning gate* (S-gate), viene descritta nei successivi due capitoli. Gli S-gates consistono di due elettrodi metallici che vengono impiegati simultaneamente in un esperimento di STM: uno come punta e l'altro come elettrodo di *gate*. La presenza del *gate* consente all'STM di acquisire spettroscopie a tre terminali, che sono di grande aiuto, ad esempio, nell'interpretazione della struttura

elettronica di campioni contenenti colloidi o nanoparticelle. Gli S-gates sono stati testati usandoli per misurare il diagramma di stabilità di colloidi di Au del diametro di 20 nm. Le spettroscopie *tunnel* effettuate su singole particelle colloidali hanno mostrato gli effetti di *Coulomb blockade* e la presenza di *Coulomb steps*. Applicando tensione sull'elettrodo di *gate* abbiamo osservato che la corrente presenta modulazioni di periodo *e*. La preparazione dei campioni è cruciale per il successo degli esperimenti di tipo STM, in quanto è necessario tener conto di una serie di stringenti limitazioni sul tipo dei campioni che possono essere misurati: i substrati devono essere conduttori, piatti e privi di imperfezioni. Inoltre, per i nostri esperimenti, le nanoparticelle devono essere saldamente ancorate ai substrati e devono avere una barriera *tunnel* con il substrato stesso. Nel capitolo 7 presentiamo le nostre soluzioni a questo tipo di problemi utilizzando: (a) substrati di oro temprati con fiamma di idrogeno e ricoperti con un monostrato organico auto-aggregato, (b) substrati metallici su cui vengono depositate particelle racchiuse in un involucro dielettrico che permette loro di legarsi al substrato. Con queste tecniche siamo riusciti a preparare campioni con particelle di diametro variabile fra 20 e 2 nm. Nel capitolo 8 viene presentato uno studio dei *nanocluster* di CdSe tramite STM a bassa temperatura: vengono descritte la sintesi per preparare i nanoclusters, la preparazione dei campioni per STM e le spettroscopie a bassa temperatura. Le spettroscopie dI/dV dei cluster di CdSe mostrano una sequenza di risonanze in banda di conduzione che noi interpretiamo come dovute alla quantizzazione dello spettro elettronico. Le spettroscopie misurate con minor separazione punta-campione mostrano una serie di risonanze satellite dovute alla separazione dei livelli degeneri causata dall'occupazione elettronica multipla all'interno dei *cluster*. Il capitolo 9 tratta lo studio del gas bidimensionale di elettroni (2DEG) nello strato di accumulazione della superficie (110) dell'InAs. Abbiamo sviluppato un metodo di passivazione con zolfo per proteggere il 2DEG dal contatto con l'aria e causare il *pinning* del livello di Fermi alla superficie dell'InAs. Le spettroscopie STM a bassa temperatura, su tale sistema, mostrano dei picchi nella densità degli stati che abbiamo interpretato con un modello di pozzo quantico triangolare. Nel capitolo 10 discutiamo un esperimento in cui l'STM viene usato come contatto elettrico variabile per misurare le variazioni locali della magnetoresistenza gigante (GMR) di un multistrato Cu/Co. Abbiamo misurato variazioni dell'effetto GMR variabili fra un valore tipico del 10% fino al 60%, a seconda della diversa qualità locale del multistrato.

Curriculum Vitae et Studiorum

Luca Canali

May 13, 1971   Born in Parma, Italy.

1985-1990   High-School education at the Liceo Scientifico
                'Ulisse Dini' in Pisa, Italy.

1990-1995   University of Pisa and Scuola Normale Superiore.
                M.Sc. cum laude in Physics.

1995   Undergraduate research under the supervision of
                Prof. F. Beltram.

1996-2000   Ph.D. research at the Technical University of
                Delft in the group Solid State - Quantum
                Transport under the supervision of Prof.dr.ir
                L.P. Kouwenhoven and Prof.dr.ir J.E. Mooij.

List of publications

L. Canali, M. Lazzarino, M. Sorba, F. Beltram, Stark-cyclotron resonance in a semiconductor superlattice, Phys. Rev. Lett **76**, 3618 (1996).

L. Canali, F. Beltram, M. Lazzarino, M. Sorba, High-field transport in superlattices, Superlattices and Microstructures **22**, 155 (1997).

L. Canali, J.W.G. Wildöer, O. Kerkhof and L.P. Kouwenhoven, Appl. Phys. A **66**, S113 (1998).

L. Gurevich, L. Canali, L. Kouwenhoven, Scanning Gate Sensor, Patent number NL1013671 (1999).

L. Gurevich, L. Canali, L. Kouwenhoven, Scanning Gate Spectroscopy on Nanoclusters, Appl. Phys. Lett. **76**, 384 (2000).

S.J.C.H. Theeuwen, L. Canali, S. Radelaar, C.H. Marrows, B.J. Hickey, J. Caro and L.P. Kouwenhoven, Appl. Phys. Lett. **77** (2000).